A QUAD BGO DETECTOR FOR

HIGH RESOLUTION POSITRON TOMOGRAPHY

J. Michael Roney

Foster Radiation Laboratory
Department of Physics
McGill University, Montréal

August 1984

A thesis submitted to the Faculty
of Graduate Studies and Research in
partial fulfillment of the requirements
for the degree of Master of Science.

ABSTRACT

The current trend towards higher resolution positron tomography requires the development of small but efficient detectors. The design and evaluation of a detector comprising four equally spaced, 4.5mm-wide bismuth germanate crystals coupled to a dual photomultiplier tube is presented. The intrinsic optical cross talk between the two sectors of the dual photomultiplier exhibits a spatial dependence that has been exploited for crystal identification. The intrinsic peak efficiency of the detector is higher than that of the low resolution detectors currently in use in the Montreal Neurological Institute's Positome III camera and the full-width at half-maximum (FWHM) timing resolution is 10ns. An evaluation of the use of inter-crystal septa and tapered crystal faces has been made by measuring aperture functions of various detector configurations. The central aperture function of the optimal detector configuration has a FWHM of 3mm.

Résumé

Il existe actuellement dans la domaine de la tomographie par émission de positons (TEP) un besoin de meilleure résolution spatiale. On présente le concept et l'évaluation d'un module capteur qui comprend quatre cristaux de germanate de bismuth d'une largeur 4,5mm couplés à un photomultiplicateur double. Le passage naturel de la lumière entre les deux secteurs montre une dépendance spatiale qui peut être utile pour l'identification de la source de lumière. L'efficacité des cristaux étudiés est plus grande que dans les cristaux typiques du Positome III, un apparail de TEP à l'Institut Neurologique de Montréal. L'index de résolution temporale est de 10ns. On a aussi examiné les avantages de l'emploi de feuilles de tungstène entre les cristaux, et l'emploi de cristaux pointus. L'index de résolution spatiale pour le module optimal est de 3mm.

TABLE OF CONTENTS

LIST OF FIGURES

LIST OF TABLES

ACKNOWLEDGEMENTS

I express here my appreciation for the tremendous support and wealth of ideas provided by Prof. C.J. Thompson throughout this work. The useful discussions with and continual interest shown by Prof. J.K.P. Lee are gratefully acknowledged.

I am indebted to Mr. L.R. Lupton for his contribution of the Monte Carlo simulation work cited in this thesis.

Thanks are due to Messrs. A. Alousi, D. Hetherington, S. Kovalski, and S. Strother and Drs. M. Chidichimo and H. Marshall for numerous informative and stimulating discussions and the general interest and support shown. I also extend thanks to Mr. M. Della Neve for his assistance with the preparation of the ^{56}Co source and Mr. I. Bonnell for his help in the preparation of the circuit diagram in Chapter Two.

The assistance in the preparation of the manuscripts of this thesis and an earlier publication, and the continual support provided by my wife, Beverley, is especially appreciated.

Finally, the financial support of an NSERC Postgraduate Scholarship held during this work is gratefully acknowledged.

CHAPTER ONE

Introduction

1.1 Basic Principles

Positron Emission Tomography (PET) is a procedure that endeavors to quantitatively map the distribution of physiologically interesting chemical compounds present in active biological systems. A compound of interest is labelled with a positron emitting isotope and then administered, either by inhalation or intravenously, to the subject under study. The compound is distributed throughout the body in a manner determined by the biochemical processes to which it is subject. The biochemical pathways followed by the labelled compound resemble, and in some cases are identical, to those of a similar, unlabelled, compound up until the radionuclide labelling the compound decays through positron emission. The spatial distribution of the labelled substance is actually determined by mapping the distribution of positrons in the subject.

Within a few millimetres of its nucleus of origin (if the compound is in a non-gaseous medium), an emitted positron interacts with an orbital electron of the surrounding medium through the process of annihilation. This process is characterized by the transformation of the total energy of the positron-electron system into electromagnetic energy. This usually takes the form of two simultaneously created gamma rays with an energy of approximately 511keV each and travelling in directions almost 180° from each other. The coincidence detection of such paired

gamma rays defines a line along which the annihilation occurred, and thereby provides a 'natural collimation' of the radiation associated with the labelled compound. The concentration of the compound along the line joining two detectors is directly related to the number of 511keV coincidence counts registered by the detectors.

To efficiently exploit this effect the subject should be surrounded by detectors connected to a coincidence circuit, which in turn is interfaced to a dedicated computer that processes an image of the positron distribution. The 'raw data', from which an image may be processed, consist of a series of line integrals, commonly referred to as 'projections', of lines passing through the subject at various angles. Each projection represents the total number of coincidence counts along the associated projection line and therefore is related to the total concentration of the labelled compound along that line. The computer first preprocesses this raw data by performing a normalization of the projections after making corrections for random and scattered coincidences, and gamma-ray attenuation. The corrected and normalized projection data are then reconstructed into a digital representation of quantities, occasionally referred to as 'PET numbers', that are related to the concentration of the labelled compound in the subject. The reconstruction is performed using one of several algorithms, depending on the geometry of the detector system and the specific nature of the data.[IEEE NS-21,1974; Rockmore and Macovski,1976; Macovski and Herman, 1981] When the projections can be restricted to a particular 'slice' (i.e. plane of finite thickness), as in a true tomographic system, the

algorithm most often employed is the 'Convolution Back Projection'. For each angular view of the slice there are a series of projections across the field of view which combine to form a profile function of the positron distribution. In simple back projection, the profile functions are aligned relative to each other according to their corresponding angles and their values projected back on to the image plane. The problem with this method is that values are mapped to locations in the image plane corresponding to areas surrounding regions of activity in the object plane where, in fact, no activity exists. The blurring which results from this can be greatly reduced by convolving the profile functions with an appropriate filter function prior to back projecting the profiles. Using this 'convolution back projection' technique with a carefully chosen filter, the incorrect contributions of back projected profiles to areas surrounding regions of activity are exactly canceled, thus producing a quantitative reconstruction. Once the reconstruction is accomplished, the image plane represents a map of the distribution of the labelled compound in the chosen slice in terms of PET numbers and may be displayed on a video display with the value of the PET numbers indicated either by levels of gray or a colour code. If the detectors and associated electronics exhibit a sufficiently fast timing response (of the order of a few hundred picoseconds), the image quality of the system can be improved using the same number of counts (i.e. the signal-to-noise ratio is improved) by making use of time-of-flight information. [Ter-Pogossian et al, 1981(a); Yamamoto et al, 1982] In such a system, the position of the annihilation along the projection line can be determined by measuring the difference in the arrival time of the two associated

gamma rays. The implementation of such a 'Time-of-Flight' system, being quite complex and costly, has been achieved in relatively few centres. It has not been considered during this study because the detector investigated here (i.e. bismuth germanate) does not have the fast timing response required of a time-of-flight detector.

1.2 Requirements of a Medical PET Detector

The PET technique of imaging positron emitting isotope distributions has been primarily exploited for medical research, where it has enabled one to conduct in vivo studies of quantifiable physiological processes which cannot be performed in any other way. Appendix One presents a few examples of such studies. When PET is applied to such studies of the human system a number of constraints are imposed on the imaging problem. A major constraint is the amount of radioactivity to which a human subject is exposed. Although for most PET studies the critical organ doses currently are at, or below, those received during most nuclear medicine studies, which range typically between 3 and 10 rads [Correia et al,1979; Ter-Pogossian,1981(b)], it is important to produce the maximum benefit from such studies for the minimum amount of radiation. The quality of the quantitative image of the labelled substance is influenced by the way scattered and random events are treated and the gamma-ray attenuation-correction technique employed (see Appendix Two), the reconstruction filter used, and, perhaps most importantly, by the number of true counts used to form the final image. It is therefore crucial to employ a detection system which maximizes the overall coincidence detection efficiency, thereby increasing the number of true

counts, and to minimize the coincidence resolving time, in order to reduce the number of random events. The efficiency depends on the geometry of the camera, the detector material and the dead time of the system, while the resolving time depends on the detector material and readout electronics. In designing a PET detector, then, a detector material with a high photoelectric cross section for 511keV gamma rays (see Appendix Two) and a fast response time when coupled to its readout electronics should be used. The detectors should be incorporated into an array covering a large solid angle with a high detector packing density. An additional constraint, particularly when processes in the human brain are to be studied (the specific medical application to which this work is addressed), is the requirement of high image spatial resolution. It has been demonstrated that quantitative studies of the behaviour of labelled compounds in small cerebral structures (such as in the cerebral cortex grey matter which is 4mm wide in places) requires a detector having a spatial resolution of 2mm FWHM (since quantitation requires the resolution be a factor of two finer than the dimension of the object under study.) [Budinger et al,1984] The fundamental problem, therefore, is to design a detector system with a spatial resolution of the order of a few millimetres that maximizes overall efficiency and minimizes the timing resolution.

1.3 Physical Constraints on a Medical PET Detector

A high efficiency PET system requires a detector material which has a large cross section for the absorption of annihilation radiation, an efficient means of identifying the absorption of paired 511keV gamma rays

with a small coincidence resolving time, and the ability to fill the detection solid angle with as much detector material as possible (i.e. large detection packing fraction). Since a large absorption cross section requires a material with a high atomic number(Z) (see Appendix Two), the use of the type of solid state detectors currently available is ruled out and, therefore, the thrust of PET detector development has been in two general directions: scintillators and multiwire proportional chambers (MWPC) coupled to high Z (usually lead-based) converters. In the MWPC-Pb detectors, the converter plate has an array of small holes pierced through it, often in a honeycomb system, and an electric potential introduced across the plate. A gamma interaction in the converter releases electrons into the holes. They then drift in the electric field until emerging from the plates where they are detected by the MWPC. The MWPC-Pb detectors have spatial resolutions of about 4mm [Jeavons,1979] but the time spread of the electrons exiting the converters is between 100ns and 300ns (depending on the particular design) thus limiting the coincidence resolving time and increasing the accidental count rate. For this reason MWPC-Pb detectors are currently restricted to low count rate applications, such as those not involving human subjects, but work is in progress that may improve the timing characteristics enough to make these devices medically useful in the future.[Bellazini et al,1984;McKee,1984] In the scintillation detector, which is favoured for medical applications, the electrons released by a gamma interaction lose their energy in the scintillator primarily through the ionization and excitation of surrounding orbital electrons. Some of the energy excites states which suffer radiative decay in the optical or near-optical

wavelengths. These optical photons are then detected and converted into electrical impulses by a photomultiplier tube (PMT) or solid state photodetector. The timing characteristics depend on the decay time of the excited atomic states of the scintillator, the scintillation efficiency, light collection efficiency, and the quantum efficiency and the timing response of the photodetector. Resolving times of commonly used scintillation detectors range from tens of picoseconds to tens of nanoseconds, which explains the preference for them in medical applications. What is required, then, is a high Z scintillator that can be arranged in an array with a high packing fraction, and that has a timing resolution of less than a few tens of nanoseconds. Since the late 1970's it has been recognized that bismuth germanate (BGO) more or less fulfills all of these requirements and it has become the detector of choice for scintillator based conventional PET systems.[Brooks et al,1981] Cameras employing scintillators generally have the detectors incorporated into circular or polygonal arrays referred to as 'rings'. Such an arrangement provides the maximum detector solid angle for a given slice, whose thickness is determined by the height, or axial extent, of the detectors.

When considering the resolution of a detector system there are two fundamental physical properties of the annihilation process which set an absolute limit on the PET spatial resolution: positron range and non-colinearity of the annihilation radiation. As described in Appendix Two, positrons travel a finite distance in an absorbing medium before being thermalized and annihilating with an orbital electron. This

'positron range' is a function of the initial energy of the positron (which in turn depends on the parent nuclide) and the absorber. Studies of this effect [Derenzo,1979; Hoffman and Phelps,1976; Cho et al,1975] have shown that it is non-negligible for isotopes having beta end-point energies greater than around 1MeV. The spatial distribution of annihilations associated with positrons emitted from a point source (Point Spread Function:PSF) is not gaussian: it is sharply peaked and has exponential tails. For ^{68}Ga (E_{max}=1.90MeV) in water, the full width at half maximum (FWHM) of the PSF is about .30mm [Derenzo,1979]. Approximately 75% of the area under a gaussian distribution is contained between the half maxima, but if the ^{68}Ga-H_2O PSF is projected onto a plane, 75% of the projected annihilations occur within a radius of around 2.7mm. The spatial resolution of studies using a detector system with a FWHM resolution of around 2 to 3mm using ^{68}Ga, ^{15}O (E_{max}=1.73MeV), ^{13}N (E_{max}=1.19) and, to a lesser extent, ^{11}C(E_{max}=.961MeV) would be non-negligibly degraded by the positron range effect. Studies involving ^{18}F (E_{max}=.633 MeV), however, would not suffer a significant loss of resolution due to the range of positrons. (The 75% width in water is only about .6mm [Cho et al,1975].) A more significant degradation of the resolution is due to the non-colinearity of the paired 511keV gamma rays as discussed in Appendix Two. For PET, this does not significantly depend on the positron emitting isotope and the absorbing medium. However, there is a strong dependence on the distance between the two detectors registering a coincidence, D:

$$FWHM_{non\text{-}col} = \frac{D}{2}\tan(.25^\circ) \qquad [1.1]$$

For D=50cm, a typical dimension for a head scanner, the contribution to the spatial resolution FWHM due to non-colinearity is 1.1mm. This is an important contribution in a high resolution system and worthy of consideration when determining the geometric dimensions of a camera. Although the positron range and non-colinearity effects are non-negligible, the spatial resolution of PET systems has been almost entirely limited by the technical problem of producing narrow detectors with a high packing fraction.

1.4 Development Work on Medical PET Detectors

A major technical obstacle to obtaining narrower detectors has been the unavailability of PMTs small enough to couple efficiently to narrow scintillation crystals. One promising approach to this problem replaces the PMT with a large area silicon avalanche photodiode(APD).[Entine et al 1983;Petrillo et al,1984] Unfortunately the APDs are still in the developmental stage with work yet to be done on their optimization for scintillation detection and on improvement in fabrication methods to increase the production yield of uniform gain, low noise devices. The yield has yet to be increased to a level that would bring about a reduction in cost significant enough to make the use of these devices feasible in a PET system. Recent work by most groups attempting to improve the spatial resolution of PET cameras has therefore concentrated on the coupling of several small crystals to at least one PMT for timing

information, with crystal identification and energy information being provided by one of a variety of techniques. Derenzo[1983;1984] and Yamashita et al[1984] have used silicon photodiodes cooled to about 200K to obtain both energy discrimination and crystal identification. Yamashita et al[1984] have also reported on the performance of a PMT with a control grid that modulates the photoelectrons coming from one half of the photocathode to provide crystal identification using pulse shape discrimination. A detector comprising the control grid PMT, two 4mm wide BGO crystals and 2mm wide septa has coincidence timing and energy resolutions of 6ns and 30% FWHM respectively [Murayama et al,1984]. A similar scheme using a control grid consisting of sense wires on, or in, the face of the PMT had been proposed by Charpak[1967] and Boutot and Pietri[1972] and is currently being re-examined by Vacher[1984]. Barton et al[1983] have shown that mercuric iodide crystals can be used to localize an event to one crystal while energy information is provided by the PMT. Eriksson et al[1983] and Wong et al[1984] have coupled two scintillators made from different materials (BGO/GSO (Eriksson) and CsF/BaF_2(Wong)) to one PMT, using pulse shape discrimination to identify the crystal. Other techniques include that of Burnham et al[1984], who optically couple several small crystals by means of a light pipe to more than one PMT, and Meuhllehner et al[1983], who couple several PMTs to a single bar of scintillation material and use Anger camera methods [Anger,1966] to decode the azimuthal position of an interaction. (i.e. the interaction position is defined as the centroid of the position spectrum, which is derived from the position dependent PMT pulse height distribution of the PMTs near the point of interaction.)

Rogers [Rogers, 1984; Yao Guang and Rogers, 1984] proposed a design, similar to that of Meuhllehner, that uses the Anger techniques to determine both the azimuthal and altitudinal positions of an interaction and uses the shape of the position spectrum to determine the depth of the interaction in the crystal. Murayama et al[1982] have directly coupled four 15mm-wide BGO crystals to two PMTs using a light-sharing scheme similar to the one proposed here. The Murayama design has some scintillation light shared through alternate pairs of adjacent crystals. This results in the alteration of the pulse heights, and therefore the design requires a moderately complex decoding scheme. Moreover, this light sharing method precludes the use of inter-crystal septa.

The design presented here exploits the intrinsic, position dependent, spread of light through the entrance window of a dual PMT to provide azimuthal crystal identification. Because the pulse heights are not affected by this light sharing, a simple decoding scheme composed of two double-channel analysers for each four crystal-dual PMT combination can be used. This design also permits the insertion of inter-crystal septa, which have been used to decrease the resolution losses at the edges of a tomograph. The various factors that have been considered in the design of the detector include the PMT characteristics, crystal properties, the crystal identification encoding scheme and decoding electronics, and the effect of inter-crystal tungsten septa and pointed crystals on off-centre in-slice spatial resolution. Chapter Two contains a detailed discussion of these design considerations, and an evaluation of the significant characteristics of the detector based on a series of

measurements is presented in Chapter Three. The assessment of this detector demonstrates that it provides a cost effective solution to the problem of obtaining a higher resolution PET system.

Because this work has been primarily motivated by the need for higher resolution, much effort has been spent on studying the spatial resolution of various crystal-septum configurations of the detector. The studies are based on the experimental determination of the in-slice aperture function. This aperture function is the in-slice coincidence response of a detector pair, as a line source, oriented perpendicular to the slice plane, is moved past the detectors. The intrinsic resolution of a pair of detectors is usually quoted in terms of the FWHM of the aperture function and, because the function is not gaussian, the full-width at tenth-maximum (FWTM) is also often quoted. For off-centre sources viewed by a detector pair not aligned along a ring diameter (i.e. detectors oriented at an angle to each other), the aperture function is influenced by crystal penetration and inter-crystal scatter of the gamma rays. This results in a skewing and widening of the function, which accounts for a loss of resolution at the edges of a tomograph. It has been shown that the use of septa and tapered crystals reduces these resolution losses for detectors with widths greater than 6mm [Keller and Lupton, 1983 and Lupton et al, in press], but no definitive investigation into their effectiveness for narrower crystals has been made until now. The aperture function of two detector configurations, one comprising $30x15x4.5mm^3$ BGO crystals with 1.0mm inter-crystal air-gaps and the other made up of the same sized crystals with the inter-crystal space

occupied by tungsten septa, were measured and also calculated using the Monte Carlo code developed by Keller and Lupton [1983]. The effect of adding a point to the crystals was investigated by measuring the aperture functions for detectors using $33.2 \times 15 \times 4.5 mm^3$ crystals with the face tapered to a 70° angle. Chapter Four contains a discussion of these aperture function measurements and calculations which provide a conclusive evaluation of the effect of inter-crystal septa and tapered crystals on spatial resolution.

CHAPTER TWO

Detector Design

2.1 Introduction

The dual requirements of spatial resolution of the order of a few millimetres and high efficiency motivated C.J. Thompson to design a detector consisting of four narrow BGO crystals in optical contact with the face of a dual-anode photomultiplier, such as the Hamamatsu R1548 PMT.[Thompson, 1983] The R1548 has two independent PMT segments, A and B, in a single glass enclosure. This PMT was specifically designed to detect the scintillation light from two BGO crystals for use in positron tomography. If, however, four crystals are coupled to the dual PMT, as in the Thompson design, a scheme that identifies the particular crystal in which a gamma ray interacts is required. In the original proposal, illustrated in Figure 2.1, two of the crystals, labelled 1 and 2 in Figure 2.1(a), are coupled to the half of the PMT face in front of photocathode A and the two remaining crystals, 3 and 4, are coupled to the sector B half of the PMT face. Timing and energy information related to events in crystal 1 or 2 is obtained from the output of the anode of sector A and the same type of information associated with interactions occurring in crystal 3 or 4 is obtained from the sector B output. To identify the crystal of interaction a light sharing scheme similar to that developed by Murayama et al[1982] was proposed. The two outer crystals, 1 and 4 in Figure 2.1(a), are optically connected to each other by a light pipe which passes above all four crystals. It was expected that about 10% of the light from one outer crystal would be channelled via the other outer crystal to the photocathode of the opposite sector.

FIGURE 2.1 INITIAL PROPOSAL FOR A HIGH RESOLUTION BGO DETECTOR

(a) Drawing of the original Thompson design. Crystal identification would be accomplished by cross coupling 10% of the scintillation light between the outer crystals (1 and 4) using a light pipe. The design was found to be unfeasible for reasons cited in the text.

(b) Expected electrical response of the Thompson detector design depicted in Figure 2.1(a). This diagram can be thought of as a schematic oscilloscope trace of the detector preamp output when a 511keV gamma ray is absorbed in each of the four crystals. When an interaction occurs in one of the outer crystals, the cross coupling through the light pipe would produce a small response in the alternate PMT sector. No alternate sector response occurs when an inner crystal absorbs a gamma ray. (The modified design, using the intrinsic optical cross talk between the two sectors, has cross coupling occurring for the inner crystals instead.)

(c) Drawing of the proposed positron tomograph based on the quad BGO detector. The tomograph would have five rings each with 320 crystals. The total number of dual PMTs for this tomograph would be 400. (Parts of this diagram are from Budinger et al, 1984)

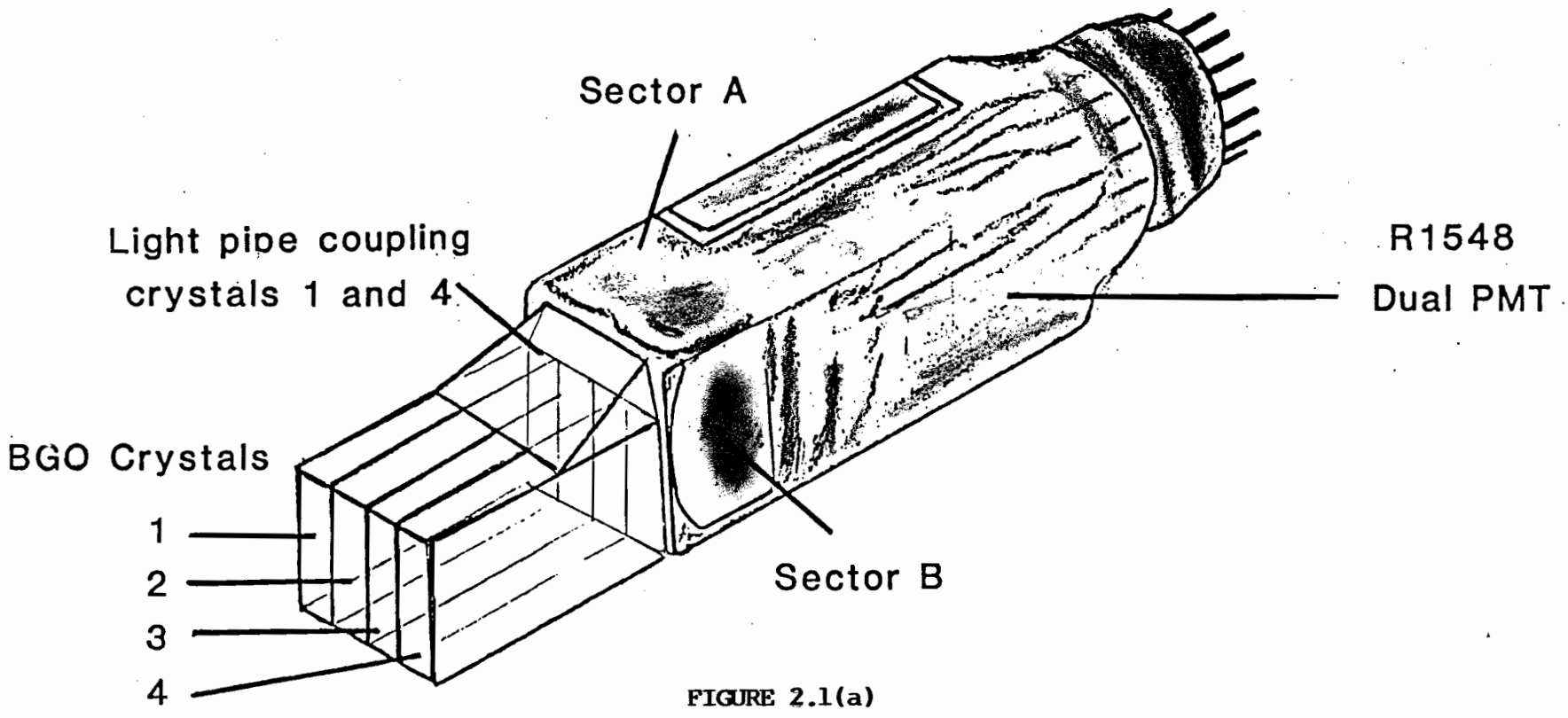
Sector A
Light pipe coupling
crystals 1 and 4
R1548
Dual PMT
BGO Crystals
1
2
3
4
Sector B

FIGURE 2.1(a)

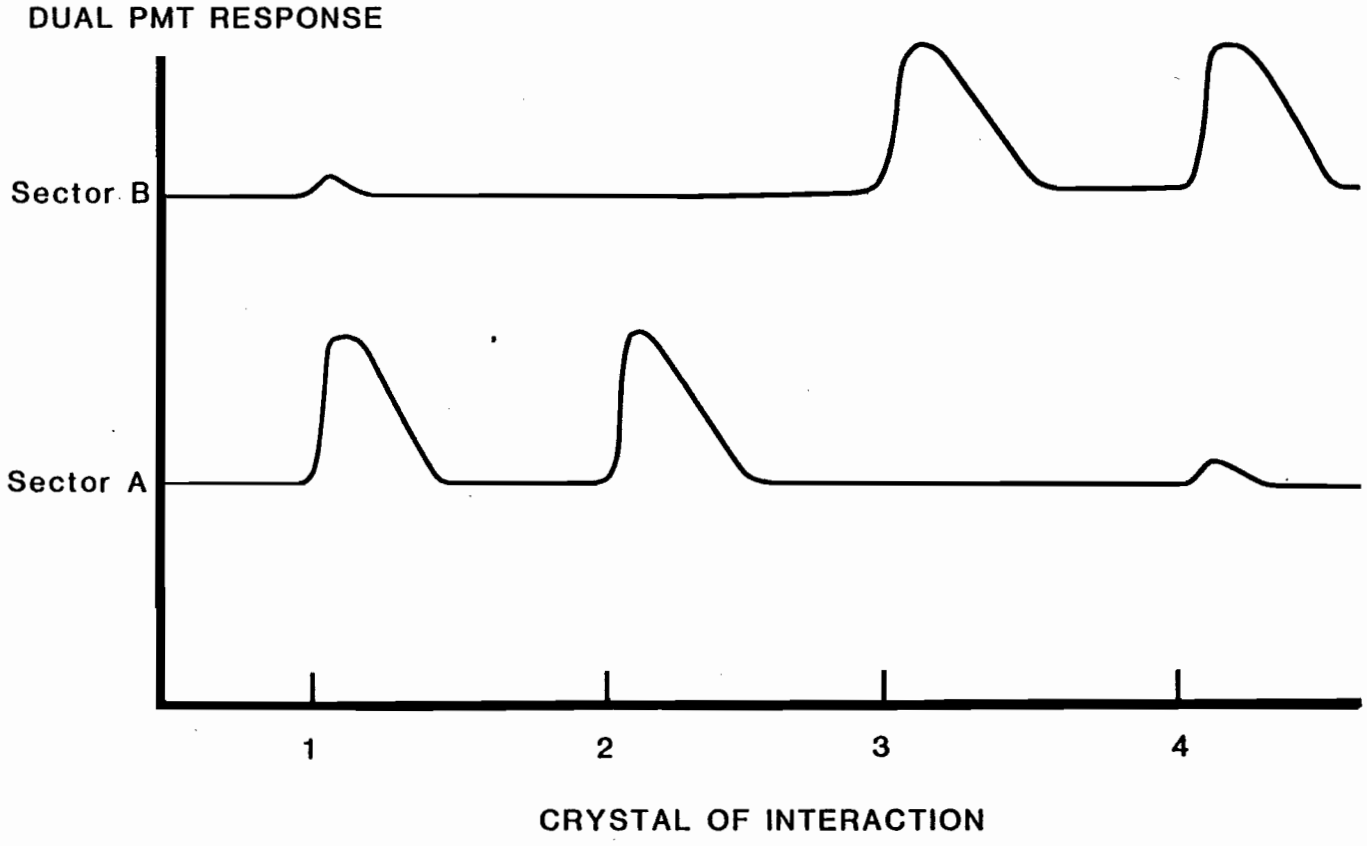
DUAL PMT RESPONSE
Sector B
Sector A
1
2
3
4
CRYSTAL OF INTERACTION

FIGURE 2.1(b)

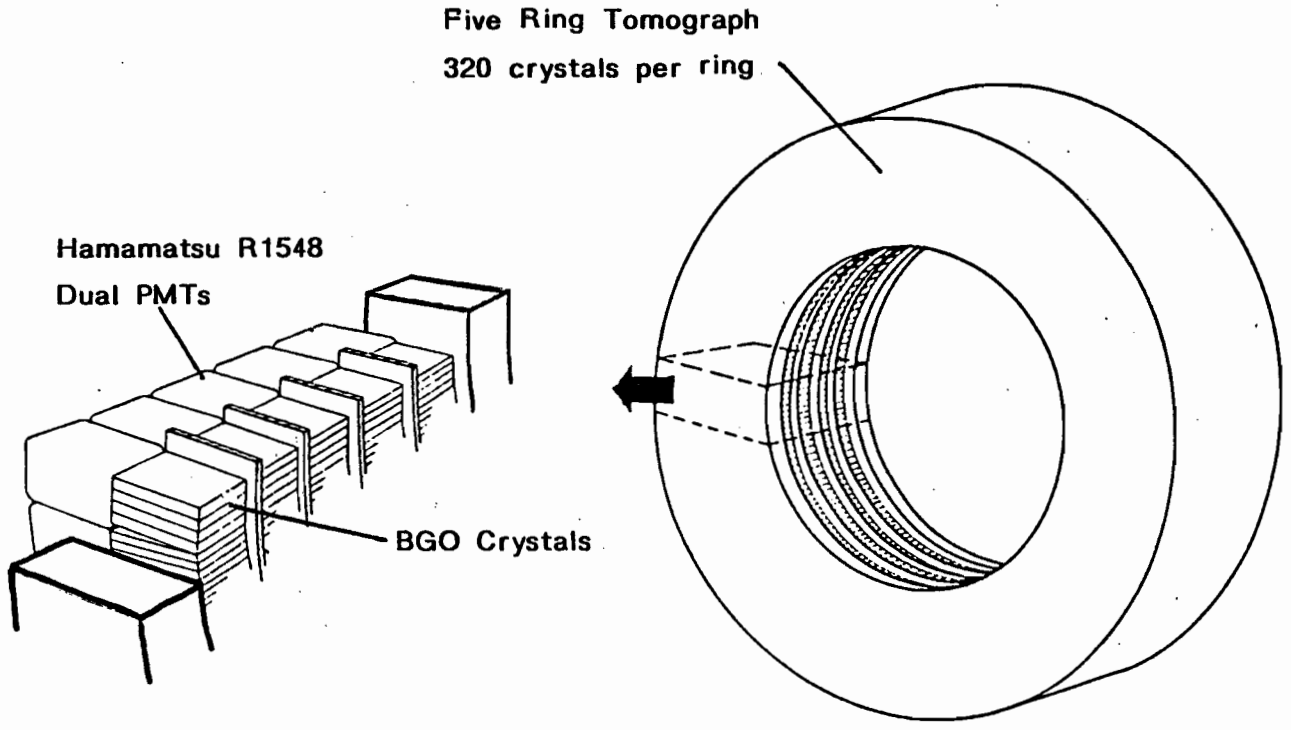
Five Ring Tomograph
320 crystals per ring
Hamamatsu R1548
Dual PMTs
BGO Crystals

FIGURE 2.1(c)

In this way, the absorption of a gamma ray in an outer crystal would produce a near full-energy pulse in the PMT sector to which it is directly coupled, and a small pulse in the opposite sector. An interaction in an inner crystal, however, would only produce the full energy pulse. Figure 2.1(b) is a schematic of this expected electrical response of the two PMT sectors to gamma rays absorbed in each of the four crystals. A preliminary study, undertaken to investigate the feasibility of this design, demonstrated that it would not work in practice because of the existence of optical cross talk between the two PMT sectors, as reported by Yamashita et al[1982]. However, it was found that this same optical cross talk, which is caused by the spread of light through the entrance window of the PMT, exhibits a spatial dependence which can be effectively exploited for crystal identification. In the design proposed in this work, which is a modification of the Thompson design, there is no light pipe and, instead of interactions in the outer crystals producing a small response in the opposite PMT sector, cross-sector response is generated by inner crystal interactions. A schematic of a tomograph array composed of five rings of quad BGO detectors is presented in Figure 2.1(c).

2.2 Properties of Bismuth Germanate

Bismuth germanate ($Bi_4Ge_3O_{12}$, referred to as BGO) is a cubic crystal isomorphic with eulytine, a naturally occurring mineral, $Bi_4Si_3O_{12}$, whose structure is associated with a number of luminescent materials [Blasse, 1970]. The density of BGO is 7.13g/cm^3 with the contributions of the three constituents weighted as: Bi:67.1%,

Ge:17.5% and O:15.4%. The presence of bismuth, which has the largest atomic number of the stable elements (Z=83) apart from uranium and thorium, gives BGO a high photoelectric cross section. The total linear attenuation coefficient of BGO, because of the high effective Z combined with a moderately high density, is .903cm^{-1} at 511keV [Derenzo,1982]. Although the linear attenuation coefficient is less than that of tungsten (2.41cm^{-1}) and lead (1.65cm^{-1}) it is larger than that of all other readily available scintillation materials. Because BGO is chemically inert and non-hygroscopic, the high packing fraction required of a PET system is readily achieved with BGO, as no inter-crystal space need be wasted on hermetic canisters.

The BGO emission spectrum peaks at 480nm and has a FWHM of 150nm with the peak asymmetrically broadened at longer wavelengths. (Piltingsrud [1979] has resolved the asymmetry into three components at low temperatures: 530, 570, and 610nm.) The fluorescence is due to the decay of the Bi^{3+} ion from the excited $^3P_1$ state to the $^1S_0$ ground state. The emission and absorption spectra of BGO are very well separated, as can be seen in Figure 2.2(a) [Weber and Montchamp, 1973]. This separation is primarily due to a stokes shift of approximately 2.2eV [Weber and Montchamp, 1973]. This stokes shift can be understood in the following way: the local vibrational states of the crystal lattice depend on whether the Bi^{3+} ion is in a ground or excited state. Because of this dependence, when the Bi^{3+} is in an excited state the energy difference between the excited and ground states of the lattice is about 2.2eV smaller than when the Bi^{3+} is in a ground state. Therefore, a

FIGURE 2.2 LUMINESCENCE CHARACTERISTICS OF BGO

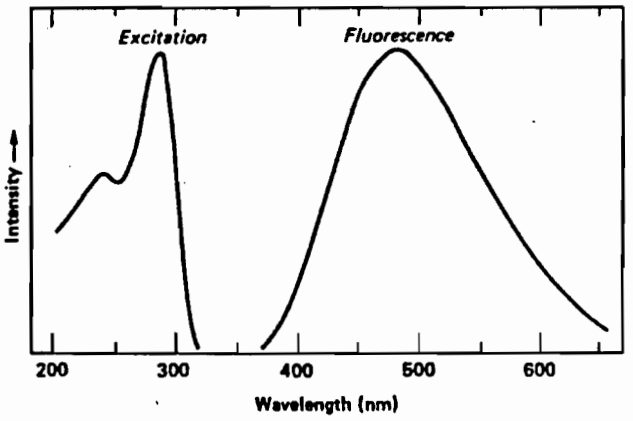

Figure 2.2 (a) Excitation and Fluorescence of Bismuth Germanate from Weber and Montchamp, 1973

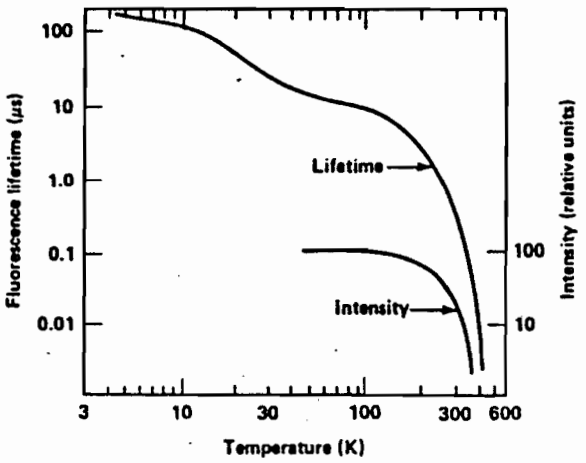

Figure 2.2 (b) Temperature Dependence of Bi^{3+} Luminescence from Weber, 1982

photon emitted at around 2.6eV(480nm) is not reabsorbed by the crystal since approximately 4.8eV is required to excite the Bi^{3+} and lattice from the ground state. The additional energy is required because of differences in the vibrational states of the crystal. It is not surprising, therefore, that the life time of the $^3P_1$ state and its intensity are strongly temperature dependent, as can be seen in Figure 2.2(b).

The initial absorption of a gamma ray is followed by a complex cascade of secondary processes (ionizations, atomic excitations and subsequent decays etc.) which ultimately result in the creation of a large number of excited Bi^{3+} ions. The efficiency of these processes is directly related to the scintillation efficiency of the crystal, which is the fraction of the total absorbed incident particle energy that is converted into detectable optical photons. The scintillation efficiency of BGO has not been determined conclusively, but one estimate of the value of the light yield for BGO is $(1\pm.5)x10^4$ photons/MeV [Lorentz,1982]. This amounts to a scintillation efficiency of around (2.4+1.2)% (assuming a mean scintillation photon wavelength of 500nm [Lorentz, 1982]), which is considerably less than that of the 13% scintillation efficiency of the standard thallium activated sodium iodide NaI(Tl) scintillator [Knoll, p334, 1979]. Taken together with the fact that BGO has a high index of refraction (2.152 at 480nm [Bortfeld and Meier, 1972]), which introduces optical losses at the interface between the crystal and photodetector, BGO is usually quoted as having an integrated light output equal to around 10% of that of NaI(Tl).[Faruki,

1982(a)] The net result of the low scintillation efficiency and high refractive index is that the photoelectron statistics are relatively low, and consequently the energy resolution of BGO is quite poor. The resolution of a scintillation detector is primarily determined by the intrinsic scintillation efficiency of the crystal (including effects due to impurities), crystal geometry and the ratio of light collection area to total crystal surface area, the reflectivity of the crystal surface coating, the relative refractive indices of the crystal, coupling compound and photodetector, and the quantum efficiency and uniformity of the sensitivity of the photodetector. Fan [1964] developed an analytic expression to approximate the efficiency of light detection from a scintillation crystal coated with a diffuse reflector:

$$\varepsilon = \frac{K_1 K_2 A_o}{A} \left[1 - \eta \left[1 - \frac{K_1 K_2 A_o}{A} \right] \right]^{-1} \qquad [2.1]$$

where: ε is the efficiency of light detection.
η is the coefficient of reflectivity of the crystal surfaces.
A is the total crystal surface area.
A_o is the area of the crystal surface coupled to the PMT.
K_1 is the probability that a photon impinging on the crystal surface coupled to the PMT reaches the photocathode. It may be expressed as:

$$K_1 = [4n/(n+1)^2] \times [1 - \cos(\sin^{-1}[1/n])] \qquad [2.2]$$

where n is the ratio of the refractive index of the crystal to that of the PMT window assuming perfect coupling.
K_2 is the quantum efficiency of the photocathode.

For a $10x20x30mm^3$ BGO crystal, with 95% reflectivity at its surfaces, coupled to a PMT with a 20% quantum efficiency and using Lorentz's [1982] figures for BGO light yield, photoelectron statistics account for a FWHM resolution of $(12\pm3)\%$. If the reflectivity is 90%, this figure becomes $(17\pm4)\%$. Although a BGO-PMT detector has poor energy resolution, the

resolution still permits one to use energy information for the identification of the annihilation radiation. Moreover, the energy window of a PET single channel analyser (SCA) is usually quite wide (typically 350-700keV) in order to allow for long term thermal drifting of the electronics, and therefore poor energy resolution is not considered a serious drawback in a PET detector.

Three components in the decay curve of BGO have been observed [Faruki, 1982(b); Gu, 1982]: the main 300ns component, a 60ns part responsible for about 10% of the light output, and a weak 570-600ns component. These life times are strongly temperature dependent, tending to decrease with increasing temperature. Although the long decay times hinder the coincidence timing resolution of a BGO detector, the fact that BGO also has very little after glow (less than .005% of maximum intensity after 3ms [Faruki, 1982(b)]) allows one to use first photoelectron timing methods. By setting a leading edge discriminator level very low, one can trigger off the first photoelectron emitted from the photocathode of a PMT. In the case of BGO, this would probably be associated with the 60ns decay component. BGO-BGO coincident timing resolutions as small as around 2ns have been measured.[Okajima et al, 1982]

2.3 Hamamatsu R1548 Characteristics

The basic characteristics of the R1548 were described in detail by Yamashita et al [1982]. This dual PMT has a flat, 24x24mm^2 front face with two 10x20mm^2 bialkali photocathodes, each with a separate

ten-stage set of dynodes. Corresponding dynodes from each sector are electrically connected to the same pin in the PMT base, except for the seventh dynodes, which are connected to two separate pins in the base. Independent adjustment of the potentials on the seventh dynodes provides separate gain control of each sector over a 1:.03 range. The semi-transparent bialkali photocathode deposited on the borosilicate glass window of the R1548 has an extended green sensitivity. The spectral response of the PMT, shown in Figure 2.3(a) [Yamashita et al, 1982], matches the emission spectrum of BGO in the blue with decreased matching in the green but which is still a good match for BGO. The quantum efficiency at the peak of the BGO emission spectrum, 480nm, is around 22% and the sensitive area of the photocathode covers most of its physical area as can be seen in Figure 2.3(b), which is a contour map of the photocathode's sensitivity profiles. When the R1548 is coupled to two $12x24x24mm^3$ BGO crystals it exhibits timing and energy resolution characteristics that are quite adequate for a conventional PET system: Yamashita et al [1982] have measured an energy resolution of 19.0% FWHM at 511keV and a BGO-BGO coincidence timing resolution of 2.9ns FWHM and 6.2ns FWTM using constant fraction discriminators in a fast-slow coincidence detection system.

Since such measurements depend on the quality of BGO crystals used, particular PMTs involved, and the coincidence timing electronics (e.g. constant fraction, leading edge etc.), a series of experiments were performed to compare the R1548 timing and gain characteristics with those of the Hamamatsu R1213 PMT, which is currently being used in a PET

FIGURE 2.3 SPECTRAL RESPONSE AND PHOTOCATHODE SENSITIVITY MAP OF THE R1548

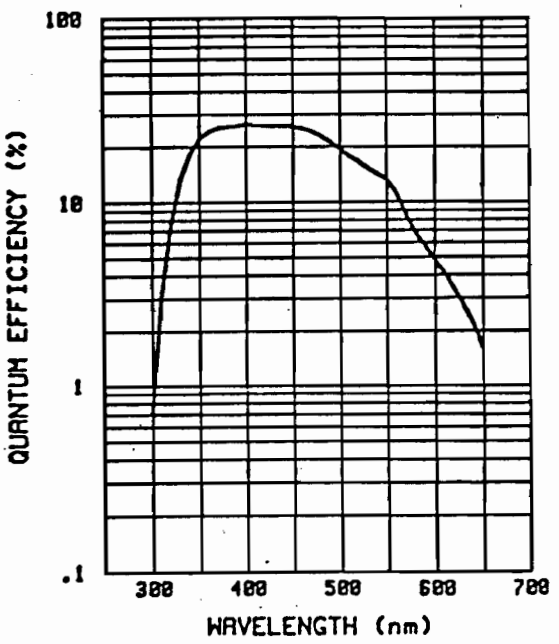

Figure 2.3(a) Spectral Quantum Efficiency of the Hamamatsu R1548 Dual PMT [From Murayama et al, 1982]

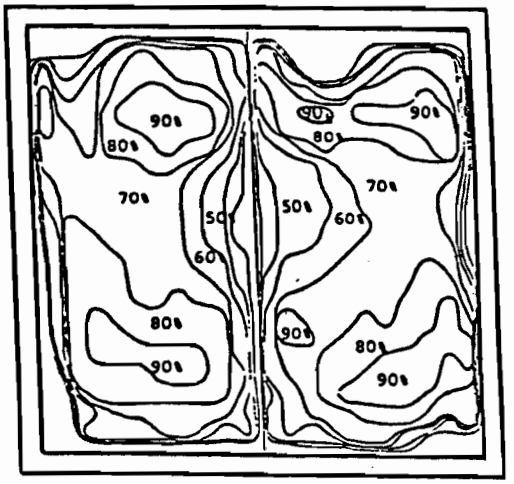

Figure 2.3(b) Contour Map of Sensitivity Profiles of the R1548 Anode Output. Each sensitivity shown is normalized by the maximum value.[From Murayama et al, 1982]

detector system at the Montreal Neurological Institute (MNI): the Positome III camera. A $10x20x30mm^3$ BGO crystal, with polished surfaces and coated with a diffuse reflector, NE560 (a TiO_2, water based, white paint), on five sides, was optically coupled to the R1213. The clear $10x20mm^2$ end face was coupled to the PMT face with GE602 epoxy resin. This resin is transparent over the BGO emission spectrum and, because it has an index of refraction close to that of the borosilicate PMT entrance window, one can assume that, when it acts as the coupling agent, only a single optical interface exists between the BGO and PMT window. In addition, the resin is sufficiently viscous to provide a stable but impermanent optical link when used without adding a hardener. Under operating conditions identical to those of the Positome detectors, the energy resolution of the BGO-R1213 detector is (27±1)% FWHM at 511keV. The timing resolution of the BGO-R1213 detector and a 1"x1" NaI(Tl) detector viewing a ^{68}Ge source was measured using a leading edge timing single channel analyser (SCA). The commercially available ^{68}Ge has a half life of 275 days and decays entirely through the electron capture weak interaction to ^{68}Ga. The ^{68}Ga, with a half life of 68 minutes, decays mostly (88%) through positron emission. The timing threshold was set at about 1% of the pulse height and the SCA window set between 350 and 650keV. These measurements yielded a value of (9.9±.7)ns FWHM for the timing resolution. The same crystal was then coupled to an R1548 PMT using the GE602 resin, as before. The high voltage on the R1548 was set at +1450V, which was chosen in order to generate pulses having the same magnitude as those produced by the BGO-R1213 detector. Using the same electronic configuration as in the previous measurement, the energy and

TABLE 2.1 RESULTS OF HAMAMATSU CHARACTERIZATION MEASUREMENTS

PMT	Crystal Size (mm^3)	Timing Pick-off Method	Energy Resolution (FWHM %)	Timing Resolution (FWHM ns)	Detector Pair
R1548*	24x24x12	constant fraction	19	2.9	BGO-BGO
R1213	30x20x10	leading edge	27±1	9.9±.7	BGO-NaI
R1548	30x20x10	leading edge	25.6±.2	3.2±.5	BGO-NaI

* Yamashita, 1982 measurement

timing resolutions were (25.6±.2)% FWHM and (3.2±.5)ns FWHM respectively. The results of this series of measurements concur with Yamashita et al [1982] in recommending the use of the R1548 in a conventional PET system. Table 2.1 summarizes these results and those of Yamashita.

As well as determining that the R1548 possessed adequate timing and gain characteristics, it was necessary to investigate the properties of inter-sector cross talk. In addition to the optical cross talk mentioned in the introduction of this chapter, the existence of electrical cross talk between the two sectors was also revealed. The electrical cross talk is characterized by pulses of opposite polarity and shorter duration than the signals from the direct scintillation of BGO. This cross talk is caused by the modulation of the dark current in one sector of the PMT when a charge pulse on the other side lowers the potential of the corresponding dynodes. This cross talk was eliminated by capacitively coupling the ninth and tenth dynodes to the cathode with a 0.001 microfarad capacitor.

The optical cross talk was found to exhibit position dependence such that when light entered the window close to the centre of the PMT face, considerably more light was channelled through the entrance window to the opposite photocathode than when light entered the window close to the edge of the PMT face. But as can be seen in Figure 2.3(b), the photocathode sensitivity is not completely uniform and, because of this, it was necessary to investigate whether the optical cross talk would (a)

exhibit a position dependence that would be useful for crystal identification and (b)interfere with the 511keV pulse height. The following experiment was performed to test whether or not this property could be used as a means of crystal identification when four crystals are coupled to one R1548. Two 30x20x10mm^3 BGO crystals were painted on five sides with the NE560 reflector. In addition, half of the 20mmx10mm side coupled to the PMT was painted white. One crystal was mounted with the clear half towards the centre of the PMT and the other with the clear part towards the edge, as shown in Figure 2.4. A collimated beam of 511keV gamma rays from a ^{68}Ge source was directed at only one of the crystals. A 511keV gamma absorption event in that crystal was identified by both energy discrimination (using a window of 350-650keV) and coincidence timing with a sodium iodide (NaI(Tl)) detector. The anode signal from the other side of the PMT was connected to the analogue-to-digital converter (ADC) input of a multichannel analyser (MCA) which was gated by 511keV events in the irradiated crystal. When the clear side of irradiated crystal was coupled to the centre of the PMT, a distinct peak with a maximum at 86keV and FWHM of 52keV was observed in the other side of the PMT . This represented a 16.6% cross talk signal. Integrating the peak from 50keV to 350keV confirmed that a cross talk event was recorded for 94% of the 511keV events observed in the irradiated crystal. When the clear side of the irradiated crystal was coupled to the edge of the PMT very few cross talk events were recorded. Only 5% of the observed 511keV events recorded in the irradiated crystal gave a response in the opposite sector in the range 50-350keV. These results demonstrated that the optical cross talk in the

Figure 2.4: Detector configuration used to study optical cross talk spatial dependency. Two 30mmx20mmx10mm BGO crystals were coupled to the dual PMT. Scintillation light entered the PMT window only from half of the crystal because of the use of a mask, as shown. 94% of the interactions in crystal C1 resulted in a cross talk pulse in sector B, while an interaction in crystal C2 resulted in a cross talk pulse in sector A only 5% of the time.

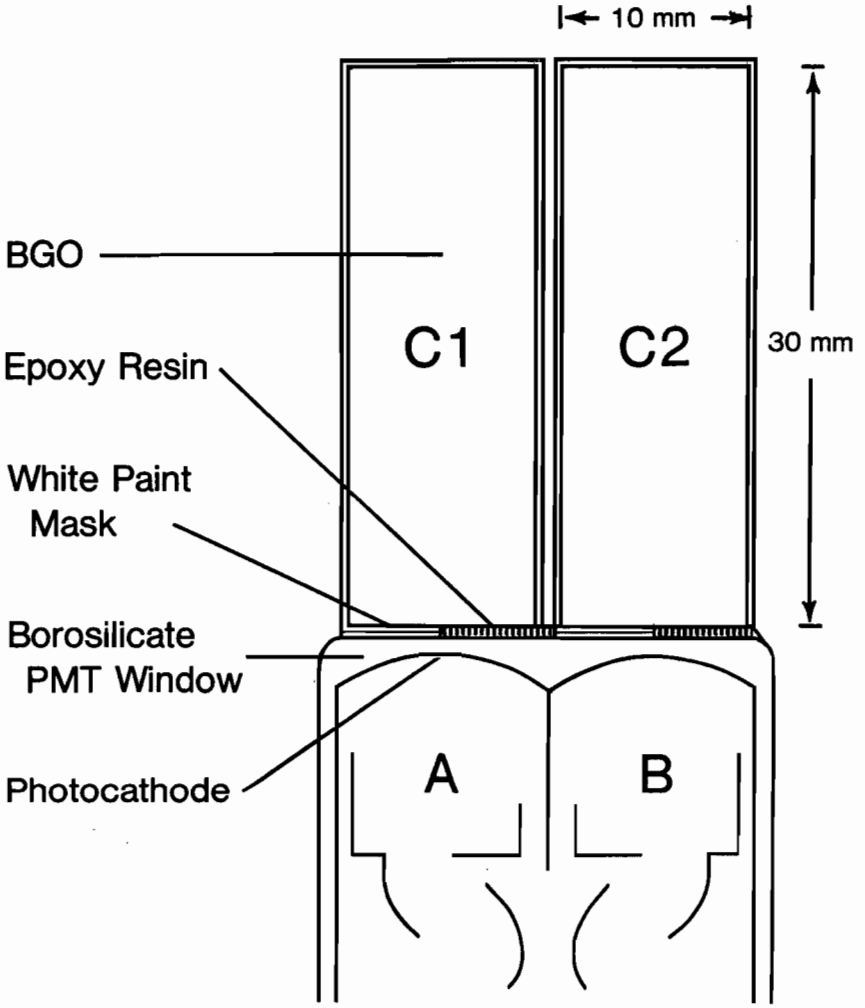
10 mm
BGO
Epoxy Resin
White Paint
Mask
Borosilicate
PMT Window
Photocathode
C1
C2
30 mm
A
B

R1548 would appear to provide a very simple scheme for crystal identification when four narrow crystals are coupled to the PMT.

Having made these observations, a number 4.5mm-wide BGO crystals were acquired. Four 30x20x4.5mm^3 crystals were coupled with epoxy resin to the R1548 as depicted in Figure 2.5. With this arrangement, the effect of the cross talk and non-uniformity of the photocathode sensitivity on the annihilation radiation spectrum could be examined by comparing the spectra generated by 511keV absorptions in crystals coupled to the inside and outside of the PMT face. The crystals were coated with NE560 reflector and each was wrapped in aluminium foil. The PMT was covered in a black, light-proof, plastic and tape and then enclosed in a snugly fitting mu-metal shield. The entire module was then wrapped in black tape. Both the crystals and shield were held at the electric potential of the cathode of the PMT to prevent disturbances of the electrostatic field between the photocathode and first dynode. The anode of each sector was connected to a preamp and a voltage of +1150V was applied to the tube. The gain of each sector was adjusted, using a potentiometer at dynode seven, to give the same pulse heights for 511keV scintillations occurring in both sectors. The output of the preamp was fed into a delay amplifier and a SCA with a window set between 350 and 650keV. The delay amplifier output was fed into the ADC input of an MCA. The SCA output was shaped into a logic pulse that gated the MCA. A 1mm wide collimated gamma ray beam was directed at each of the two crystals on the same detector sector and a gated spectrum collected on the MCA. These are shown in Figure 2.6. From these spectra it is clear that the sensitivity of the

FIGURE 2.5 QUAD BGO DETECTOR

The proposed quad BGO detector for high resolution positron tomography. The R1548 dual PMT is coupled to four BGO crystals. The addition of points to the faces of the crystals increases the detection efficiency of the detector without degrading the spatial resolution uniformity.

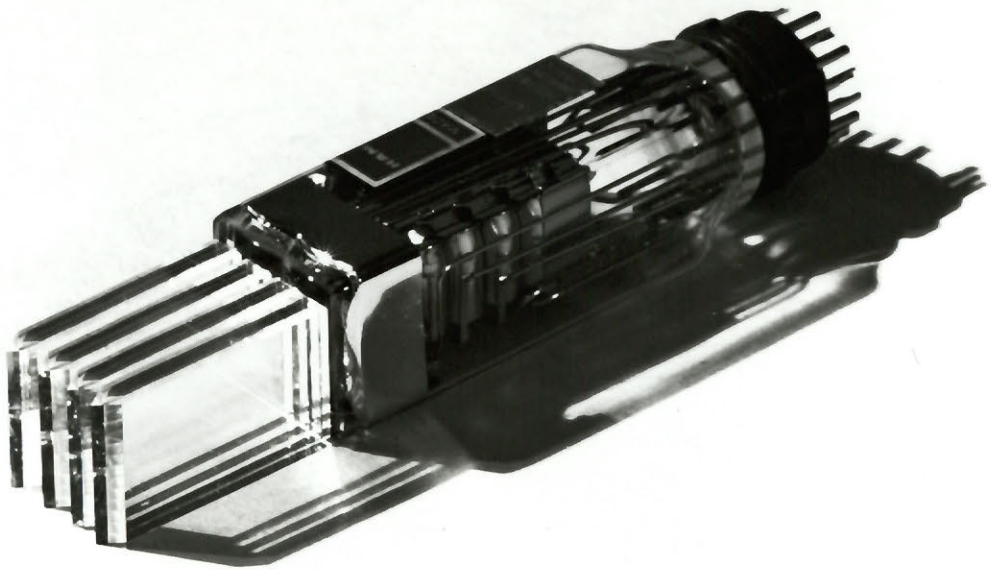

Figure 2.6(a)
350-650keV windowed pulses from scintillations in an outer crystal of the quad detector

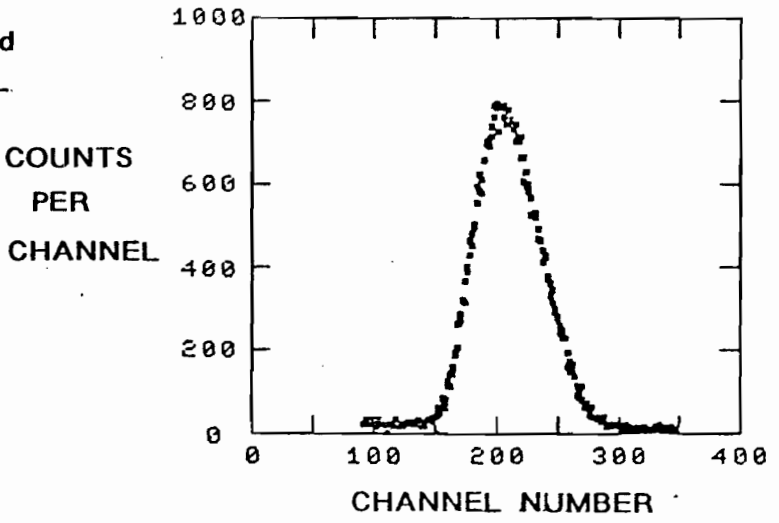

Figure 2.6(b)
350-650keV windowed pulses from scintillations in an inner crystal of the quad detector

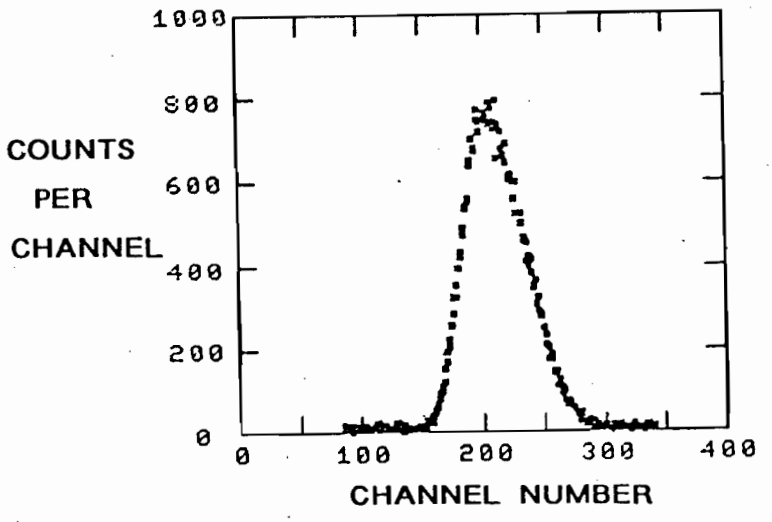

FIGURE 2.6 GATED 511keV PEAKS MEASURED WITH THE QUAD BGO DETECTOR

A collimated 511keV source was directed at the outer and inner crystals coupled to the same PMT sector. The preamp pulse branched into a delay amplifier and an SCA. The delay amplifier was connected to the ADC input of an MCA. The MCA was gated by the SCA and these spectra collected.

photocathode is uniform enough to permit the coupling of four crystals to the PMT without causing significant alterations in the spectra. Moreover, because the inner and outer crystal spectra are not significantly different, it is apparent that the optical cross talk from the inner crystal scintillations does not interfere with the spectrum of that crystal. One may conclude that crystal identification is achieved without a significant loss of energy resolution.

2.4 Crystal Geometry

The dimensions of the crystal influence the spatial resolution, efficiency, and the energy and timing resolutions of the detector. Because the spatial resolution was to be improved with minimal decrease in the packing fraction, the width of the crystals was determined by the PMT dimensions and the thickness of inter-crystal septa to be used. The PMT can accommodate four 5.5mm wide crystals when no septa are used (allowing for a .5mm wide inter-crystal space). Lecompte et al [1984] have shown, from geometrical arguments, that the insertion of thin tungsten septa improves the statistical signal-to-noise ratio (SNR) of an image at the maximum spatial frequency permitted by sampling theory. This is accomplished by the improved position identification of detected events, which results from the reduction in crystal penetration and inter-crystal scattering when septa are used. This reduction is caused by the absorption of gamma rays in the tungsten septa, especially for those entering the crystal at oblique angles (such as for gammas from a peripheral positron source in the tomograph). It was expected that the use of septa would reduce the resolution losses at the edge of the

tomograph. Lecompte et al [1984] have calculated that the optimum septum thickness for detectors with inter-crystal spacing of 4mm is around 1mm. Nahmias et al [1982], however, have experimented with the use of septa with 8mm wide BGO crystals, and have shown that approximately only a 10% improvement in the aperture function FWHM can be expected with the use of septa for crystals of that size. These results were corroborated by a monte carlo calculation performed by Derenzo [1981]. To investigate this further, the thickness of the crystals for this experimental detector was chosen as 4.5mm to allow for the insertion of 1mm septa, and thereby permit a comparison of detector configurations with and without septa.

The height of the crystal more or less defines the slice thickness and, therefore the axial resolution of a tomograph. The axial resolution FWHM is approximately half the slice thickness [Brooks et al, 1981]. Since there is no reason to assume that anatomical features are elongated in any preferred direction, the resolution should be the same in all three dimensions if quantitative images are to be obtained. In practice, however, most positron tomographs have detectors that are elongated in the axial direction to improve the image quality used to form an image of each slice, since the count rate is proportional to the slice width squared [Lupton and Keller, 1983; Derenzo, 1980; Tanaka et al, 1982]. Brooks et al [1981] have argued that in X-ray CAT scanners the axial resolution is typically more than five times the in-slice resolution and that the image quality is not greatly degraded there. It has become apparent, however, that although the image may appear adequate, the ability to perform accurate, quantitative, physiological

studies is greatly hindered without cubic quantitation volumes.[Strother, 1984] Two heights of the crystals chosen for the experimental detectors used in this study were 15mm and 20mm. The 20mm crystal would provide maximum packing fraction in the axial direction but poor axial resolution, whereas the 15mm high crystal would have an improved axial resolution and a low packing fraction. Ideally,two rows of 10mm high crystals would be aligned along the axial dimension of the PMT with a scheme similar to that which Derenzo [1984] or Charpak [1967] used to identify the slice on the PMT registering an event.

The length of the crystals greatly influences the efficiency, spatial resolution, and energy and timing resolutions of the detector.[Nahmias, 1982; Ishibashi et al, 1982] It has been shown [Nahmias, 1980] that, for crystals having widths as small as 8mm, a 25% increase in the intrinsic peak efficiency can be expected if the crystal length is increased from 30mm to 50mm, keeping the other dimensions constant. Unfortunately, as the crystal is lengthened, the light output decreases with a corresponding loss of energy and timing resolution. This effect becomes more important when very narrow crystals are used. Perhaps of greater concern is the loss of spatial resolution that is a consequence of increased crystal penetration of gamma rays from peripheral sources and increased inter-crystal scatter. Obviously, a trade-off between resolution and efficiency must be made. Figure 2.7 is graph of the detection efficiency of a 5x10xdmm^3 BGO crystal as d, the length, increases from 10 to 50mm. The values were calculated by Derenzo [1982] using a monte carlo simulation. These calculations tend to suggest

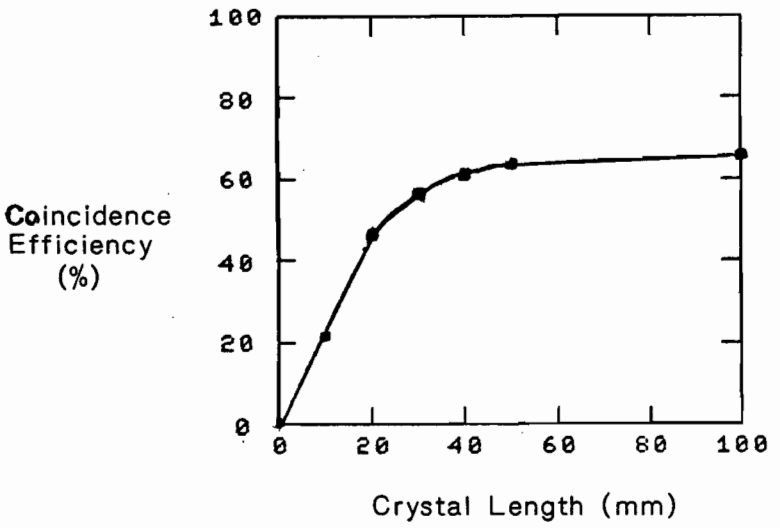

Figure 2.7: Graph of Coincidence Efficiency vs. Detector Length
The crystal cross section is 5 x 10 mm^2. The data points are generated by a monte carlo simulation [Derenzo, 1982]. In the simulation , 10,000 collimated 511keV photons uniformly irradiate the face of the detector array with a 0° angle of incidence. A valid detection requires at least a 100keV energy loss in one detector and less than 10keV loss in each of the others. The curve shown is an interpolation by eye.

that 30mm would be an appropriate length for a $5x10mm^2$ crystal cross section, and assuming little difference exists between these calculations and those for a $4.5x15m^2$ crystal, it would be an appropriate length for a $4.5x15mm^2$ crystal as well.

One approach to solving the problem of resolution losses at the edge of a tomograph is to taper the face of the crystal to a point. The gamma rays from sources at the periphery of the tomograph enter the detectors at oblique angles. Because the first detector they encounter presents them with less BGO than do detectors for which the angle of incidence is 0°, there is an increased probability of the off-centre rays penetrating the initial crystal encountered, and being absorbed in an adjacent crystal. If the face of the detector is tapered to a point, then more detector material is presented to angles rays than a flat faced crystal. Using this geometrical argument, one expects to observe an improvement in the spatial resolution at the tomograph periphery when points are added to the crystal face. In fact for moderately sized crystals (of the order of 10mm wide), the tapering of their faces has been shown to reduce resolution loss at the edges of an image [Lupton et al, 1984] but experimentation is still required to test the effect of this technique when it is used with narrow crystals separated by tungsten septa. Eight of the crystals had faces tapered to a point cut at an angle of 70°, as shown in Figure 2.8 The 70° angle of the taper was chosen so that the edge of the point would be aligned with a pair of gamma rays emitted along the tangent of a 13cm-radius circle concentric with a 46cm-diameter ring of detectors. This would ensure

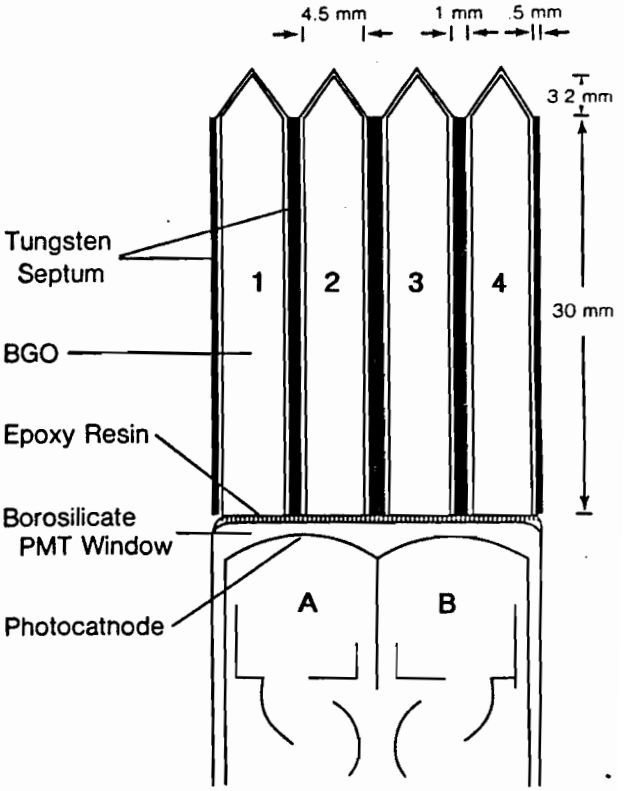

FIGURE 2.8: SCHEMATIC OF QUAD BGO DETECTOR WITH POINTED CRYSTALS

Four 4.5mm-wide BGO crystals were coupled to one dual PMT, as shown. Crystal identification was provided by optical cross talk between the centre crystals and the opposite photocathode. Pointed crystals increase the path length in the crystal of off-axis gamma rays.

The maximum oblique angle of incident gamma rays on a detector face from a source of activity of radius R_o is:

$$\theta = \sin^{-1}(R_o/R_D)$$

where R_D is the tomograph ring radius. The angle of the point is 2θ. For a reconstruction radius of 13cm and a ring radius of 46 cm, the angle of the point is 70°.

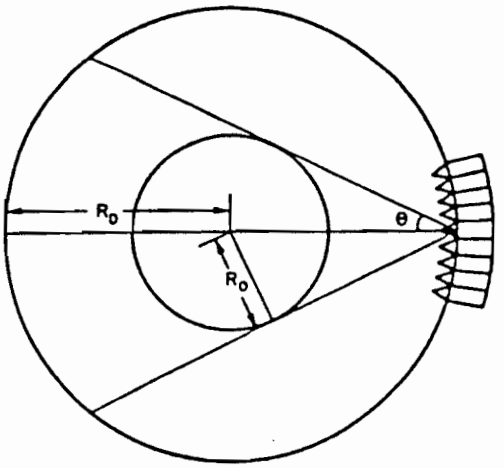

(the bottom diagram is from Cho et al, 1984)

that the gamma rays traverse at least 4mm of BGO in each detector.

2.5 Preamplifier

This study has not included an investigation of preamplifier optimization. The measurements performed throughout this work employed charge sensitive preamps of the design incorporated into the NaI(Tl) based Positome I detector. Briefly, it is an inverting, pulse shaping, FET input amplifier with an integration time constant of 500ns and a gain of approximately four.

2.6 Position Decoder and Test Coincidence Circuit

For the decoding technique proposed in Section 2.1 to be employed in a tomograph the discriminator that determines the time and energy of each gamma ray must be modified so that it can decode the position of the interaction crystal. A block diagram of the circuit used for decoding the signals from the test detectors used in this study is shown in Figure 2.9. The crystal identification modifications can be made by including a second energy discriminator which, for every event meeting the minimum energy requirement in one side of the PMT, examines the energy region 40-350keV in the other side of the PMT. Two circuits of the type depicted in Figure 2.9 were constructed using schottky TTL logic and incorporated into a standard double width NIM module. The timing characteristics of the electronics were enhanced by using LM360 voltage comparators and the schottky logic. A detailed circuit diagram of the contents of the Detector Decoder NIM module is presented in Figure 2.10. The two TTL timing outputs were AC coupled to simulate fast NIM logic

Figure 2.9: Block diagram of the timing, energy and positioning discriminator used with the four crystal-dual PMT detector. Lower level discrimination of the ENERGY SCA and upper level discrimination of the CROSS TALK SCA are both accomplished using the same voltage comparator. The use of the two NAND gates shown in the lower right corner allows the crystal number to be read directly in binary from the position bits when a signal appears at the timing output.

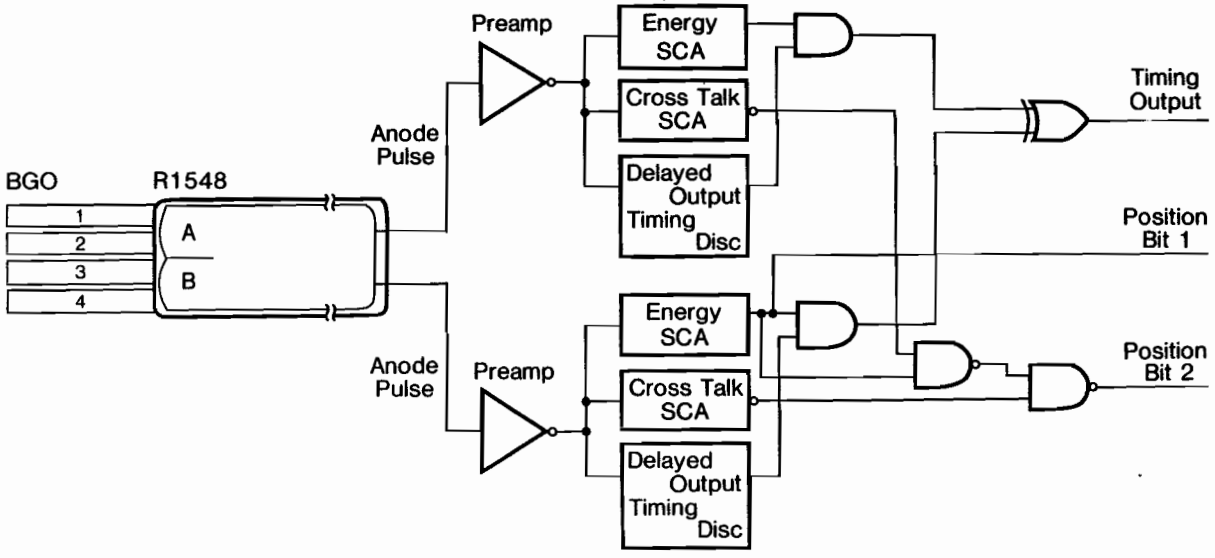
Preamp
Energy SCA
Cross Talk SCA
Delayed Output Timing Disc
Anode Pulse
BGO
R1548
1
2
3
4
A
B
Timing Output
Position Bit 1
Position Bit 2
Anode Pulse
Preamp
Energy SCA
Cross Talk SCA
Delayed Output Timing Disc

FIGURE 2.10 CIRCUIT DIAGRAM OF DETECTOR DECODER MODULE AND COINCIDENCE CIRCUIT

The Detector Decoder consists of two circuits described in Figure 2.9 and a detector pair identification circuit that is enabled by a TAC SCA pulse. The timing outputs of the detector decoder are input to the TAC, which has an internal SCA that sets a timing window. When a coincidence occurs, the position bits from the two detectors are latched through a quad D-type flip flop to a DAC. The four bits that are latched through form the binary representation of the codes described in Table 4.3. The timing of the 'Timing Output' is adjusted with the 5kohm potentiometer that determines the time constant for the 96S02 one shot. The four threshold levels are set by adjusting the 200ohm potentiometers shown on the second page of the diagram.

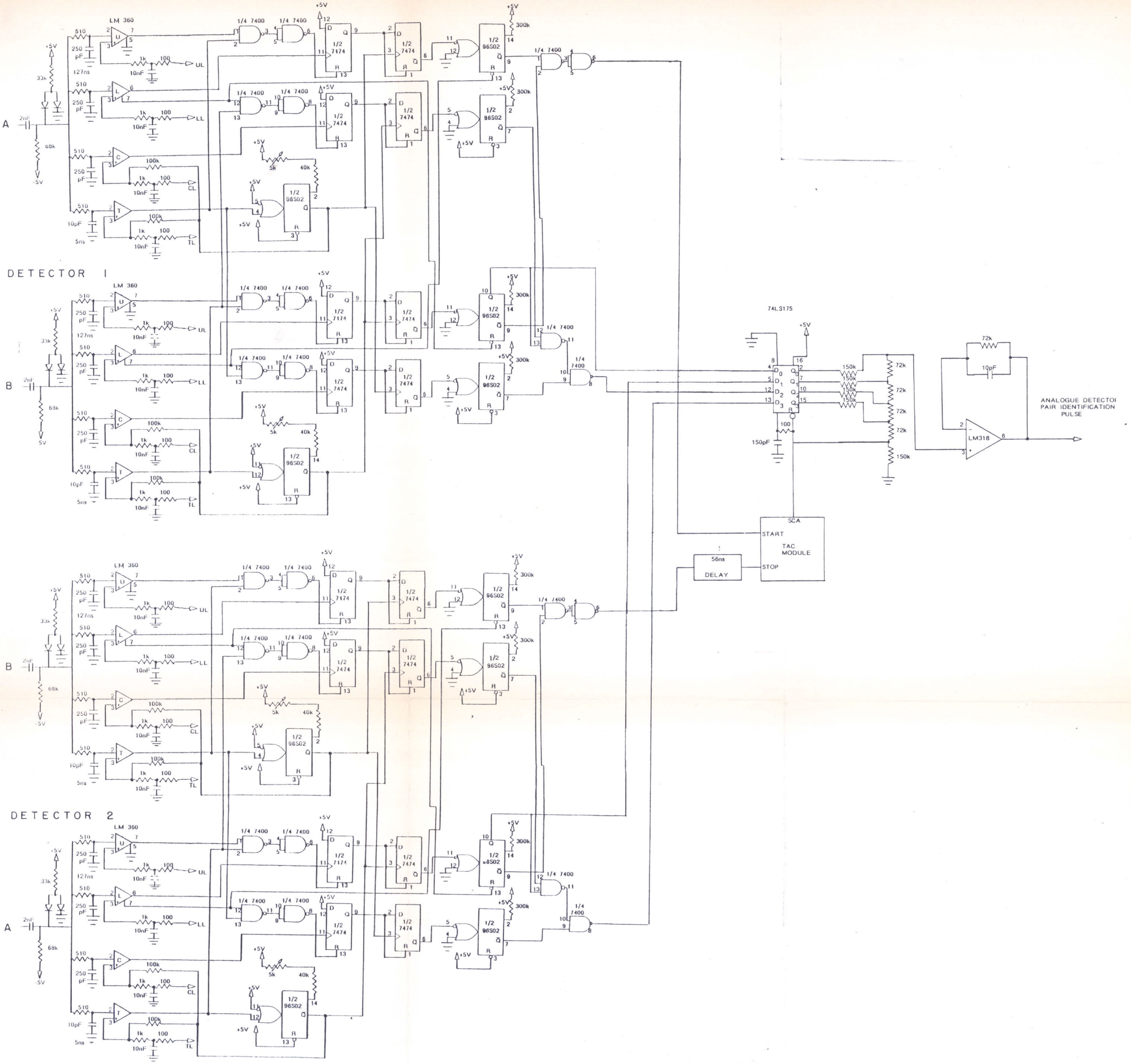
DETECTOR 1
DETECTOR 2
A
B
LM 360
1/4 7400
1/2 7474
1/2 96S02
74LS175
LM318
SCA
START
STOP
TAC MODULE
56ns DELAY
ANALOGUE DETECTOR PAIR IDENTIFICATION PULSE
UL
LL
CL
TL
+5V
-5V
33k
2nF
68k
510
250 pF
127ns
10pF
5ns
1k
100
10nF
100k
5k
40k
300k
150pF
72k
150k
10pF

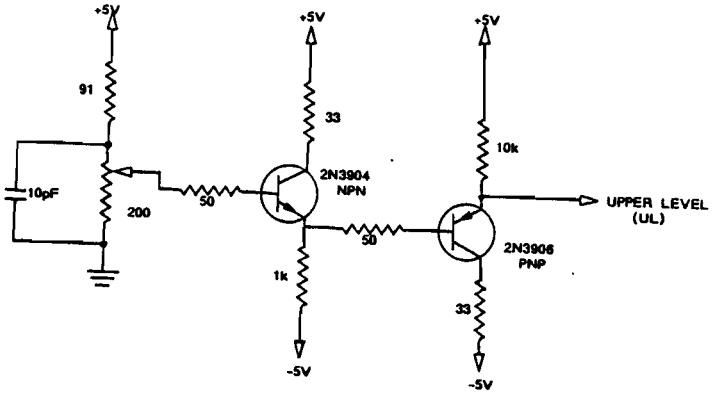
+5V
91
10pF
200
50
+5V
33
2N3904
NPN
1k
-5V
+5V
10k
50
2N3906
PNP
33
-5V
UPPER LEVEL
(UL)

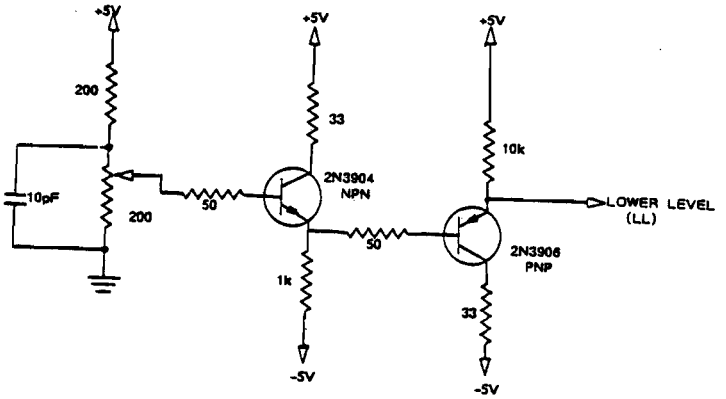
+5V
200
10pF
200
50
+5V
33
2N3904
NPN
1k
-5V
+5V
10k
50
2N3906
PNP
33
-5V
LOWER LEVEL
(LL)

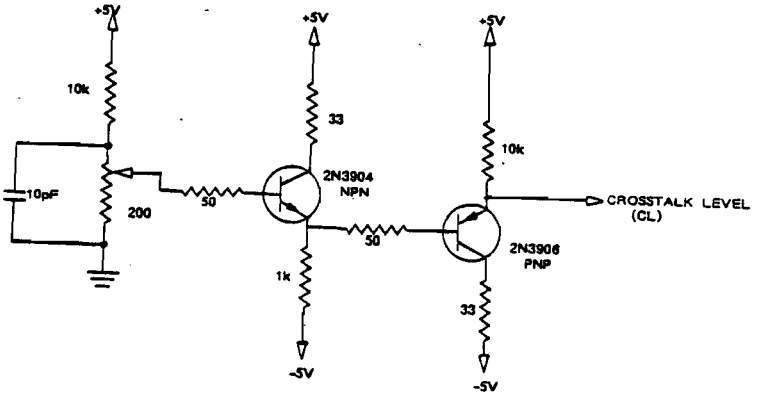
+5V
10k
10pF
200
50
+5V
33
2N3904
NPN
1k
-5V
+5V
10k
50
2N3906
PNP
33
-5V
CROSSTALK LEVEL
(CL)

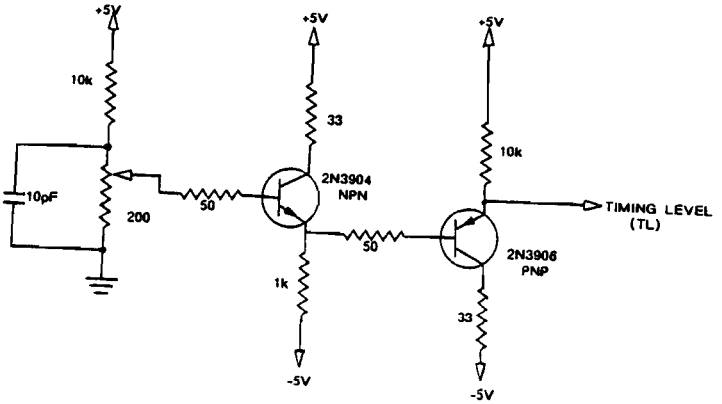
+5V
10k
10pF
200
50
+5V
33
2N3904
NPN
1k
-5V
+5V
10k
50
2N3906
PNP
33
-5V
TIMING LEVEL
(TL)

levels. The Detector 1 timing output was fed into the start channel of a Canberra Model 1443A time-to-amplitude converter (TAC) and the Detector 2 timing output was fed through a 56ns delay before being input into the stop channel of the TAC. The SCA of the TAC was used to set the coincidence window of the system. The TTL pulse emitted from the TAC SCA was fed back into the Detector Decoder module and used to latch the four position bits of the two detectors through a quad D-type flip-flop. The latched data were then transferred to a digital-to-analogue (DAC) converter which produced an analogue pulse that had one of sixteen possible discreet pulse heights. A one-to-one correspondence existed between the sixteen pulse heights and the sixteen possible coincidence detector pairs in the two quad detector system. The analogue detector pair identification pulse was then sent to the ADC input of a Tracor-Northern Model 7200 multichannel analyser (MCA). The MCA counted the number of coincidences that each of the sixteen detector pairs registered, binning them into sixteen different channels. The dead time of this total system was approximately 5 microseconds, which was adequate for the count rates used for measurements performed in this study. This dead time was almost entirely due to the TAC and MCA dead times and does not represent the dead time of a PET system incorporating this detector. Such a system would have a dead time an order of magnitude less than this. The advantage of using this circuit was that coincidences from all sixteen detector pairs could be counted during a single experiment and under identical conditions.

The timing calibration of the TAC was performed by using the same Detector Decoder timing output signal for the start and stop channels, with the signal passing through a precision delay box prior to entering the stop channel. The delay box used was the Canberra Model 2058 NSEC Delay which, according to the manufacturer, has a typical precision of 20ps per engaged switch and a maximum deviation of 100ps per engaged switch. For a 56ns delay, three switches were engaged, therefore a precision of the order of 50ps was expected. The Canberra Model 1443A TAC has a precision of less than .05% of the selected timing range, according to Canberra. The range used for these measurements was 200ns, therefore the upper limit of the TAC's precision was expected to be 100ps. The TAC pulses produced in this calibration procedure were analysed by the TN7200 MCA. They exhibited a distribution with a FWHM of (360$\pm$70)ps.

The timing jitter introduced by the Detector Decoder was measured by using the same preamp pulse as an input for both Detector 1 and Detector 2 channels in the decoder. The signals from the two timing outputs were then fed into the TAC and the TAC pulses analysed by the TN7200 MCA. The dispersion of these pulses was (1.4$\pm$.3)ns FWHM. This timing jitter was considered acceptable since the coincidence timing resolution of two different BGO detectors viewing a positron source was expected to be more than 5ns FWHM. Because the component dispersions add in quadrature, a 1.4ns FWHM jitter contributes less than 5% to a system having a 5ns FWHM dispersion.

CHAPTER THREE

Detector Evaluation

3.1 Introduction

The detector pictured in Figure 2.5 and described in the last paragraph of Section 2.3 was characterized with respect to its cross talk properties, efficiency relative to the Positome III detector, energy and coincidence timing resolutions, and the spatial resolution of the quad detector and a single crystal detector of the same dimensions for a centred line source.

3.2 Optical Cross Talk Characteristics

The uniformity of the optical cross talk characteristics was tested in sample PMTs by coupling a single crystal to one of the four positions on the face of the PMT, as shown in Figure 2.8. Having carried out tests with the crystals in that position, the crystal was moved to the next position and the measurements repeated. In all, four PMTs (eight sectors) were tested in this way. This use of a single crystal eliminated the component of cross talk related to inter-crystal Compton scattering and therefore provided a means of examining only optical cross talk. An experiment similar to that described in the Section 2.3 was performed. This time, however, no collimation of the gamma rays was required and only energy discrimination was used to define a 511keV event in the crystal. This experiment revealed that the optical cross talk was fairly uniform in the PMTs tested. The inner crystal cross talk peaks

were distributed about a mean of 97keV with values ranging between 72keV and 130keV. The FWHM of these peaks is 62keV. The crystal identification error was examined for both false positive and false negative cross talk events by varying the lower discrimination level. The identification error was optimized by setting the discrimination level at an energy where the false positive and false negative errors were equal. Typically this optimization was achieved by discriminating against cross talk events and noise pulses lower than approximately 40keV. The experiment demonstrated that, by setting the cross talk window between 40keV and 350keV, misidentification of a crystal due to the imperfection in the optical cross talk identification scheme occurred for 2% of the 511keV events registered in the crystal.

3.3 Inter-crystal Cross Talk

The ability to correctly identify the crystal of interaction is strongly influenced by the amount of inter-crystal Compton scatter. This effect is particularly important when narrow crystals are employed, as in this design. The overall cross talk characteristics, including scatter, crystal penetration and optical cross talk, were studied by coupling four narrow crystals to the face of the R1548 as shown in Figure 2.8 and performing a series of experiments similar to that described in the Section 2.3. In the first experiment a detector consisting of four crystals with flat, rectangular faces and without septa was tested. A collimated source of 511keV gamma rays was directed along the axis of the outer (1) and then the inner (2) crystal coupled to sector A of the PMT.

An ungated spectrum of the output of sector A showing the 511keV peak is shown in Figure 3.1(a). The output from PMT sector B was connected to the ADC input of an MCA and was gated by a SCA connected to sector A covering the energy range 350-650keV in coincidence with a NaI(Tl) detector. Figure 3.1(b) shows the gated spectrum of the output of sector B when the gamma ray beam was directed at the outer crystal (1) of sector A. Figure 3.1(c) shows the cross talk peak present in the gated spectrum of the output of sector B when the inner crystal (2) of sector A was irradiated. In the case where crystal 1 was irradiated, only 12% of the 511keV events registering in sector A produced a signal between 40keV and 350keV in sector B. From the results of the optical cross talk encoding errors previously discussed, one can conclude that most of this 12% error is due to Compton scatter. Probably 10% is due to Compton scatter and 2% to encoding error. When crystal 2 was irradiated, 90% of the 511keV events produced a sector B response in the same range. The experiment was repeated with the gamma ray beam directed 20° off the detector axis such that gamma rays not absorbed by crystal 1 or 2 would pass into crystal 3 and perhaps crystal 4. The off-axis beam corresponded to the tangent of a 7.8cm-radius circle concentric with a 46cm-diameter detector ring, i.e. a point 7.8cm from the centre of a tomograph. The results of this experiment are summarized in Table 3.1.

To reduce the effects of Compton scatter between crystals, inter-crystal septa are often used. The effectiveness of this technique was tested for this design by repeating the above experiments with 1mm tungsten sheets placed between the crystals. The results, presented in

FIGURE 3.1 Full Energy and Cross Talk Spectra of the QUAD BGO Detector

Figure 3.1: (a) Gamma ray spectrum from a ^{68}Ge collimated source directed at crystal 1 coupled to PMT sector A.

(b) Spectrum of pulses from the output of PMT sector B,when gated by 511keV events occurring in crystal 1 which was coupled to the outside of side A. The spectrum shows noise pulses and some cross talk events.

(c) Spectrum of pulses from the output of PMT sector B,when gated by 511keV events occurring in crystal 2 which was coupled to the inside of side A. The spectrum shows the distribution of cross talk pulses.

The spectra in Figures 3(b) and 3(c) have the same vertical scale, and all three spectra have the same horizontal scale.

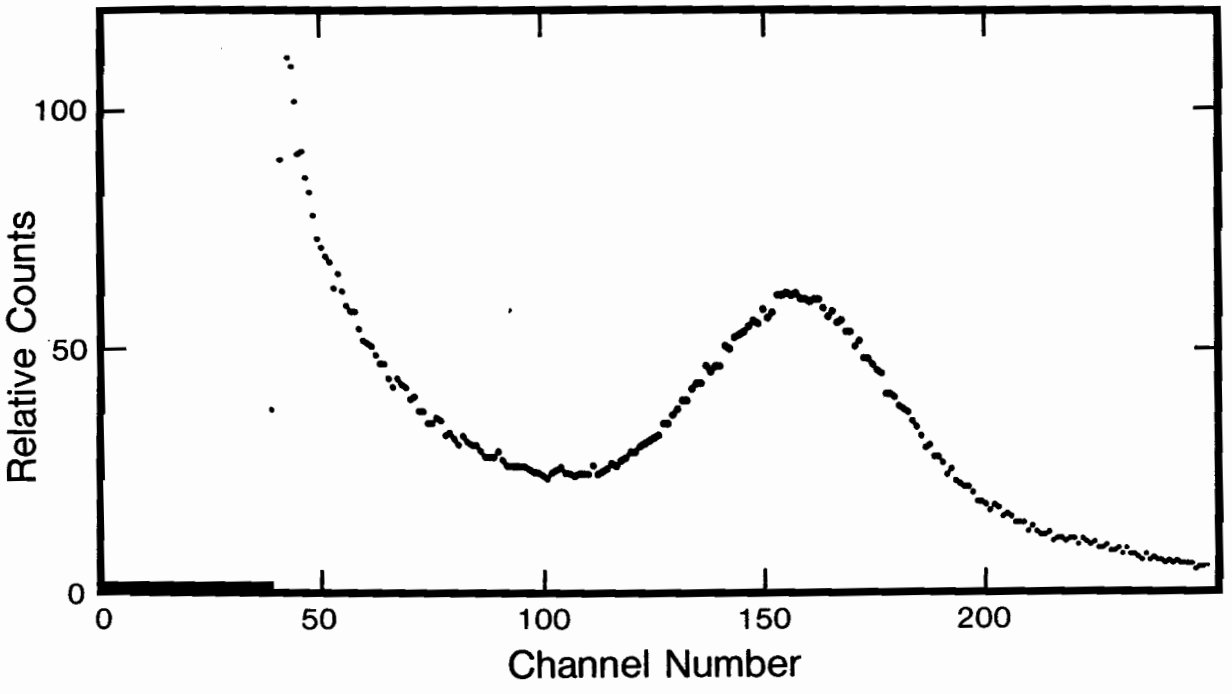

FIGURE 3,1(a)

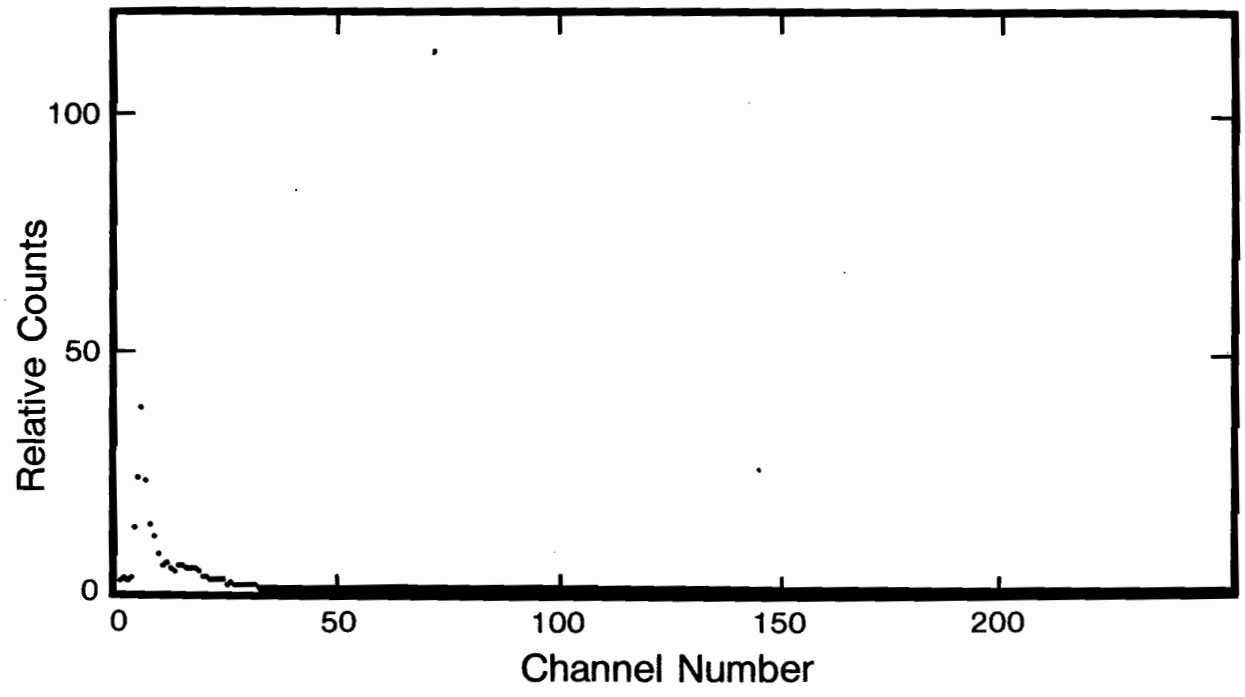

FIGURE 3.1(b)

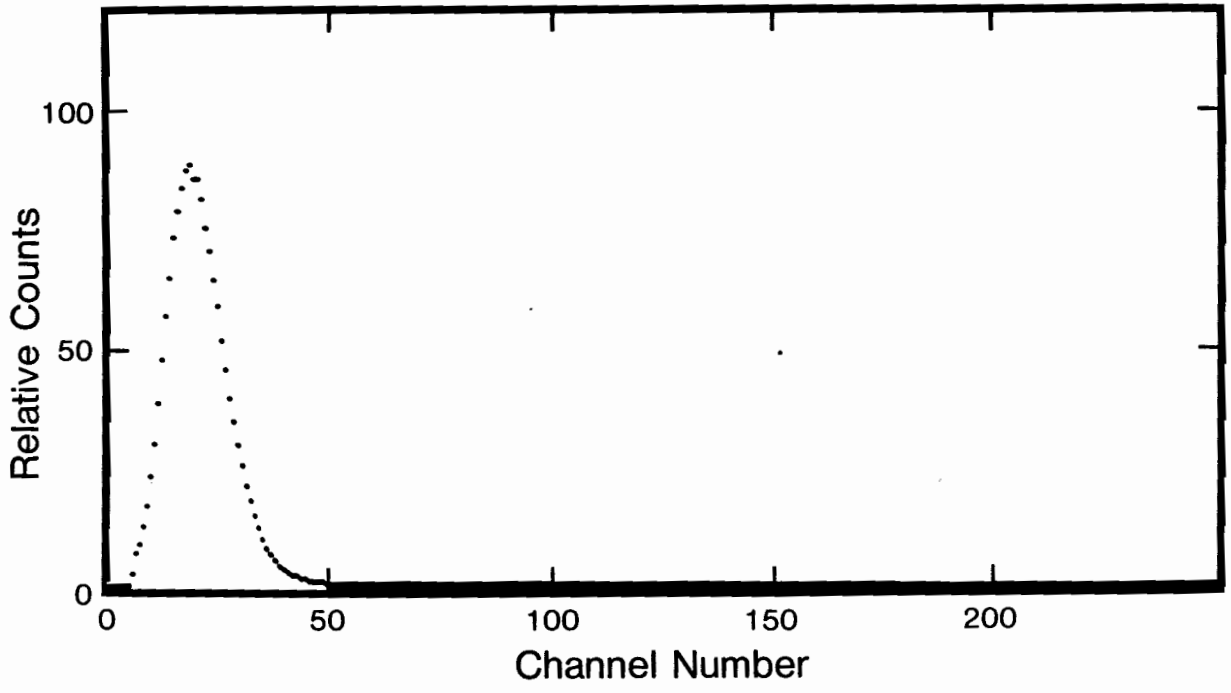

FIGURE 3.1(c)

Gamma Ray Incident Angle	Interaction Crystal (see Fig.2.8)	No Septa	1mm Tungsten Septa
0°	flat face position 1	11.9±.5	7.3±.2
0°	flat face position 2	90±1	94±1
20°	flat face position 1	49±2	28±1
20°	flat face position 2	83±5	89±3
0°	tapered face position 1	8.8±.4	8.9±.5
0°	tapered face position 2	91±1	93±2
20°	tapered face position 1	36±2	18±1
20°	tapered face position 2	93±4	93±3

Table 3.1: Percent Cross Talk in a Four Crystal-Dual PMT Detector

The values in the table represent the percentage of 511keV events interacting in crystals 1 and 2 coupled to sector A of the PMT that also give rise to a cross talk event in sector B in an energy window of 40keV-350keV.The cross talk is due to optical cross talk, compton scatter and crystal penetration of gamma rays.

Table 3.1, show that some reduction in the rate of cross coupled events related to compton scatter from an axial beam can be achieved by using the septa, and that use of such septa can also reduce significatly the rate of cross coupled events related to the scatter of off-axis gamma rays.

It was expected that a reduction in the rate of cross coupled events related to off-axis gamma ray penetration would be possible with the addition of a point to the face of the crystal. A monte carlo simulation of the shielding effects of 40° points on 4mm-wide BGO crystals reveal that a 25% drop in crystal penetration of gamma rays with more than 350keV can be expected for a 20° incident angle. For a 60° point a 17% drop can be expected for a 20° incident angle.[Cho et al, 1984] The reason for this is as follows: a gamma ray incident on a "flat" crystal at 35° (the angle of the point of the crystals used in these experiments) to the axis, corresponding to a point 13cm from the centre of a tomograph, would pass through an average of 3.9mm of BGO for a crystal 4.5mm wide. A 70° point increases the average to 5.9mm. The minimum path length is increased from essentially zero to 3.9mm for a gamma ray which is directed at the corner of the crystal. To test how well this scheme might work the above experiments were repeated for the pointed crystals, with the results summarized in Table 3.1. A significant improvement in the cross talk characteristics for off-axis gamma rays was observed when tungsten septa were used in conjunction with tapered crystals. These results are consistant with the simulation performed by Cho et al [1984].

3.4 Relative Intrinsic Peak Efficiency

The intrinsic peak efficiency of the quad BGO detector was measured relative to that of the type of detector used in the Positome III ring. The Positome III detector consists of a trapezoidal BGO crystal 30mm deep and with 30x18mm^2 front face and 30x20mm^2 rear face coupled to a Hamamatsu R1213 PMT. Since the effects of inter-crystal scattering were to be included in this measurement, a module comprising the Positome detector sandwiched between two identically cut BGO crystals and 1mm thick tungsten septa was assembled. The narrow BGO detector used for the measurement consisted of one 30x20x4.5mm^3 flat faced crystal coupled to the outer edge of an R1548 PMT with three similar crystals, separated by 1mm tungsten sheets, placed on either side of the active crystal. The high voltage applied to the Positome detector was the same as that used in the working system, +1650V, and the voltage applied to the R1548 of the narrow detector was set at +1250 in order to give similar pulse heights as the Positome detector. The preamp of Section 2.5 was used for this measurement. It was connected directly to the ADC input of a TN7200 MCA. An energy calibration of each detector was performed using the 511keV and 1275keV gamma rays of a ^{22}Na source. With these calibrations, an energy window between 350$\pm$20keV and 700$\pm$10keV was set up in the MCA memory for each of the two detectors. A ^{68}Ga source, obtained from a ^{68}Ge generator and dissolved in water, was encapsulated in a 1.2mm outer diameter (OD), .6mm inner diameter (ID), glass capillary tube. The thread of the ^{68}Ga-H_2O in the tube was 2cm long. The capillary tube was fastened to a vernier microdrive unit (David Kopf

Instruments) capable of positioning the source with an accuracy of ±.05mm . The source was placed along the axis of the detector of interest at a distance of 155±1mm and the count rate of full energy peak events determined. The source was then moved to 150mm and 160mm along the crystal axis and the measurements repeated. Returning the source to the 155mm position along the crystal axis, the source was then moved 10mm on either side of the crystal axis and the measurements repeated. To correct for events related to gamma rays scattered off of the walls, bench surface etc., an 80mm thick lead brick was placed between the source and the detector before moving the source to a new position, and the full energy peak count rate determined. It was assumed that, with the lead in place, any gamma rays entering the detector had been scattered from the surrounding surfaces. The count rate for unscattered gammas was obtained by subtracting the count rate with the lead brick in place from the count rate without the lead. The error in placing the detector was estimated to be ±1mm and the experiment, as described above, was repeated three time in order to average out any detector positioning errors. The ^{68}Ga line source was used to obtain good statistics (the statistical error was less than .5%), but to ensure that the line source geometry did not interfere with the measurement, a smaller positron source (5mm long, 1.2mm OD) was used in a fourth run of the experiment. The measurements using it yielded results consistent with those of the measurements using the longer source, thereby indicating that the use of the 20mm long line source did not affect the efficiency measurement. The ratio of the peak efficiency of the narrow detector to that of the Positome detector was (20.7±1.2)%. One would expect that

this ratio should be approximately equal to the ratio of the area of the narrow crystal face to that of the Positome crystal face, which is 16.7%. In fact, the narrow crystal exhibits an efficiency (24.0±1.4)% higher. This higher intrinsic peak efficiency is most likely due to improvements in the BGO fabrication techniques that have occurred since 1977 when the Positome III crystals were produced.

3.5 Energy and Coincidence Timing Resolutions

The energy resolution of the narrow detectors is unfortunately quite poor, as can be seen in Figure 3.1(a). The spectrum in Figure 3.1(a) is that of annihilation radiation irradiating one of the four crystals in the quad detector. When the preamp pulse was connected directly to the ADC input of the MCA, the resolution was measured as 30±1%. The use of a spectroscopy amplifier with a time constant of 2μs yielded a FWHM of 28±1%, indicating that electronic noise generates approximately a 10% FWHM energy resolution broadening. Most of the energy resolution broadening problem lies primarily with the inefficiency of the collection of light from a long, narrow crystal coupled with the fact that BGO has a poor light yield to begin with. This is evidenced by a simple application of equation 2.1 for the parameters of the detectors used in these resolution measurements. The relative index of refraction between BGO and the PMT window, assuming ideal coupling with the epoxy resin, at 500nm (the mean of the BGO emission spectrum [Lorentz, 1982]) is 1.4 and therefore K_1 is 0.29. The quantum efficiency, K_2 of the R1548 at 500nm is .20. A_o/A for the 30x20x4.5mm^3 BGO crystal is .055. The

value of η for TiO_2 paint at this wavelength is 0.89 [Okajima et al, 1982]. Insertion of these values into equation 2.1 produces a light detection efficiency of 0.028. Using Lorentz's [1982] value of BGO light yield, $(.51\pm.26)\times10^4$ photons are produced when 511keV is deposited in the crystal. Therefore, 140 ± 70 photoelectrons are emitted at the photocathode, and assuming Poisson statistics hold, this implies that statistical variation in the number of photoelectrons emitted for each 511keV event accounts for an energy resolution of between 16% and 28% FWHM. The large range is due to the great uncertainty in the scintillation efficiency of the crystal. A similar calculation for the $30\times20\times10mm^3$ detector as described in Section 2.3, and used to evaluate the R1548, indicates that there is a statistical contribution of between 12% and 22% FWHM to the energy resolution. The measured value was $(25.6\pm.2)$%. Together, these measurements indicate that statistical fluctuations of the number of photoelectrons account for most of the resolution broadening, about 80%. The rest of the broadening is due to a combination of other effects, such as variations in the scintillation and light collection efficiencies over the volume of the crystal, fluctuations in the energy transformation channels through which the incident gamma ray energy is converted into optical photons, variations in the photocathode sensitivity over the active area, statistical fluctuations in the first dynode collection of the photoelectrons and electron multiplication, and electronic noise.

The coincidence timing resolution of the quad BGO detector was measured using the following electronic configuration. The PMT anode was

fed into the preamp and the time pick-off was by a leading edge discriminator with a threshold at 1% of the pulse height. The energy window was between 400 and 600keV. A ^{68}Ge source produced the annihilation radiation for these measurements and the high voltage applied to the R1548 was +1150V. The leading edge discriminators used were those incorporated into the Detector Decoder module. The timing spectrum is presented in Figure 3.2. The FWHM is 10ns. One must conclude that most of the resolution loss is due to time jitter effects, since the small energy window reduces the time walk introduced when different pulse heights contribute to the timing spectrum. The results of the energy resolution measurements demonstrate that photoelectron statistics were low for this detector (less than 100 photoelectrons from a 511keV interaction.) One consequence of this statistical fluctuation in the photoelectron number and time of creation is time jitter. Another contribution to the time jitter is the electronic noise in the preamp. The use of a very low noise preamp would minimize the jitter problems that are already aggravated by the small number of photoelectrons. But it is more important to maximize the photoelectron statistics. Okajima et al [1982] were able to achieve 2ns FWHM BGO-BGO timing spectra by optimizing the diffuse reflector coating. They roughened the crystal surface slightly and applied $BaSO_4$ with polyvinyl alcohol. The use of such a coating, in addition to the use of a low noise preamp is recommended.

3.6 Spatial Resolution Measurement

The spatial resolution of the detector configuration composed of four tapered crystals separated by 1mm tungsten septa was measured for

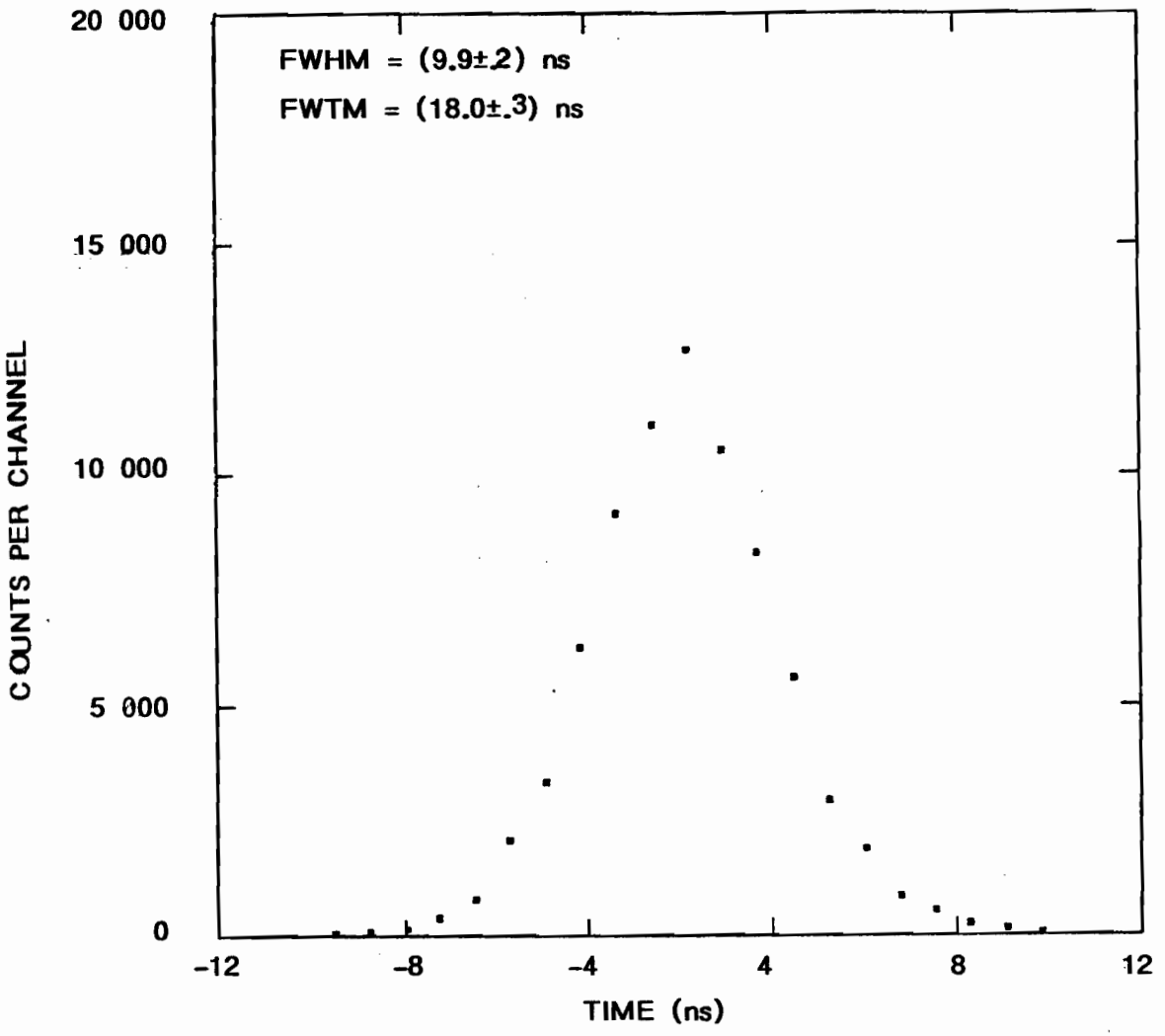

FIGURE 3.2 COINCIDENCE TIME SPECTRUM OF BGO QUAD DETECTORS

The Detector Decoder timing output pulses were fed into a TAC with a 56ns delay before the stop channel. The time calibration, described in Section 2.6, is 1.53±.05ns/channel for this measurement.

gamma rays directed along the crystal axis. A 1.2mm-diameter ^{68}Ga line source was placed midway between the four-crystal detector and a second detector composed of a single 4.5mm-wide crystal coupled to a PMT. A bank of three narrow BGO crystals, separated by 1mm tungsten sheets, was placed on either side of the four-crystal detector. This provided scattering conditions similar to those found in a ring of detectors. The two detectors were separated by a distance of 46cm and the line source was moved in 1.0mm steps in a direction perpendicular to the line joining the two detectors. The detectors were collimated with 13mm lead plates to restrict their view to a 2.4cm slice. The FWHM of the coincident response function of this setup was found to be 2.9mm and the FWTM was 6.2mm.

The coincidence response functions are presented in Figure 3.3. Figure 3.3(a) is the response function when a crystal coupled to the outside of the R1548 is in coincidence with the opposing narrow detector (i.e. crystal 1 or 4 in Figure 2.8), and Figure 3.3(b) is the response function when an inner crystal (i.e. crystal 2 or 3) is in coincidence with the opposing detector. The slight asymmetry apparent in these functions is due to the fact that the decoding circuit accepts events in which more than 350keV is deposited in two crystals coupled to the same R1548 sector. A detected event usually occurs when a gamma ray deposits more than 350keV in one crystal, but if the initial interaction occurs close to the crystal edge then it has a higher probability of scattering into the adjacent crystal. If both crystals are coupled to the same photocathode, then a gamma ray which deposits less than 350keV in one of

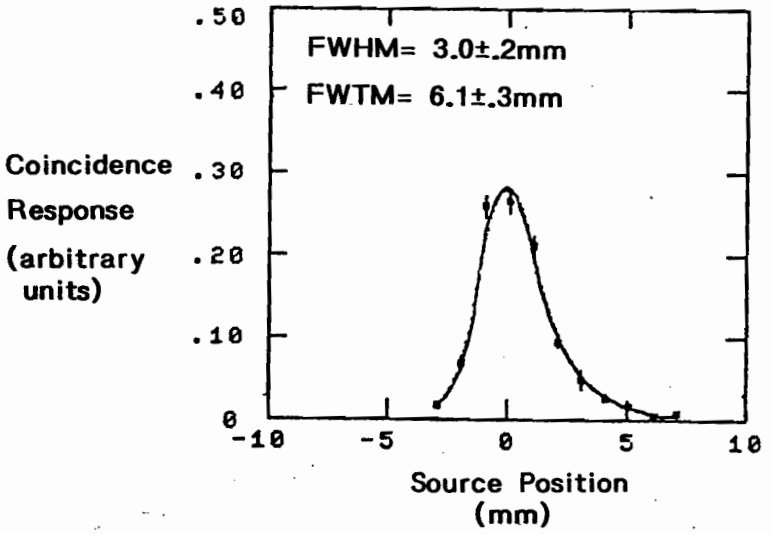

Figure 3.3(a): The coincidence response of an outer crystal of the quad detector and a single 4.5mm-wide detector.

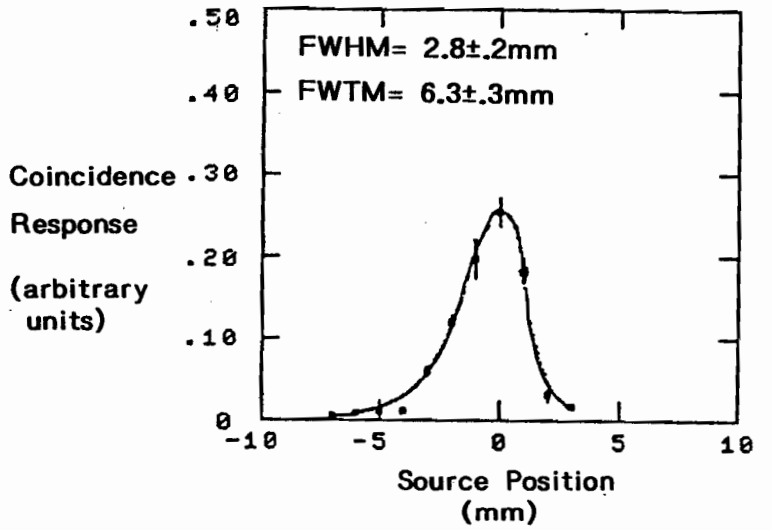

Figure 3.3(b): The coincidence response of an inner crystal of the quad detector and a single 4.5mm-wide detector.

FIGURE 3.3: COINCIDENCE RESPONSE FUNCTION OF A QUAD BGO DETECTOR AND A SINGLE 4.5mm-WIDE DETECTOR

A 1.2mm OD ^{68}Ga line source was moved in 1mm steps in a direction perpendicular to a line joining the faces of the two detectors. The vertical axis represents a normalized coincidence coint rate as the source moves past the detectors.

the crystals but more than 350keV in both crystals will be indistinguishable, as far as the decoding scheme is concerned, from a gamma ray which deposits more than 350keV in a single crystal. This shows up as an asymmetric broadening of the coincidence response function, with the broadening occurring on the side of the function related to the common-photocathode crystal edge.

CHAPTER FOUR

Aperture Function Measurements

4.1 Introduction

As pointed out in Section 2.4, there are currently two schools of thought with respect to the use of inter-crystal septa. Lecompte et al [1984] use calculations based on geometrical premises to argue that when septa are used, the statistical SNR at the maximum spatial frequency is greater than when they are omitted, even though the overall efficiency may be lower. Nahmias et al [1980], on the other hand, have performed experiments using 8mm-wide BGO crystals with and without septa. These demonstrate that little improvement (around 10%) can be expected in the aperture function FWHM if septa are used and they claim that the 20% drop in efficiency accompanying the use of septa does not justify this meagre improvement in resolution. Lecompte et al point out that the FWHM is not a satisfactory measure of the resolution since it does not take into consideration the tails of the aperture function. To deal with this problem, they have defined a 'spectral resolution', R, which accounts for all of the spatial frequency components of the aperture function (see Appendix Three):

$$R = \frac{[\int AF(x)dx\ ]^2}{\int |AF(x)dx|^2 dx} \qquad [4.1]$$

where: AF(x) is the aperture function normalized by its integral over all x and its peak positioned at x=0.

If R is used to describe the spatial resolution, then they claim that a significant improvement in resolution is expected when septa are used. An improvement that is significant enough to improve the SNR at higher frequencies, because of improved annihilation position identification. To argue this point, they derive a spectral SNR (see Appendix Three):

$$SNR(\nu) = \sqrt{(a \cdot X_o)}\ |FT\{AF(x)\}| \qquad [4.2]$$

where: a is the incident radiation linear density.
X_o is the effective width of radiation of the detector.

Using a linear attenuation calculation to describe the interactions of the gamma rays irradiating a detector array, they have determined the geometrical effects of septa on the MTF (see Appendix Three for a definition of MTF), R, SNR, and the efficiency. If the front of the septa are receded slightly from the faces of the crystals, as shown in Figure 4.1, then the efficiency for angled rays can be improved without degrading the resolution. For each angle of incidence, there exists an optimum 'septum gap' for which the highest resolution is achieved. In addition, at a given angle of incidence, an optimum septum thickness exists with respect to maximizing the SNR at the maximum frequency of the system. Even though the efficiency drops, Lecompte et al show that, on geometrical grounds, the SNR at higher frequencies is improved for angled rays when septa are used.

A series of aperture function measurements were performed using the quad BGO detector with different septa-crystal configurations. The primary objective of these experiments was to determine whether or not

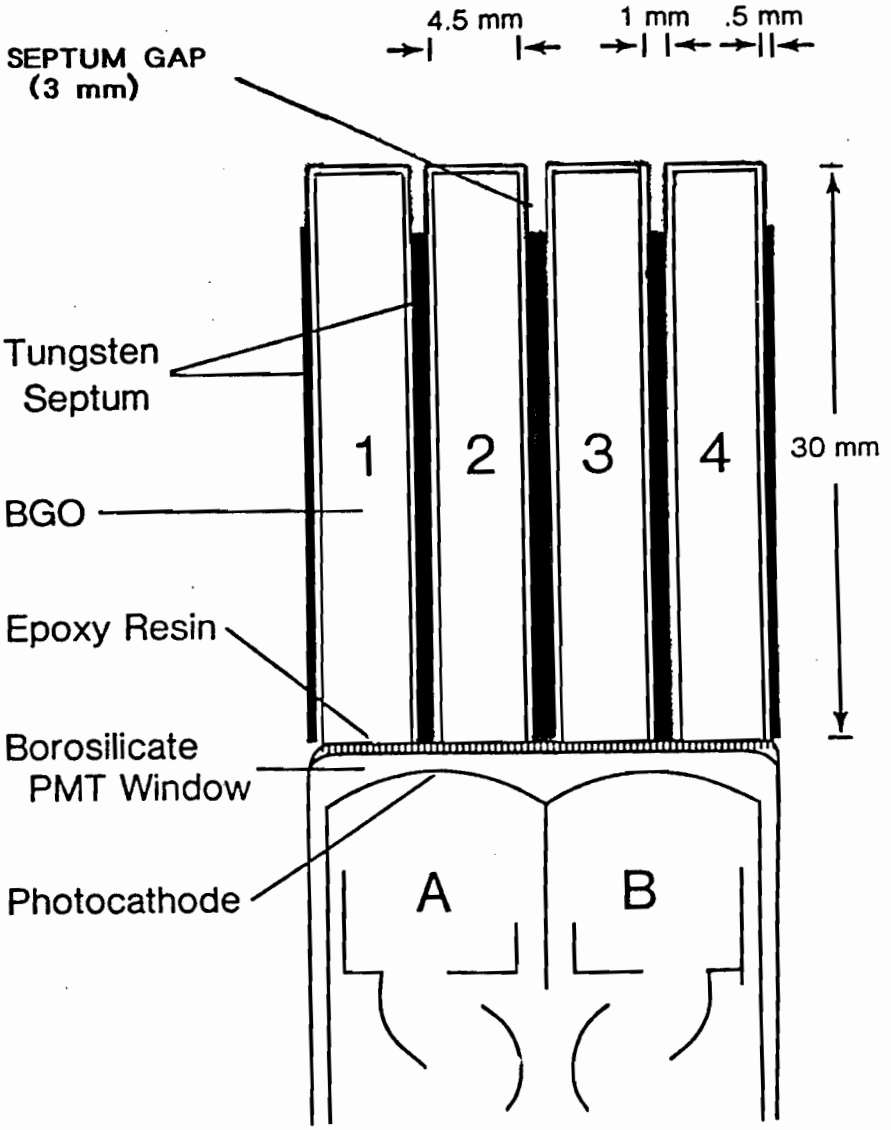

FIGURE 4.1 QUAD BGO DETECTOR WITH RECEDED SEPTA

According to the linear attenuation coefficient calculations of Lecompte et al [1984], introducing a 'septum gap' by receding the front of the septa from the crystal face improves the detection efficiency of the detector for angled rays without degrading the spatial resolution. The measurements involving flat faced crystals with septa used this configuration. The 3mm gap is optimum for 35° angled rays.

septa and/or tapered crystal faces are desirable in a final detector design. The use of R and SNR as defined by Lecompte et al are used to evaluate each configuration. Lecompte et al used the value of SNR calculated at the frequency equal to the reciprocal of the inter-crystal spacing when presenting their argument. The inter-crystal spacing of the quad detector is 5.5mm and therefore the SNR at .182mm^{-1} will be used to evaluate the various configurations. Twelve aperture function measurements were made in all. Four detector configurations were investigated: flat faced and tapered crystals with a 1mm air space between crystals and flat and tapered crystals with a 1mm thick tungsten sheet between crystals. The tungsten septum receded 3mm from the face of the flat crystals, as shown in Figure 4.1, and 3.2mm from the tip of the point of the tapered crystals as shown in Figure 2.8. The aperture function of each configuration was measured for a source associated with a diameter ray of a 460mm diameter ring tomograph both (a) at the centre and (b) 78mm off-centre, and (c) for a source associated with a chord ray situated 78mm from the centre of a ring tomograph (rays from such a source enter the detector array at an incident angle of 20°. These correspond roughly to rays emitted from activity situated at the periphery of a brain centred in the tomograph.) See Figure 4.2 for a diagram of the three positions of the source that were investigated. The experiments (a) and (c) were also simulated using the monte carlo code, APERT, which was developed by Keller and Lupton[1983] to model PET detector aperture functions. The simulation provides a theoretical frame of reference for these experiments and also enables one to deduce how much loss of resolution is introduced by the position encoding-decoding

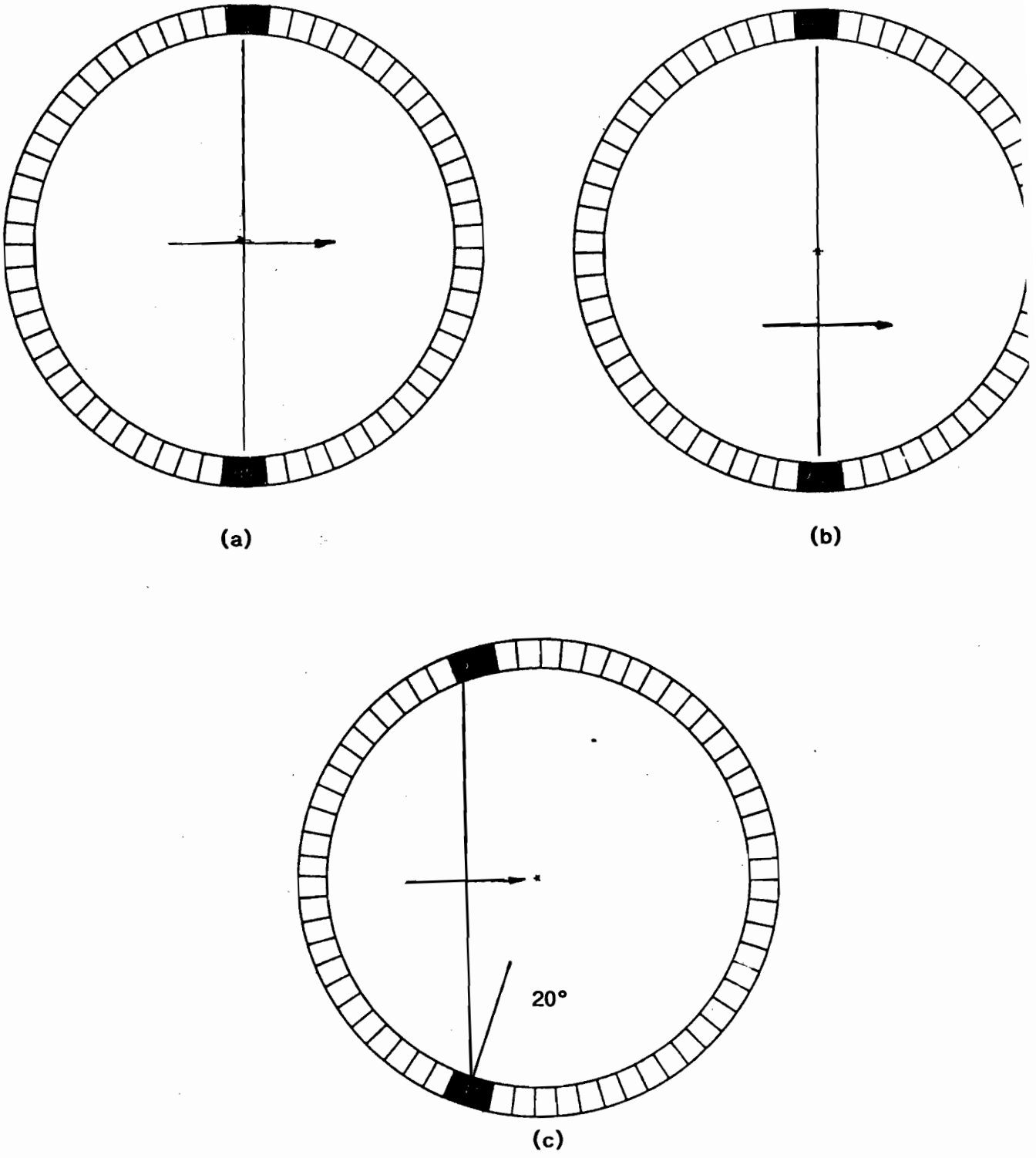

FIGURE 4.2 SCHEMATIC OF SOURCE–DETECTOR ORIENTATIONS FOR APERTURE FUNCTION MEASUREMENTS

The ring diameter is 460mm. The source motion is indicated by the arrows. The detectors under study are shaded in.

Compton scattering, as described by the Klien-Nishina formula of equation A2.4, is modelled using equal probability direction cosines groups that correspond to uniform 5keV wide energy groups. The photoelectric cross section, described by equation A2.5, is determined by fitting A x Energy^{-B} to published data. The gamma ray history in the crystal is generated by sampling the Compton and photoelectric absorption cross sections using standard monte carlo techniques.

The experimental set up, described in Section 4.3, is not identical to that of the simulation and this leads to discrepancies between the calculated and measured aperture functions. There are six major differences: the septa used in the experiment are pure tungsten, not Kennerium, there are short collimators in front of the detectors which could introduce scattering effects that are not accounted for in the simulation, half of the detector configurations tested have points, whereas the simulation is valid for flat faced crystals, receded septa were used with the flat crystals, the source used in the experiment has a significant width, and non-colinearity effects are non-negligible. The first two differences are assumed to have a negligible effect on the aperture function measurement. The effect of the points could be studied by using a geometrical model similar to that of Lupton et al[1984], but that model predicted little difference between the aperture functions of narrow crystals with flat and pointed faces. The fact that receded septa were used with the flat crystals but not in the simulation provides a means of testing the effectiveness of the septa gap, based on a comparison between the simulation and experiment. The effects of a

finite source width and gamma ray non-colinearity can be accounted for by convolving the monte carlo aperture function with functions describing the distribution of these two sources of broadening.

The source used in the experiment was encapsulated in a 1.5mm OD capillary tube. To account for the finite dimensions of the source, the monte carlo calculated aperture function was normalized with respect to its integral over all space and convolved with a rectangular function of unit area and with a width equal to the source OD, 1.5mm. The discussion in Appendix Two indicates that the angular distribution of a pair of annihilation gamma rays can be approximated by a gaussian with a FWHM of .5°. Using equation 1.1, the non-colinearity contribution for detectors separated by 460mm, as in this experiment, is 1.0mm. A gaussian with unit area and FWHM of 1mm was used to convolve the corrected monte carlo aperture function.

Aperture functions were generated using the monte carlo code and subsequent convolutions for the following detector configurations:

$30x15x4.5mm^3$ BGO Crystals, 350keV Threshold

	Inter-crystal Gap	Angle of Incident Gamma Ray
(1)	1mm air	0°
(2)	1mm tungsten	0°
(3)	1mm air	20°
(4)	1mm tungsten	20°

The graphs of the unconvolved aperture functions are presented in Figure 4.3(a) and the convolved functions in Figure 4.3(b). The data in Figure 4.3(a) are generated by the monte carlo program. The error bars

indicate the Poisson statistical error on the point as determined by the total number of gamma ray histories generated during the running of the program. The curve used to parameterize the data consisted of two exponential tails joined by a cubic spline. The cubic matched the tails to the first derivative at two spline points, S_{low} and S_{high}. The fitting function, in terms of the source position x, was:

$$f(x) = \begin{cases} A_{low} \cdot \exp\ (\ B_{low} \cdot x) & x \leq S_{low} \\ C_o + C_1 \cdot x + C_2 \cdot x^2 + C_3 \cdot x^3 & S_{low} \leq x \leq S_{high} \\ A_{high} \cdot \exp\ (B_{high} \cdot x) & x \geq S_{high} \end{cases} \qquad [4.3]$$

The two spline points were determined by a two dimensional chi-squared minimization of f(x). The exponential tails were calculated by a logarithmic-weight compensated linear least squares regression. The four cubic coefficients were determined by the other six parameters and the four boundary conditions at S_{low} and S_{high}. These parameters are listed in the figures of the aperture function graphs. The reduced chi-squared value of the fit (chi-squared/number of degrees of freedom), is printed at the top of each graph. An appropriate fit has a reduced chi-squared value whose order of magnitude is around 1. The total integral of the fitting function was used to normalize the count rate and the maximum of the fitting function was centred at x=0. The FWHM, FWTM, R and SNR calculated at .182mm^{-1} are also listed on each figure. The listed SNR assumes a value of 1000 gamma rays/mm for the incident gamma

ray linear intensity and does not account for the drop in efficiency introduced by the inclusion of septa. This parameterization proved useful because it matched the tails of the distribution very well, which was important for the normalization, and calculations of R and SNR. Moreover, the chi-shared confidence confidence levels of the fits indicated that equation 4.3 is not an inappropriate description of the monte carlo generated aperture functions. The confidence levels of the four fits ranged from .5% to 4.5% with an average of (2.5±1.8)%. (The chi-squared confidence level is the probability that a fit that appropriately describes the data has a chi-squared value greater than the measured value.) A non-symmetric gaussian parameterization was also tested but, because it failed to accurately fit the tails (and therefore had an unacceptably large chi-squared value), it was not used.

Table 4.1 summarizes the results of the monte carlo calculations. According to the simulation, the addition of septa should insignificantly effect the aperture function FWHM and spectral resolution, R for gamma rays incident at 0°. A small, approximately 10%, increase in the FWTM is predicted. For gamma rays incident at 20°, the FWHM and FWTM both improve by only 8% and the spectral resolution improves by around 10%. The SNR at .182mm^{-1} shows no improvement for the 0° rays when septa are used, but it increases by nearly 4dB for the 20° rays when the difference in efficiency is not accounted for. If the efficiency is assumed to be equal to the square of the packing fraction, then a correction to SNR for this drop in efficiency can be made. The corrected SNR still increases by almost 2dB for the 20° gammas when septa are used. However, after making

FIGURE 4.3 MONTE CARLO SIMULATED APERTURE FUNCTIONS

The simulated data from L.R. Lupton's running of the APERT program, for the detector parameters used in the measurements, are presented as data points in Figure 4.3(a). The error bars on each data point represent the statistical error. The curve drawn on each graph is the least squares fitted function described by equation 4.3. The coincidence count rate was normalized by the integral of the fitting function to produce a 'Normalized Coincidence Response'. The position of the peaks are shifted to the zero position. The reduced chi-squared, FWHM, FWTM, Spectral Resolution (R as defined in equation 4.1) and the Spectral Signal-to-Noise Ratio evaluated at .182mm^{-1} (SNR as defined in equation 4.2) are presented with the raw fitted functions in Figure 4.3(a,1-4). The fitted function was convolved with a square function, to include the effects of finite source dimensions, and a gaussian, to account for the non-colinearity effects. The raw fitted functions, convolved functions, and the FWHM, FWTM, R, and SNR of the convolved fuctions are presented in Figure 4.3(b,1-4).

FIGURE 4.3 (a 1)

GRAPH OF MONTE CARLO GENERATED

APERTURE FUNCTION FOR 0° RAYS AND

DETECTORS WITHOUT TUNGSTEN

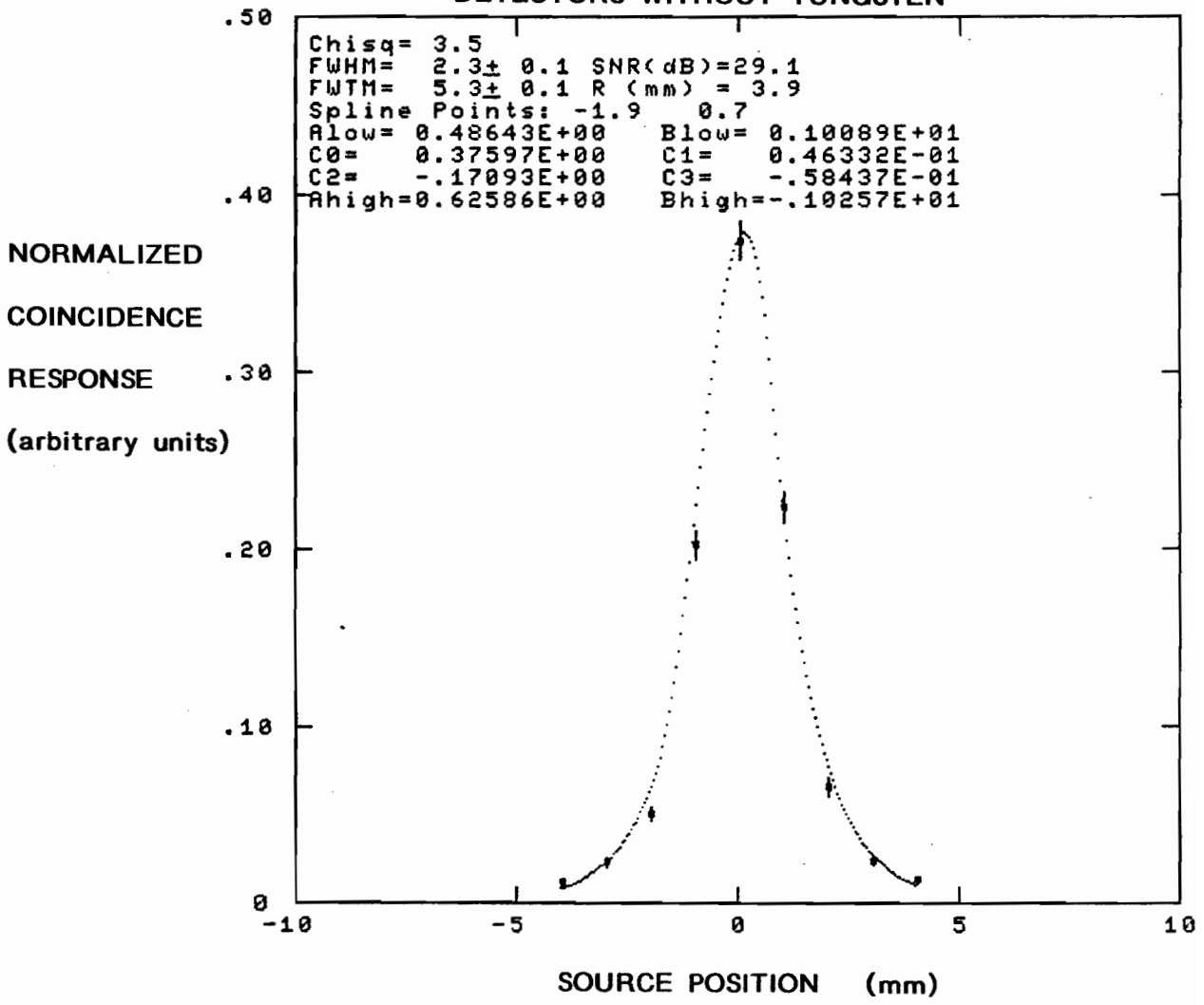

FIGURE 4.3(a 2)

GRAPH OF MONTE CARLO GENERATED APERTURE FUNCTION FOR 20° RAYS AND DETECTORS WITHOUT TUNGSTEN

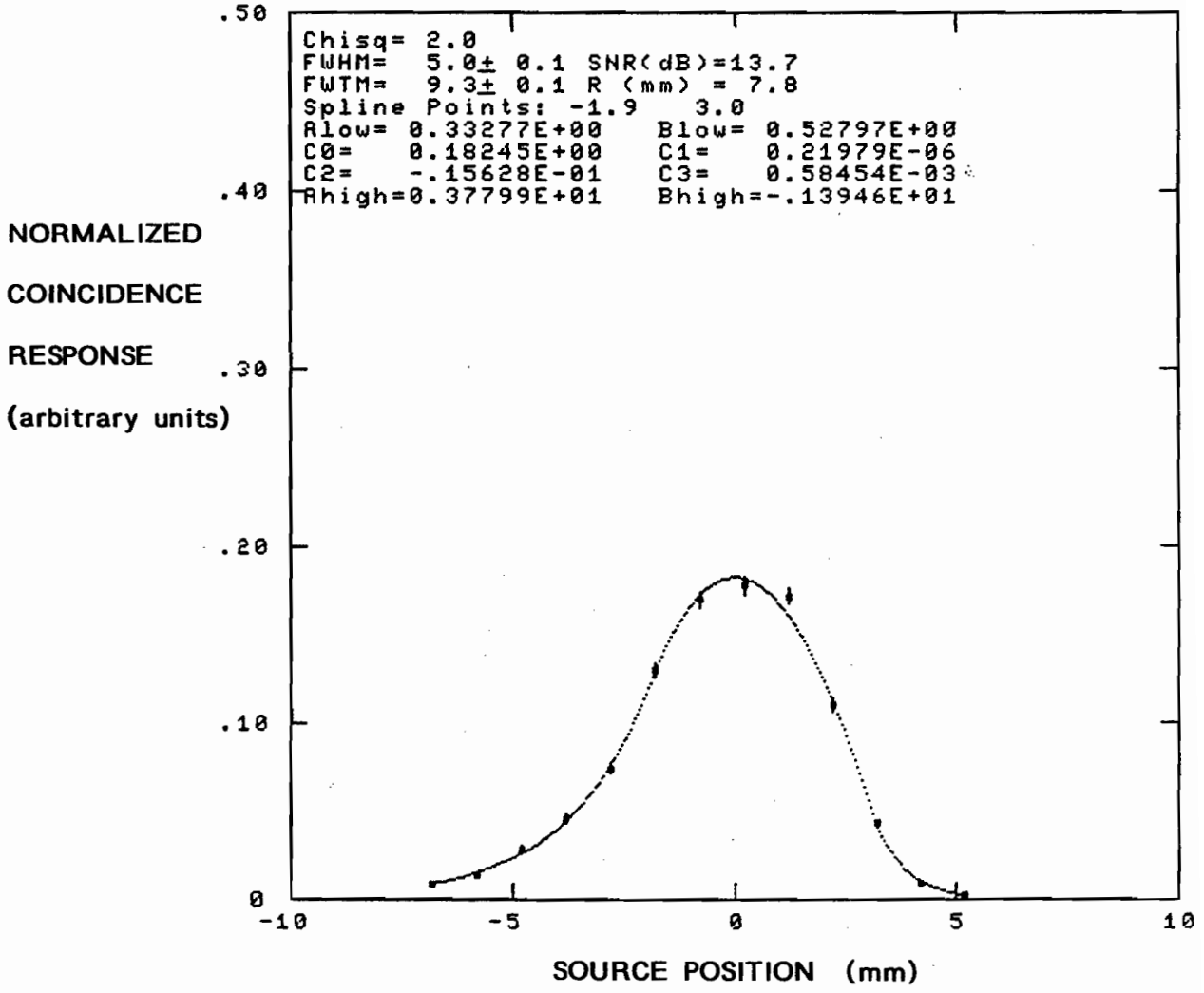

FIGURE 4.3(a 3)

GRAPH OF MONTE CARLO GENERATED APERTURE FUNCTION FOR 0° RAYS AND DETECTORS WITH TUNGSTEN

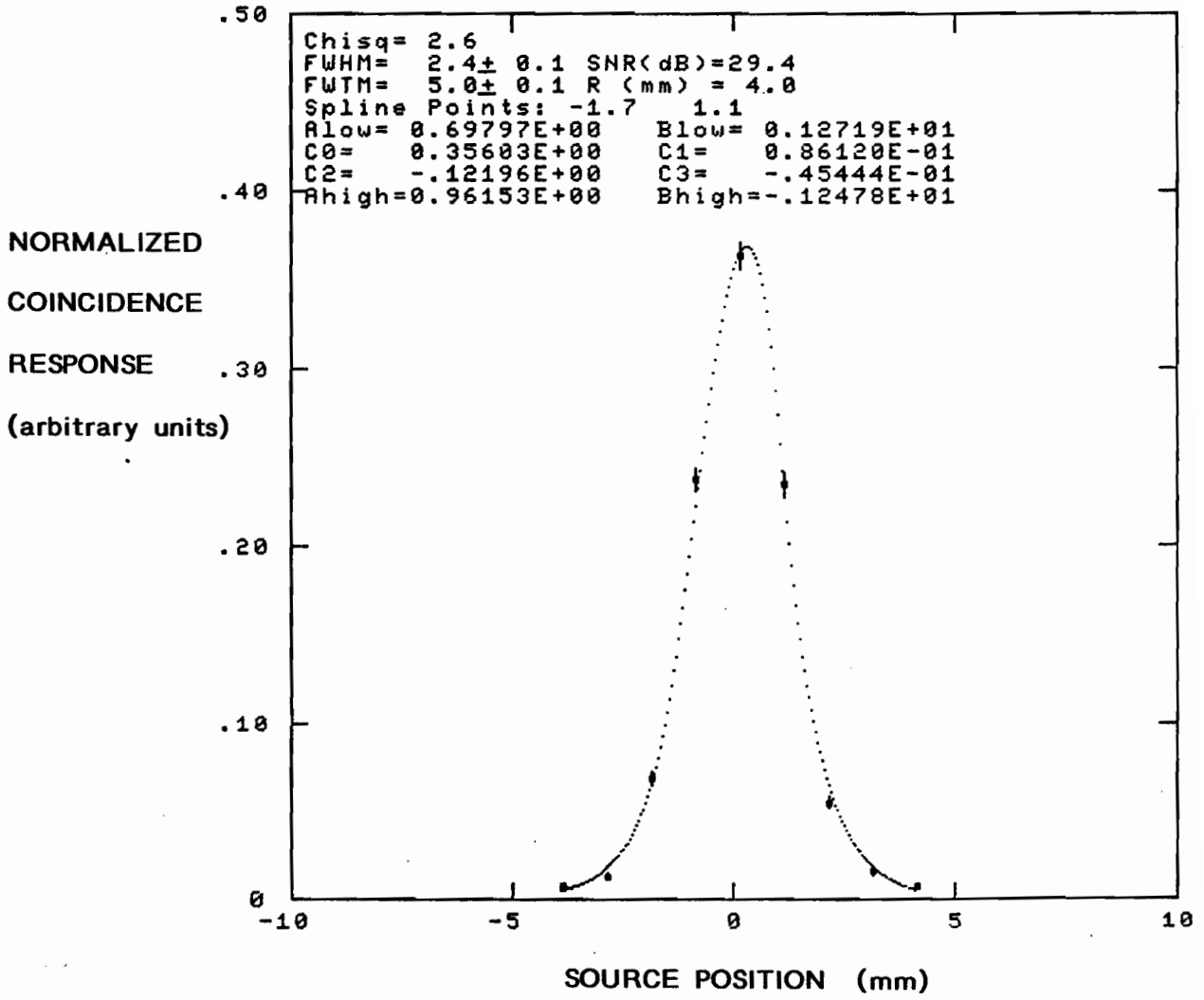

FIGURE 4.3 (a 4)

GRAPH OF MONTE CARLO GENERATED APERTURE FUNCTION FOR 20° RAYS AND DETECTORS WITH TUNGSTEN

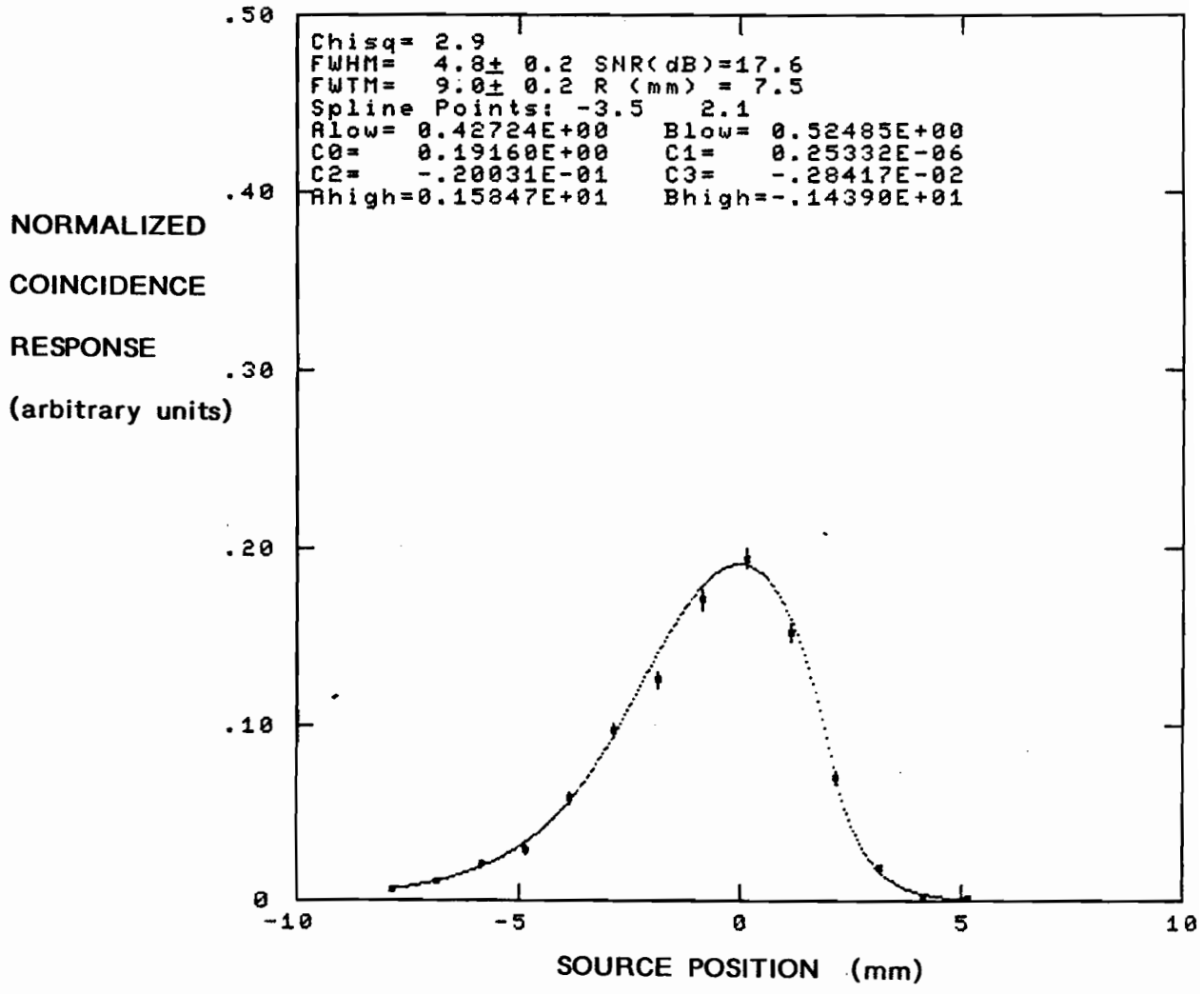

FIGURE 4.3(b 1)

GRAPH OF SIMULATED APERTURE FUNCTION CONVOLVED WITH NON-COLINEARITY AND FINITE SOURCE FUNCTIONS FOR 0° RAYS AND DETECTORS WITHOUT TUNGSTEN

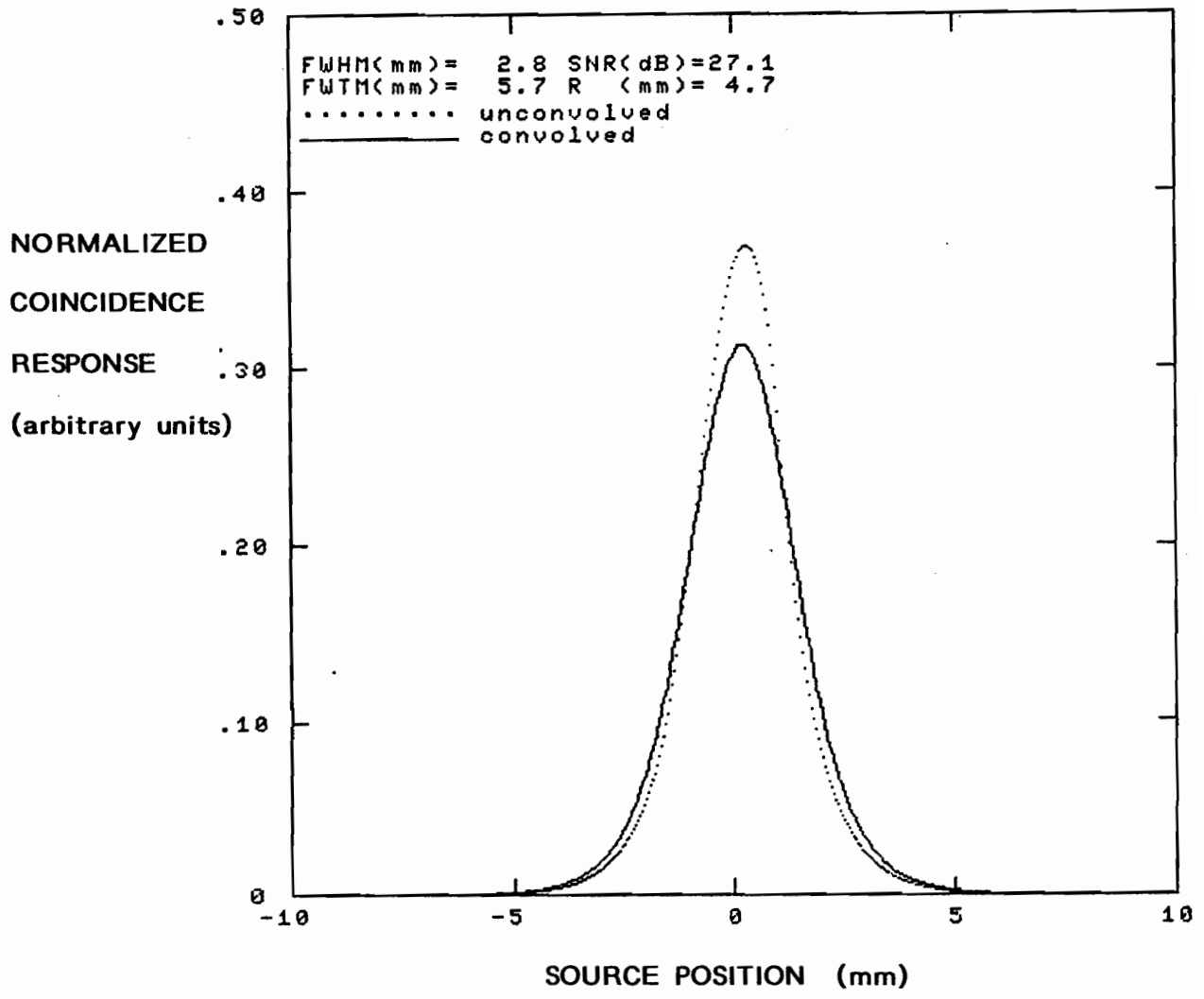

FIGURE 4.3(b 2)

GRAPH OF SIMULATED APERTURE FUNCTION CONVOLVED WITH NON-COLINEARITY AND FINITE SOURCE FUNCTIONS FOR 20° RAYS AND DETECTORS WITHOUT TUNGSTEN

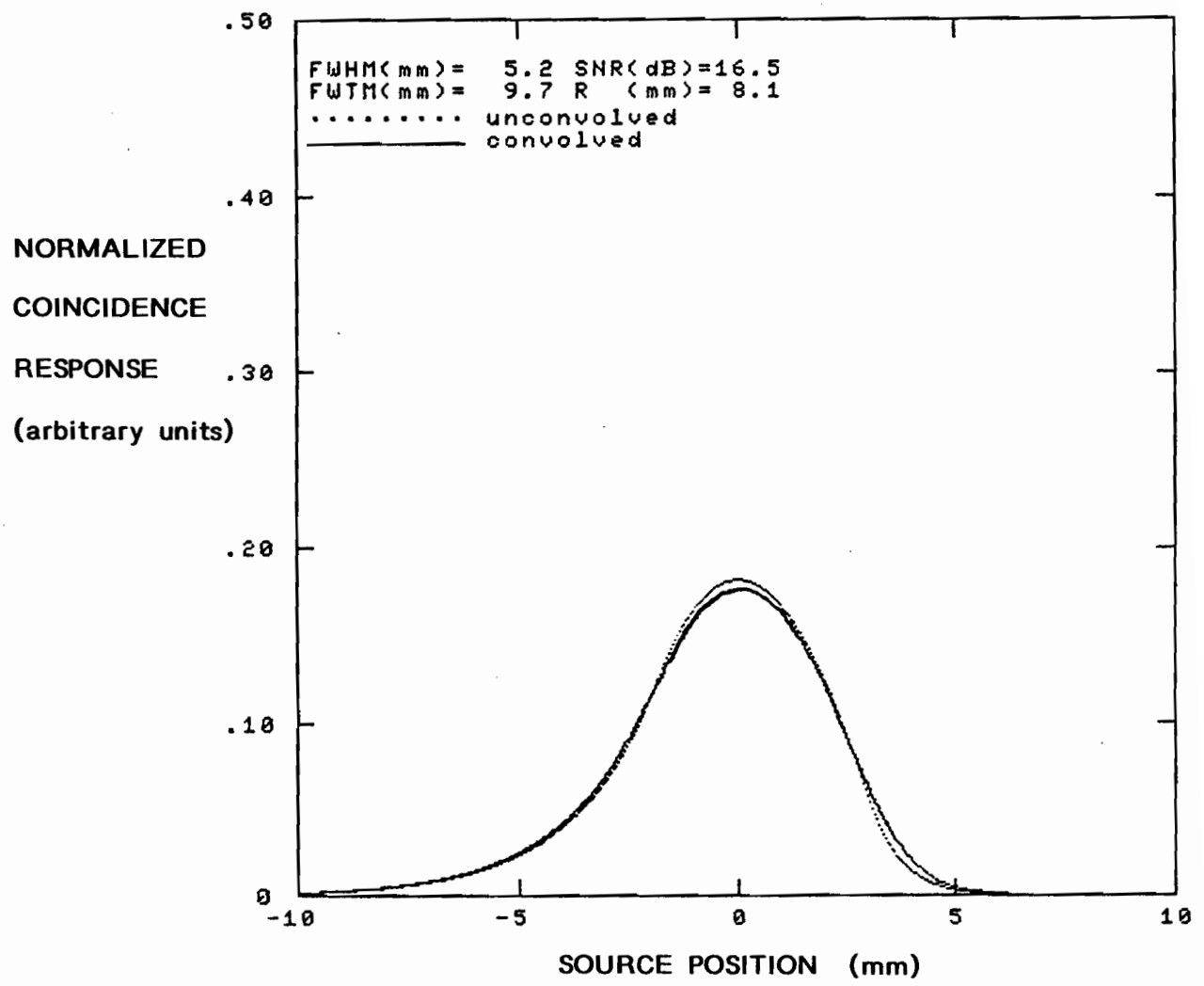

FIGURE 4.3(b 3)

GRAPH OF SIMULATED APERTURE FUNCTION CONVOLVED WITH NON-COLINEARITY AND FINITE SOURCE FUNCTIONS FOR 0° RAYS AND DETECTORS WITH TUNGSTEN

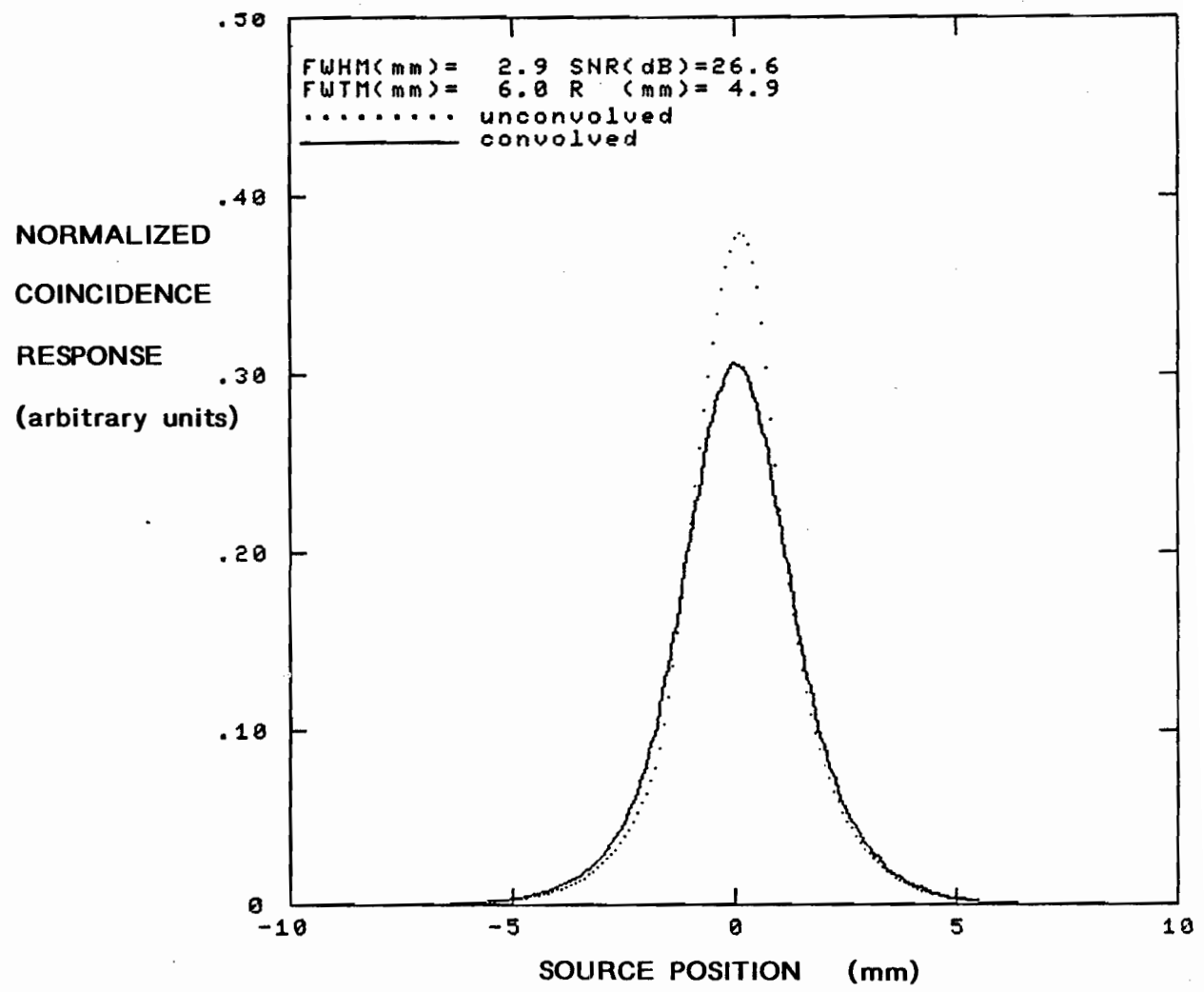

FIGURE 4.3(b 4)

GRAPH OF SIMULATED APERTURE FUNCTIONS CONVOLVED WITH NON-COLINEARITY AND FINITE SOURCE FUNCTIONS FOR 20° RAYS AND DETECTORS WITH TUNGSTEN

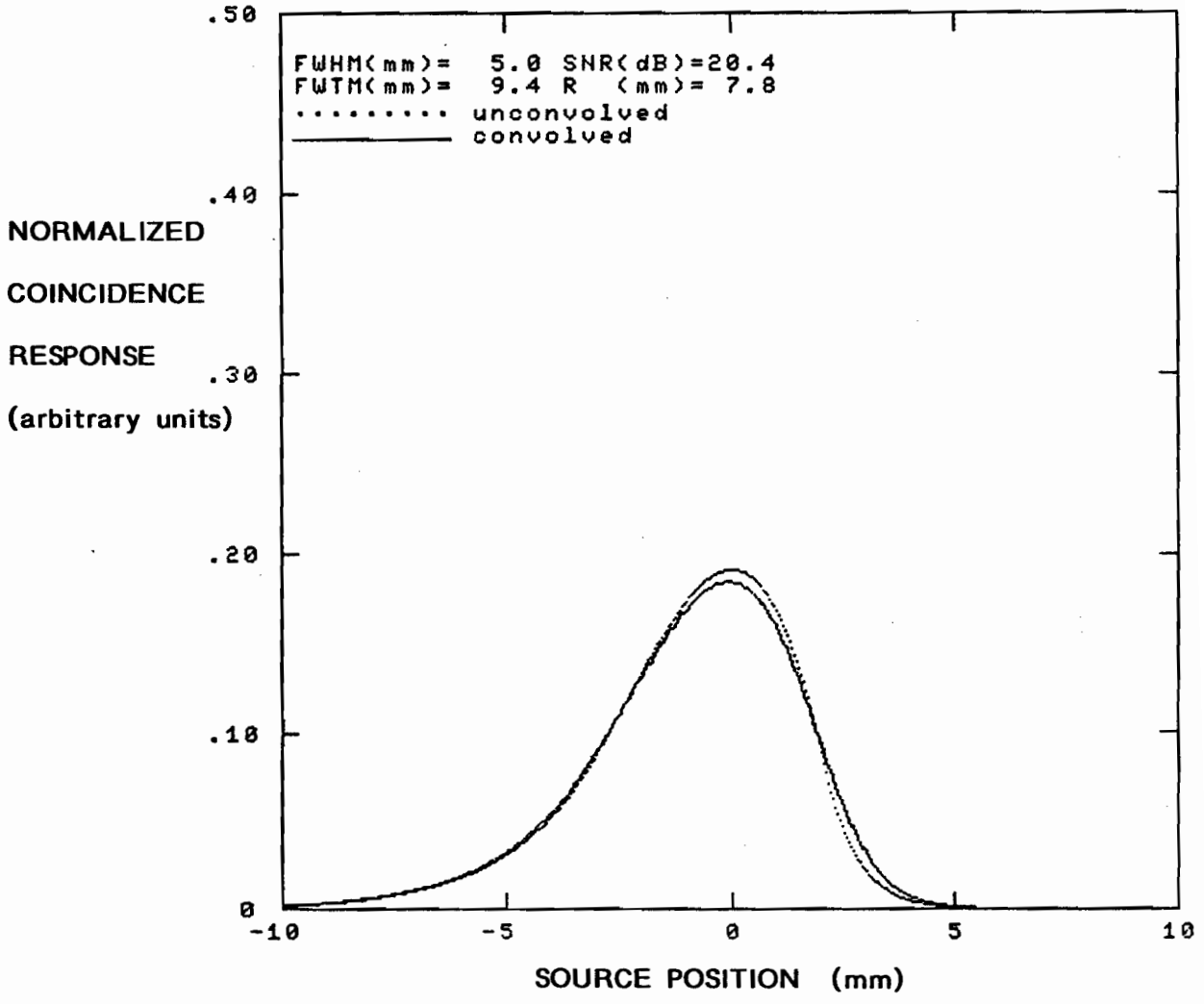

TABLE 4.1 SUMMARY OF MONTE CARLO APERTURE FUNCTION SIMULATIONS

		Without Tungsten Septa	With 1mm Tungsten Septa
0° rays	FWHM (mm)	2.8	2.9
	FWTM (mm)	5.7	6.0
	R (mm)	4.7	4.9
	SNR (dB)	27.1	26.6
20° rays	FWHM (mm)	5.2	5.0
	FWTM (mm)	9.7	9.4
	R (mm)	8.1	7.8
	SNR (dB)	16.5	20.4

this correction for the 0° rays, the SNR is expected to be almost 2dB lower when tungsten is used. Although there is a 2dB improvement at .182mm^{-1} for angled rays, at half this frequency the SNR values uncorrected for efficiency differences, are the same. Therefore, at lower frequencies, one expects the corrected SNR to be degraded when tungsten in inserted because of the efficiency losses.

4.3 Experimental Setup

The experimental setup for the aperture function measurements is depicted in Figure 4.4. Two quad BGO detectors were placed on 12cm high styrofoam blocks to limit the effect of gamma rays scattering from the bench surface. A 5mm thick lead plate extending from the bottom of each detector, as shown in Figure 4.4(b), was inserted to absorb any gamma ray scattering from the bench. The detector pair viewed a 10mm thick slice which was defined by 15x40x40mm^3 tungsten collimators visible in Figure 4.4(b). Short collimators were used because the monte carlo simulation does not account for the scattering effects of collimators. Since the effects are more significant for longer collimators, there is presumably less discrepancy between the monte carlo simulation and an experiment using short collimators. Two 4.5mm wide BGO crystals (with septa, if consistent with the detector configuration being tested) were placed on either side of the quad detector crystals when the 0° gamma ray experiments were conducted. When the 20° ray measurements were made, an additional 10mm of BGO was added to the side of the detector corresponding to the periphery-side of the tomograph. These extra crystals simulated the adjacent crystals in a tomograph array, and

FIGURE 4.4 PHOTOGRAPH OF EXPERIMENTAL SETUP

(a) The two detectors were placed on styrofoam blocks to minimize the effects of scatter from the bench surface. The source was fastened to the microdrive unit and placed between the two quad detectors, as shown. The electronics rack holds the high voltage supply, TN-7200 MCA, and the NIM modules (the nsec delay, TAC, Detector Decoder and delay amplifier modules can be seen).

(b) The two preamplifiers for the two PMT sectors are contained in the box behind the detector. The tungsten slice-width defining collimator is in front of the detector. The auxiliary BGO crystals, wrapped in white paper and placed next to the quad detector crystals, were used to introduce the scattering effects that exist in a detector ring.

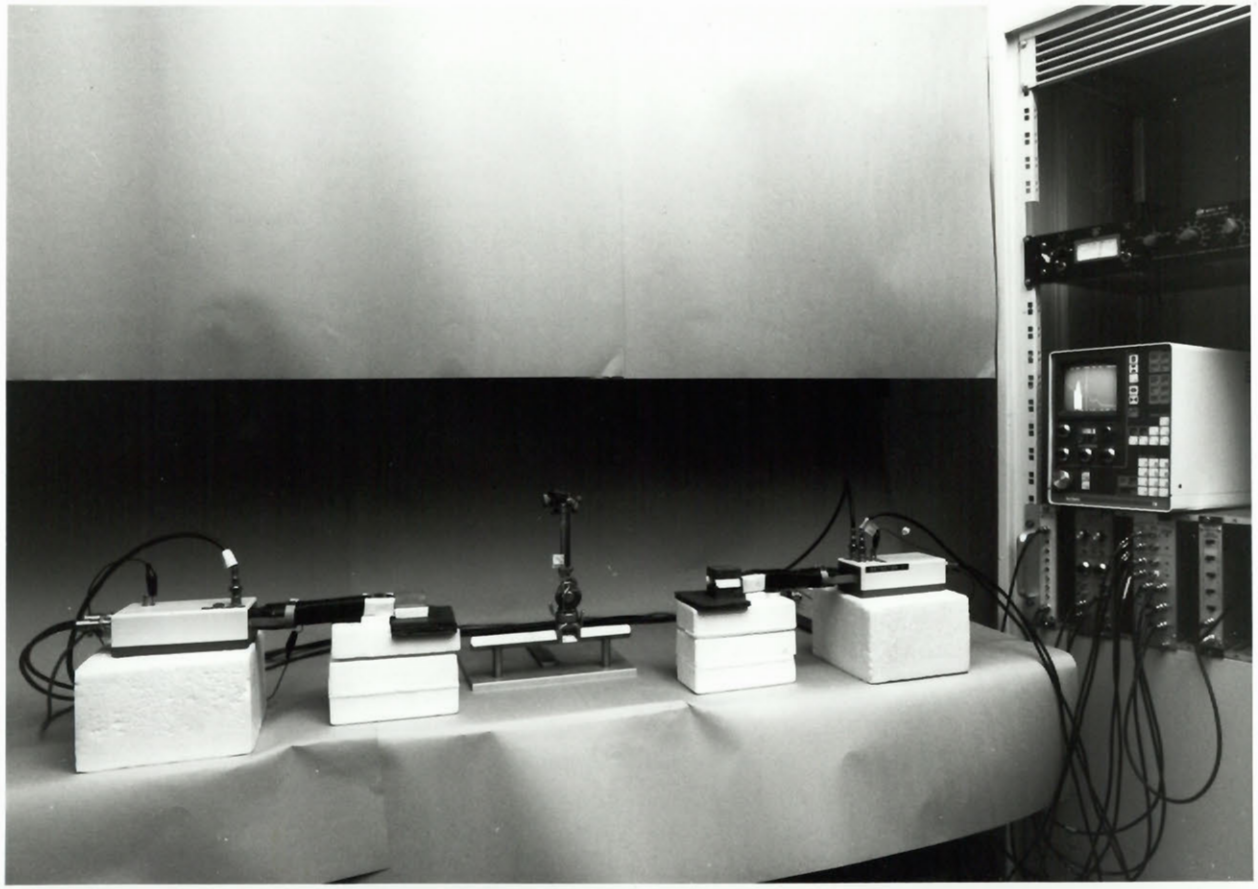

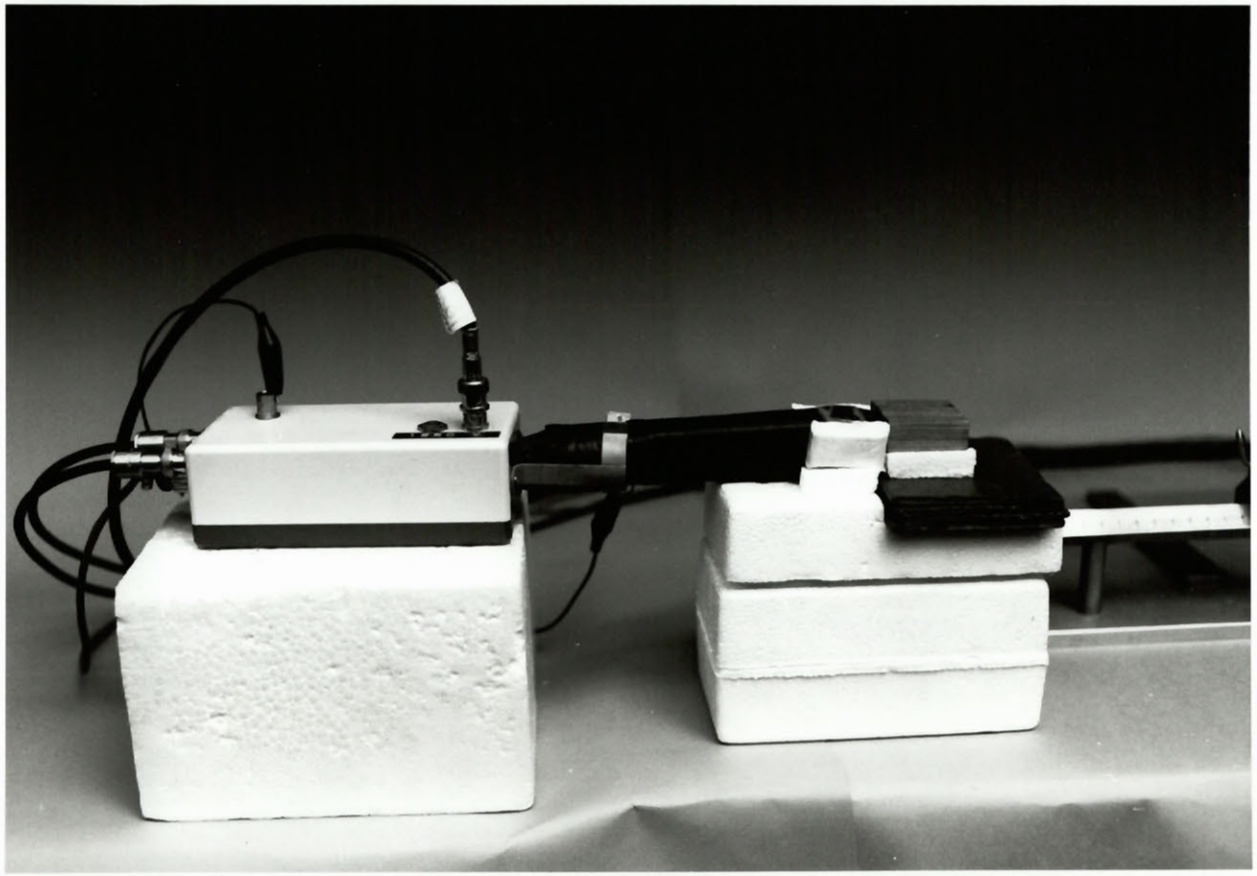

thereby introduced the shielding and scattering effects that would be present in an actual tomograph. The detectors were placed 460mm apart for the 0° measurements. For the 20° ray experiments, the two detectors were oriented at an angle of 40° with respect to each other and placed 430mm apart. As mentioned in the Section 4.1, four crystal-septa configurations were tested using the geometrical setup described above.

The high voltage on both detectors was set at approximately +1150V. The gain of each PMT sector was adjusted, using potentiometers at the seventh dynodes, to ensure that the peaks from all eight crystals overlapped. The anode of each sector was input to a preamp as described in Section 2.5 (two preamps were contained in the grey box in Figure 4.4(b)) and the preamp outputs were fed to the Detector Decoder module. An energy window was set up between 350 and 650keV. The 350keV level was used to imitate a practical PET system and the 650keV level was used to veto events related to the higher energy gamma rays which were emitted by the ^{56}Co source that was used. The timing threshold was set at 20keV and the cross talk threshold, used for crystal identification, was set at 40keV. The coincidence circuit used was described in Section 2.6. The TAC SCA was used to establish a 17ns wide coincidence window. The Detector Decoder analogue detector identification pulse was sent to a TN7200 MCA which counted the number of coincidence counts of the sixteen detector pairs for a predetermined period of time (usually fifteen minutes), before outputting the total number of counts.

Because it was expected that the measurements would be taken over a period of weeks, and because it was necessary to use the same source in order to obtain a rough measure of the relative coincidence efficiencies of the various configurations, a source with a half life longer than a month was required. In addition, it was necessary to have a thin line source with an activity high enough to provide adequate statistics over a fifteen minute period. For these reasons, a ^{56}Co source, which has a half life of 78.8 days, was produced. The edge of a .25mm thick 99.7% pure iron foil was bombarded for four hours with 12MeV protons at the McGill Synchrocyclotron. The ^{56}Co was produced through the $^{56}Fe(p,n)^{56}Co$ reaction, whose excitation function peaks at 12MeV.[Keller et al, 1973] The foil was moved in 2mm steps during bombardment to ensure that the source would be distributed uniformly over a 10mm distance along the edge. A .6mm wide strip was cut from the edge of the foil and encapsulated in a glass capillary tube with a .8mm ID and 1.2mm OD. With the source encapsulated in the glass tube, approximately 50% of the positrons emerging from the iron strip would annihilate in the glass. This is based on a calculation using equation A2.1, the value $2.32 g/cm^3$ for the density of SiO_2 and 1.46MeV for the ^{56}Co endpoint energy. ^{56}Co decays by beta plus (19%) and electron capture (2%) to the 2.085MeV second excited state of ^{56}Fe. This state decays to the .847MeV first excited state which subsequently decays to the ground state. This cascade produces two high intensity lines at 847 and 1238keV in the gamma ray spectrum. In addition to the above decay, ^{56}Co decays by electron capture to a number of excited states of ^{56}Fe whose decays produce the

^{56}Co ($t_{1/2}$ = 78.8 d)

Energy(keV)	Relative Intensity
263.41 10	22 4
411.38 8	25 3
486.54 11	55 5
733.72 15	200 10
787.88 7	310 10
846.772 13	100000
896.56 20	70 5
977.485 60	1440 15
997.33 16	112 6
1037.840 15	14000 100
1089.03 24	50 10
1140.28 10	150 10
1160.08 16	100 10
1175.102 16	2280 20
1198.78 20	50 10
1238.282 17	67600 700
1272.2 6	20 2
1335.56 8	125 5
1360.25 7	4330 40
1442.75 8	200 10
1462.34 12	77 5
1640.54 13	60 10
1771.351 26	15700 150
1810.4 5	640 10
1963.99 6	720 15
2015.181 28	3080 30
2034.755 29	7890 70
2113.85 15	385 5
2213.16 15	350 10
2276.36 16	110 5
2373.71 40	80 10
2523.86 20	60 5
2598.458 33	16900 150
3009.591 42	1000 10
3201.962 46	3040 30
3253.416 45	7410 65
3272.990 45	1750 20
3369.69 30	11 2
3451.152 47	875 10
3547.925 61	180 5
3600.69 40	16 1
3611.69 40	7 1

TABLE 4.2 ^{56}Co GAMMA RAY ENERGIES AND RELATIVE INTENSITIES from Lederer et al, 1978

spectrum presented in Table 4.2. There are a few low intensity lines which fall in the 350-650keV window of the Detector Decoder SCAs, but one expects more events associated with the 847 and 1238keV gamma ray Compton interactions in the crystal falling in the window than these. To account for the non-annihilation gamma rays, background measurements were taken by orienting the two detectors at 90° to each other and counting coincidences with the source 230mm directly in front of both detectors. With the coincidence window width set at 17ns, the count rate was an insignificant fraction of the statistical error of the aperture function measurements' count rates. It was concluded that the gamma rays emitted from the ^{56}Co are effectively eliminated from the experiment using the 17ns timing window and, therefore, no background subtraction was required.

The data were corrected for ^{56}Co decay by normalizing the count rates of all of the experiments to the same initial time. In this way, a rough measure of the relative efficiencies of the various configurations could be made. Care was taken to ensure that the only detector-source positions and orientations that were different were those introduced to study the 0° and 20° angle aperture functions.

The source was fastened to a vernier microdrive unit (David Kopf Instr.) visible in Figure 4.4(a). It was moved in (1.00$\pm$.05)mm steps over a range that included at least the points in the aperture function at fifteenth maximum for all sixteen detector pairs. Although the data were collected in the extreme tails, in order to introduce uniformity

TABLE 4.3 DETECTOR PAIR IDENTIFICATION CODES

DETECTOR ONE CRYSTAL NUMBER	1	1	2	2	1	1	2	2	3	3	4	4	3	3	4	4
DETECTOR TWO CRYSTAL NUMBER	4	3	4	3	2	1	2	1	4	3	4	3	2	1	2	1
DETECTOR PAIR ID CODE	0	1	2	3	4	5	6	7	8	9	10	11	12	13	14	15

DETECTOR ONE

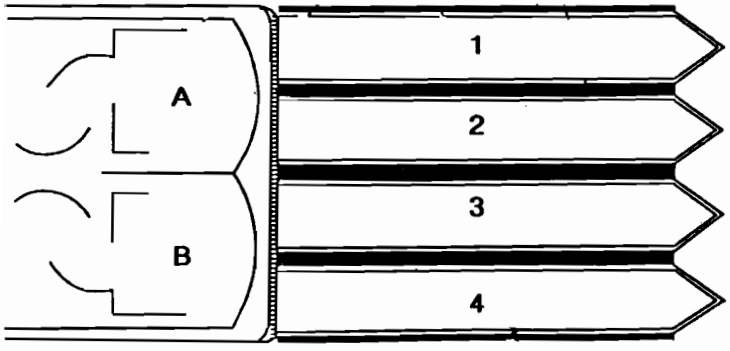

DETECTOR TWO

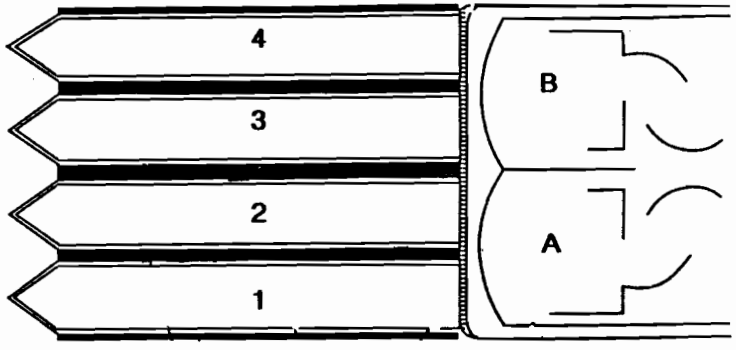

in the tail data of the various sets, only data with a relative statistical errors of less than 50% were included in the analysis.

Each of the sixteen detector pairs had been given an identification code between 0 and 15. These are summarized in Table 4.3 and are used in the presentation of the data.

4.4 Results

The decay-corrected aperture functions were fitted by the function described by equation 4.3. The count rates were normalized with respect to the total integral of the fitting function, and the peak of the function was shifted to x=0. Each configuration has sixteen measured aperture functions associated with it. The integral (Int.),reduced chi-squared of the fit (Chisqrd), and the detector pair code described by Table 4.3 (Code) are printed at the top of each graph. The FWHM, FWTM, R and SNR (at $.182 mm^{-1}$) are all calculated from the fitting function and are also printed at the top of each graph. The shielding crystals all had flat faces. Because of this, not all detector pairs of the tapered crystal configurations for the 20° rays can be used. In particular, data involving Detector 1: crystal 1 or Detector 2: crystal 4 (see Table 4.3) does not provide information about the usefulness of pointed crystals. Therefore, calculations of the FWHM, FWTM, R and SNR do not make use of such detector pairs data.

The normalized aperture functions, determined by the 0° incident angle central source and 20° incident angle peripheral source

measurements, are presented in Figure 4.5 (a)-(h). To facilitate comparisons between detector pair aperture functions, the sixteen graphs associated with each detector pair of a particular configuration are presented on two pages. To avoid clutter, the axes of the graphs have not been labelled. The source position in millimetres is represented by the horizontal axis, while the normalized coincidence response in normalized units is represented on the vertical axis. A 'key' summarizing the information in these last two paragraphs is presented before the data.

It should be noted that some data are not well represented by the fitting function. The poor fits are revealed by the high reduced chi-squared values. The chi-squared value can be obtained by multiplying the reduced chi-squared value by the number of data points in the graph less six. If the confidence level of the chi-squared is below .1%, then the fit is not acceptable. Data having fits below the .1% confidence level are not considered in further analysis. The fitting function was adequate for the monte carlo generated data and over 80% of the measured functions, but data not appropriately fit by the function will not provide meaningful measures of FWHM, FWTM, R, and SNR since these parameters were determined from the fitted function.

The average values of the SNR, FWHM, FWTM, R, and Int. are presented in Table 4.4. The mean reduced chi-squared value of all of the data sets, including those sets with a fit below the .1% confidence level, was 2.5 with a standard deviation of 2.9. As noted above, the SNR

does not take into consideration the difference in efficiencies of the various configurations. But this can be accounted for by using the values of the total integrals, which are proportional to the total coincidence count rate of the detector pair.

As mentioned in the introduction to this chapter, measurements of the aperture functions related to 0° gamma rays emitted from a source 78mm off centre were also made. No significant differences between these functions and those of a central 0° source were observed.

4.5 Discussion of Calculations and Measurements

The results in Table 4.4 indicate that the errors of the resolution measurements of the different detectors are approximately .5mm FWHM. Within this standard deviation, the FWHM measurements of the flat crystals are in agreement with the monte carlo simulations. The FWTM and R measurements are approximately (25±10%) higher than the simulated results, for the configurations both with and without tungsten. The longer tails in the measured aperture function have the effect of reducing the SNR at $.182mm^{-1}$ (uncorrected for efficiency) by (2.8±1.6)dB for the 0° rays and (9.6±2.3)dB for the 20° rays.

The monte carlo simulation predicted little or no improvement in the FWHM, FWTM and R for both the 0° and 20° rays when tungsten is used. This was confirmed by the experiments. The SNR was predicted to be the same for the 0° rays and 4dB higher for the 20° rays when tungsten was used. Although the 0° ray prediction was confirmed to within 1.7dB, the

SNR data on the 20° rays lack the precision to either confirm or reject the predicted SNR improvement. The SNR improvement could range between -1.7dB and 8.3dB. The measured quantity, INT, does not have sufficienct precision to be used as a means of accurately evaluating efficiency. Instead, if the packing fraction is used to introduce the efficiency correction, the measured SNR at .182mm^{-1} corrected for efficiency, for the 0° and 20° rays are (-.1$\pm$1.7)dB and (1$\pm$5)dB respectively. These are consistant with the simulated results, but the large error margins limit the usefulness of the measurements. The same trends between configurations with tungsten and those without were observed in the tapered crystal data. That is, no significant improvements in FWHM, FWTM and R were observed. Also from these measurements, it is apparent that the use of receded septa plays no significant role in determining the resolution of narrow crystals.

Examination of differences between the parameters describing the detectors using tapered crystals and those using flat crystals reveals that no improvement in FWHM, FWTM or R can be expected when tapered crystals are used with narrow detectors.

FIGURE 4.5 APERTURE FUNCTION MEASUREMENTS

Sixteen detector pairs record coincidences when two quad detectors view a source. The aperture functions of all sixteen pairs are presented for the following configurations:

Incident Angle of Gamma Ray	Septum	Figure Label	
		Flat Face	Tapered Face
0°	air	(a)	(e)
20°	air	(b)	(f)
0°	tungsten	(c)	(g)
20°	tungsten	(d)	(h)

To prevent clutter, the axes of the graphs have not been labelled. Instead, a 'KEY' that explains all of the pertinent information of the data presentation is provided on the following page.

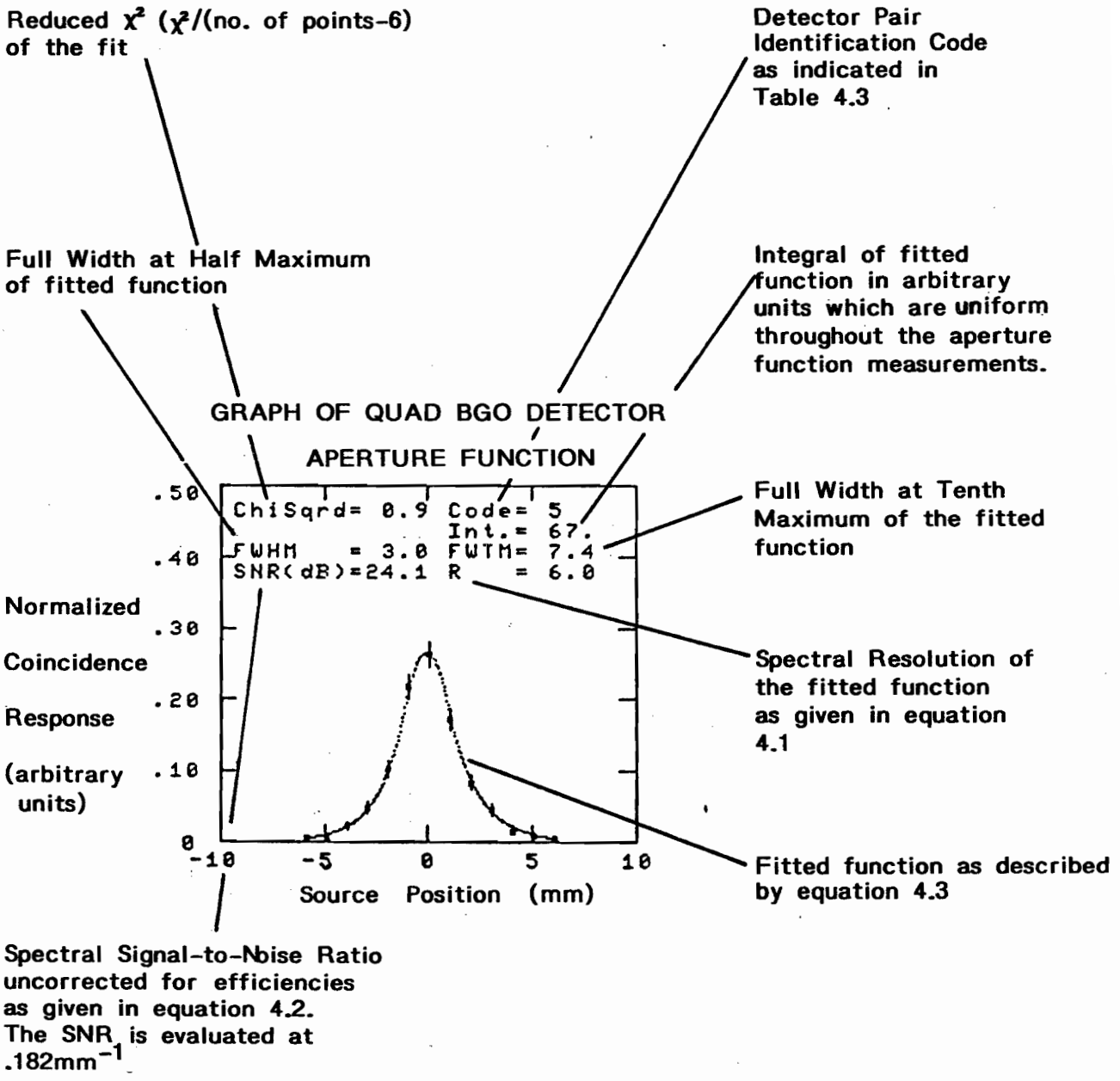

KEY TO APERTURE FUNCTION

DATA PRESENTATION

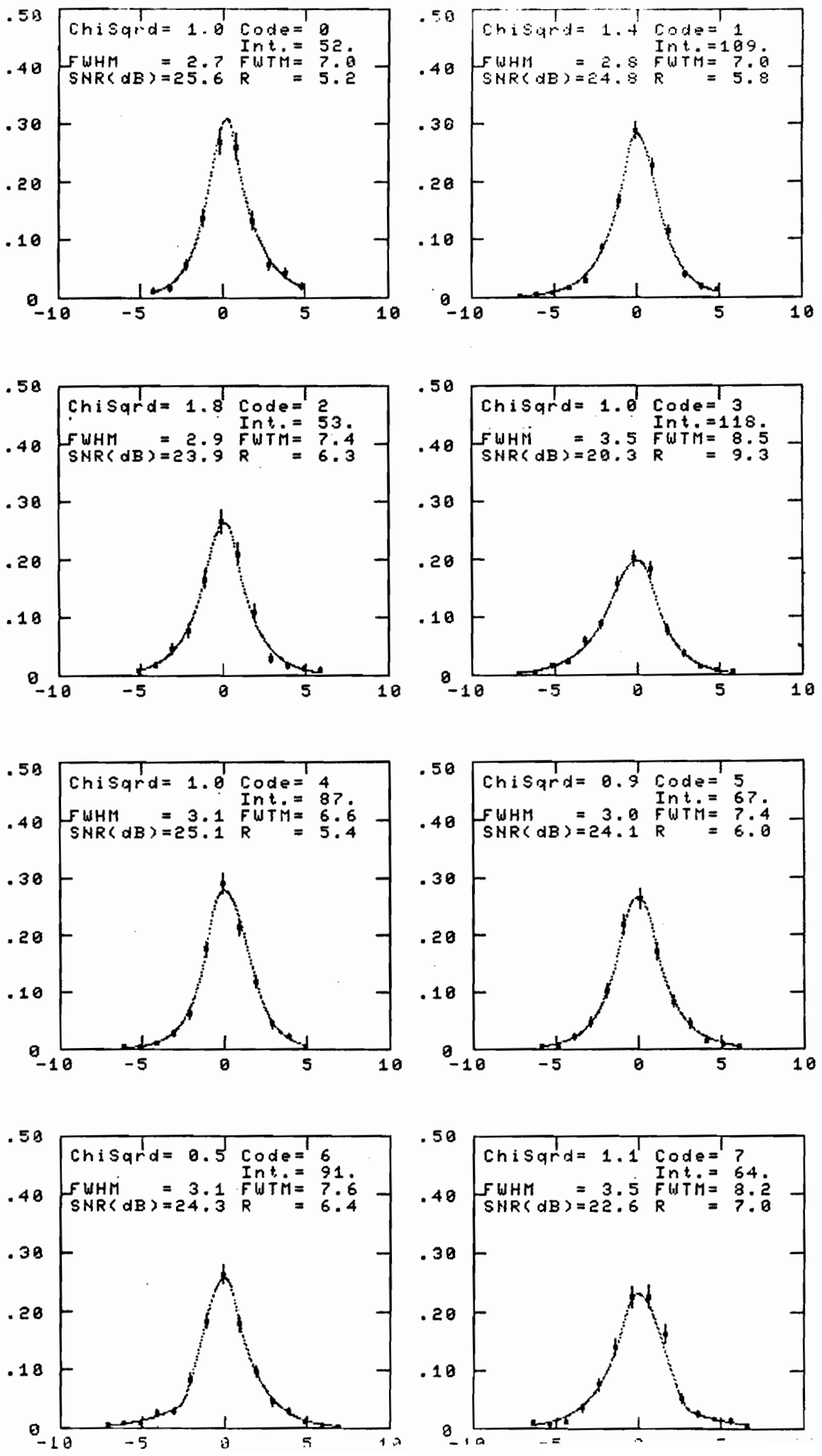

FIGURE 4.5(a) Flat crystals, without tungsten, 0° ray

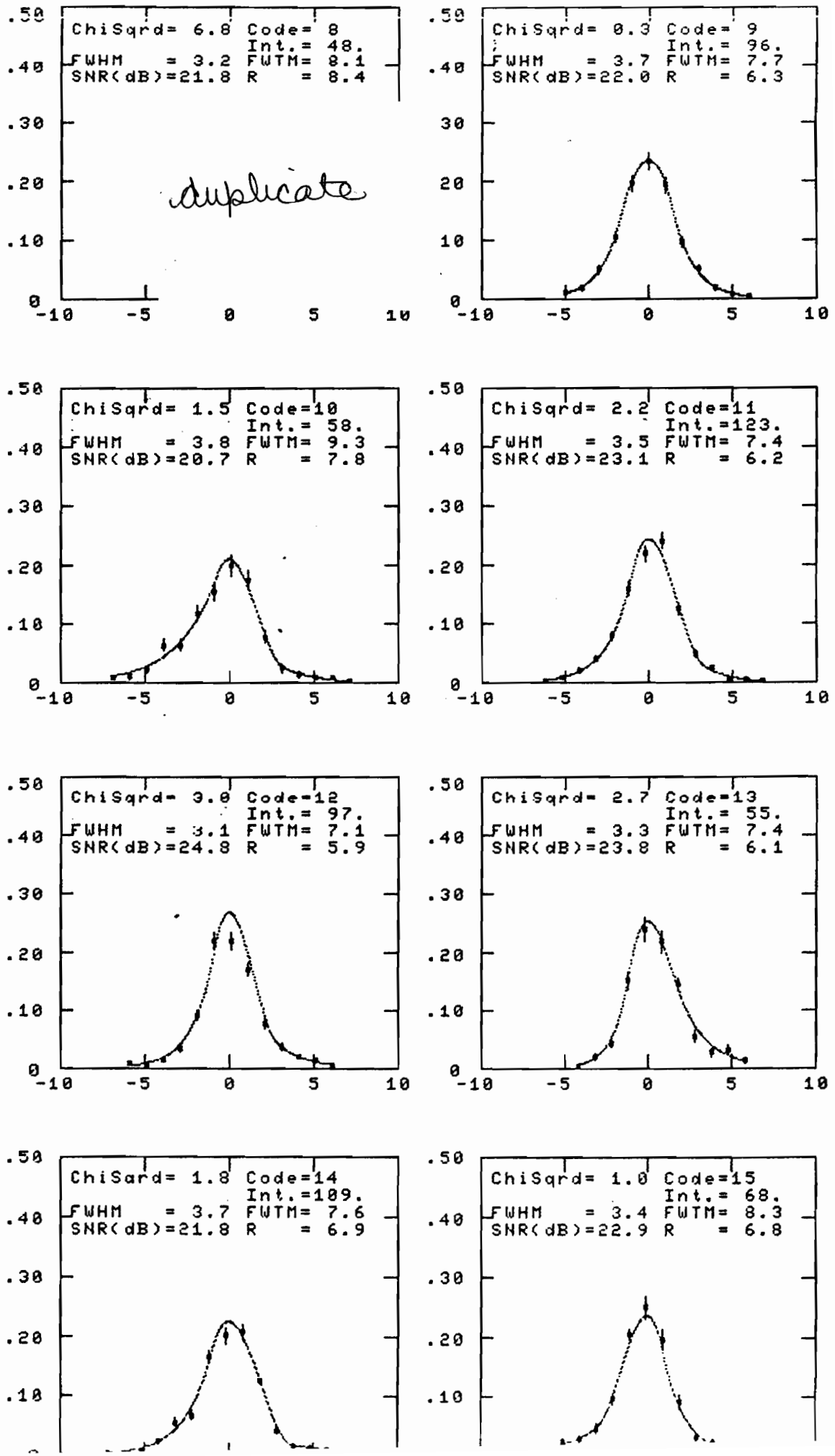

FIGURE 4.5(a) Flat crystals, without tungsten, 0° ray

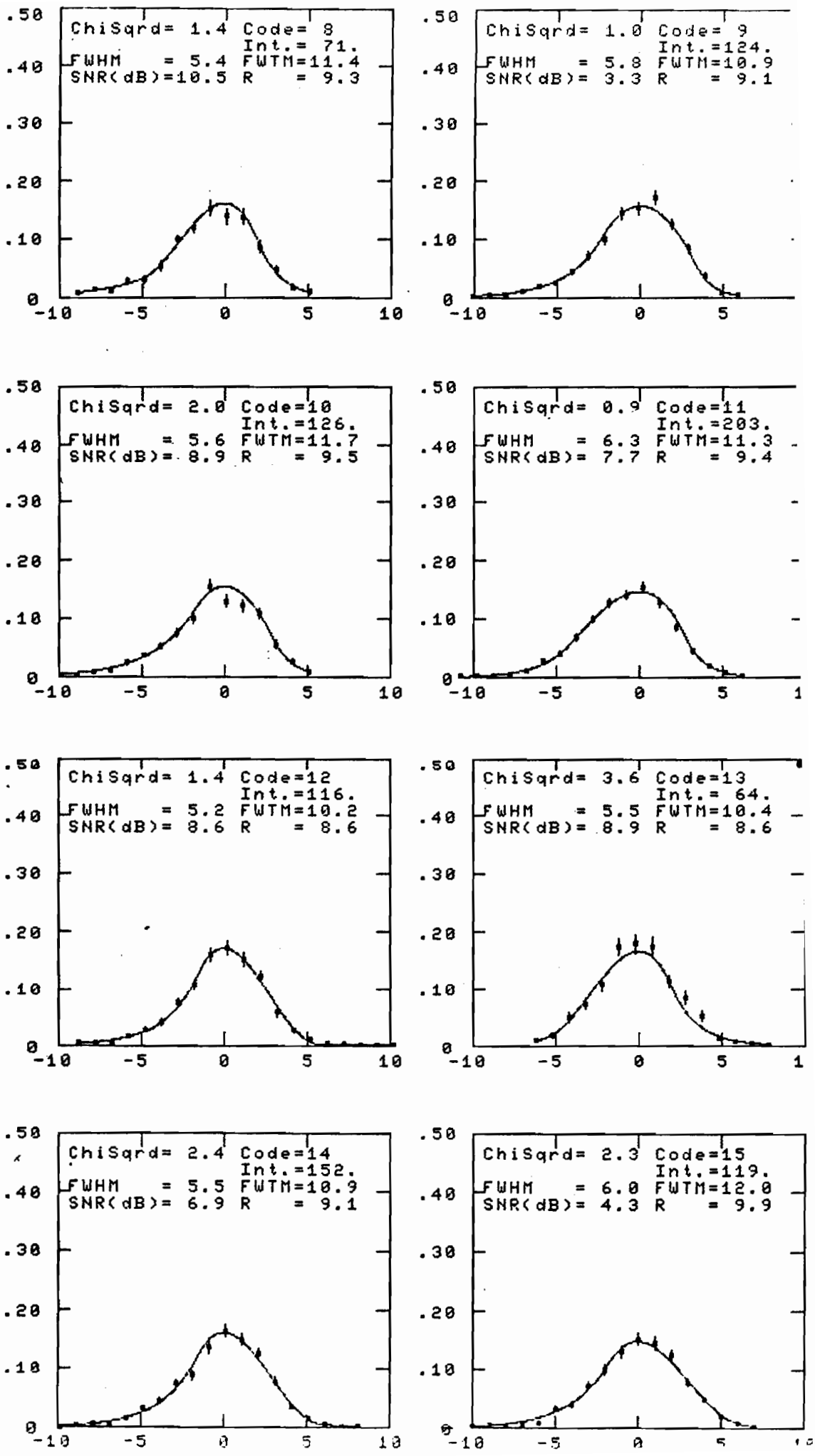

FIGURE 4.5(b) Flat crystals, without tungsten, 20° ray

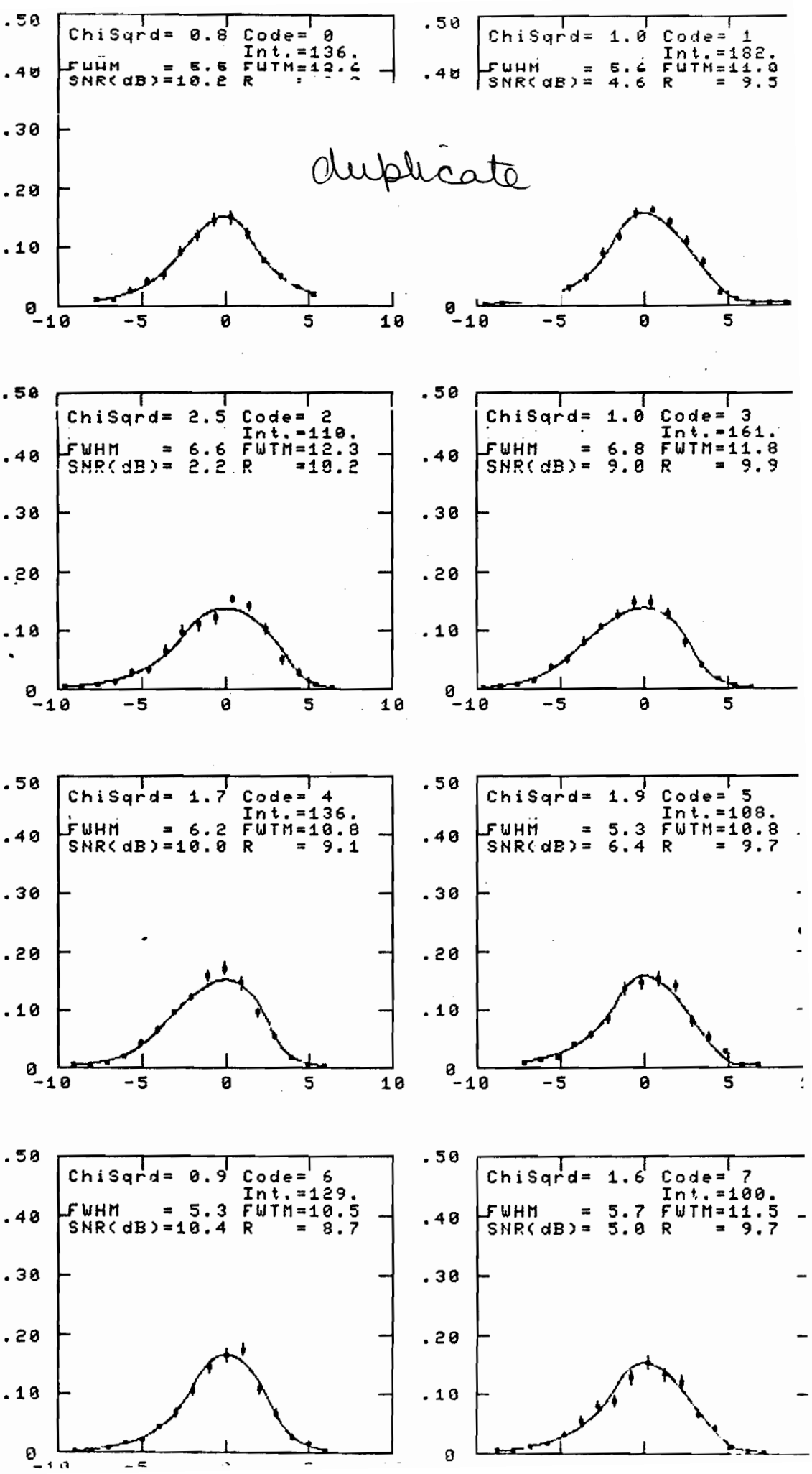

FIGURE 4.5(b) Flat crystals, without tungsten, 20° ray

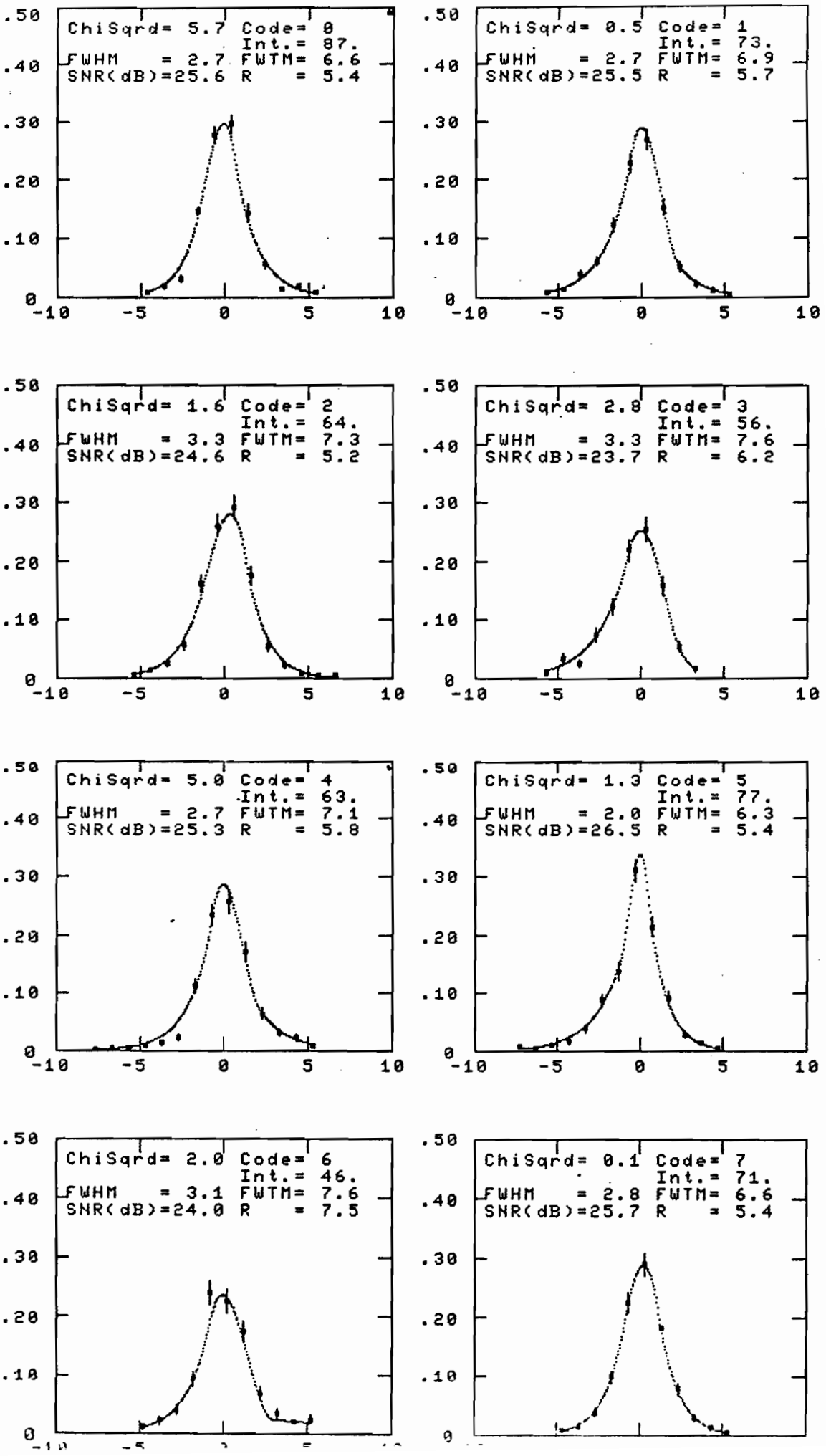

FIGURE 4.5(c) Flat crystals, with tungsten, 0° ray

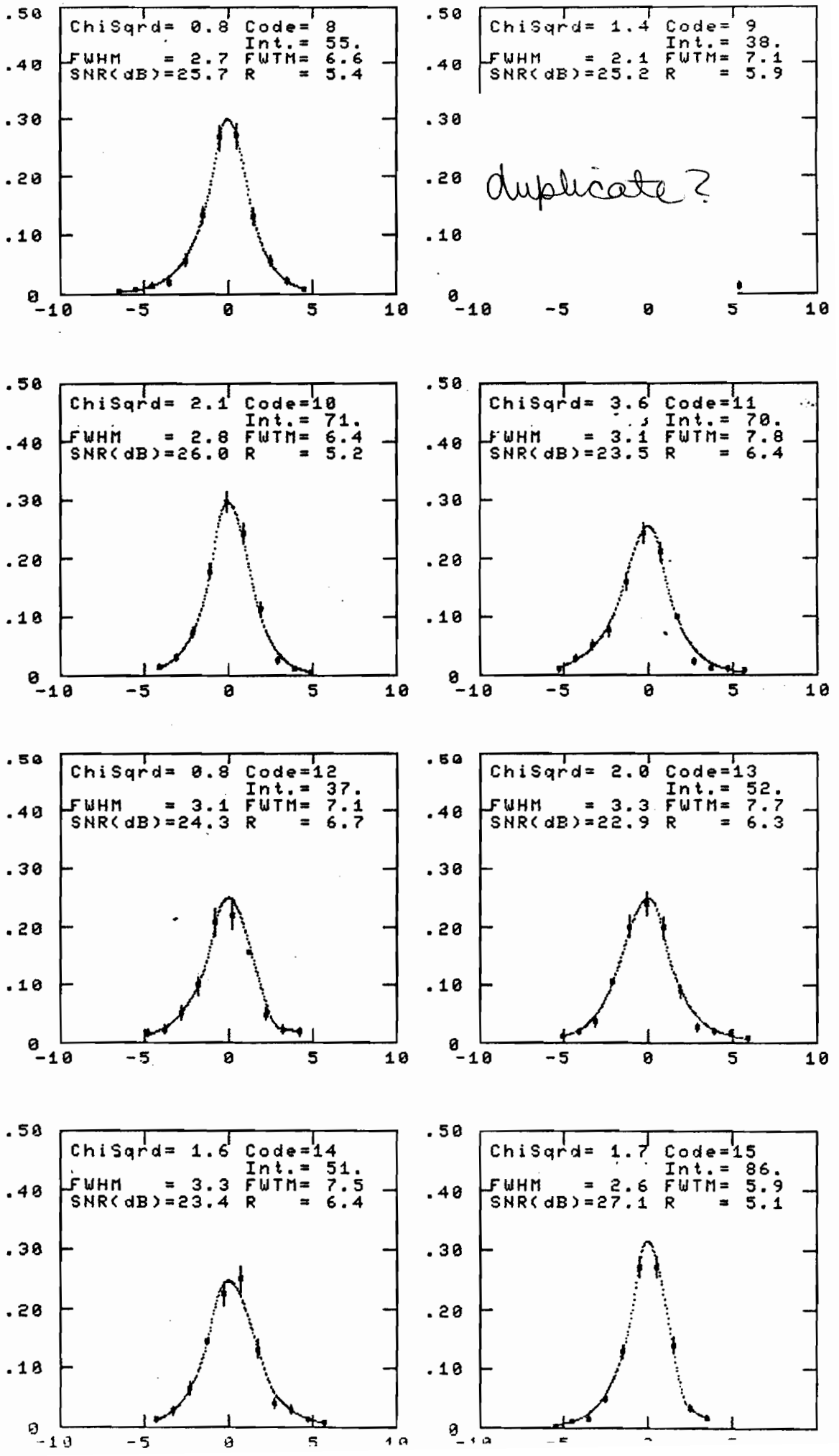

FIGURE 4.5(c) Flat crystals, with tungsten, 0° ray

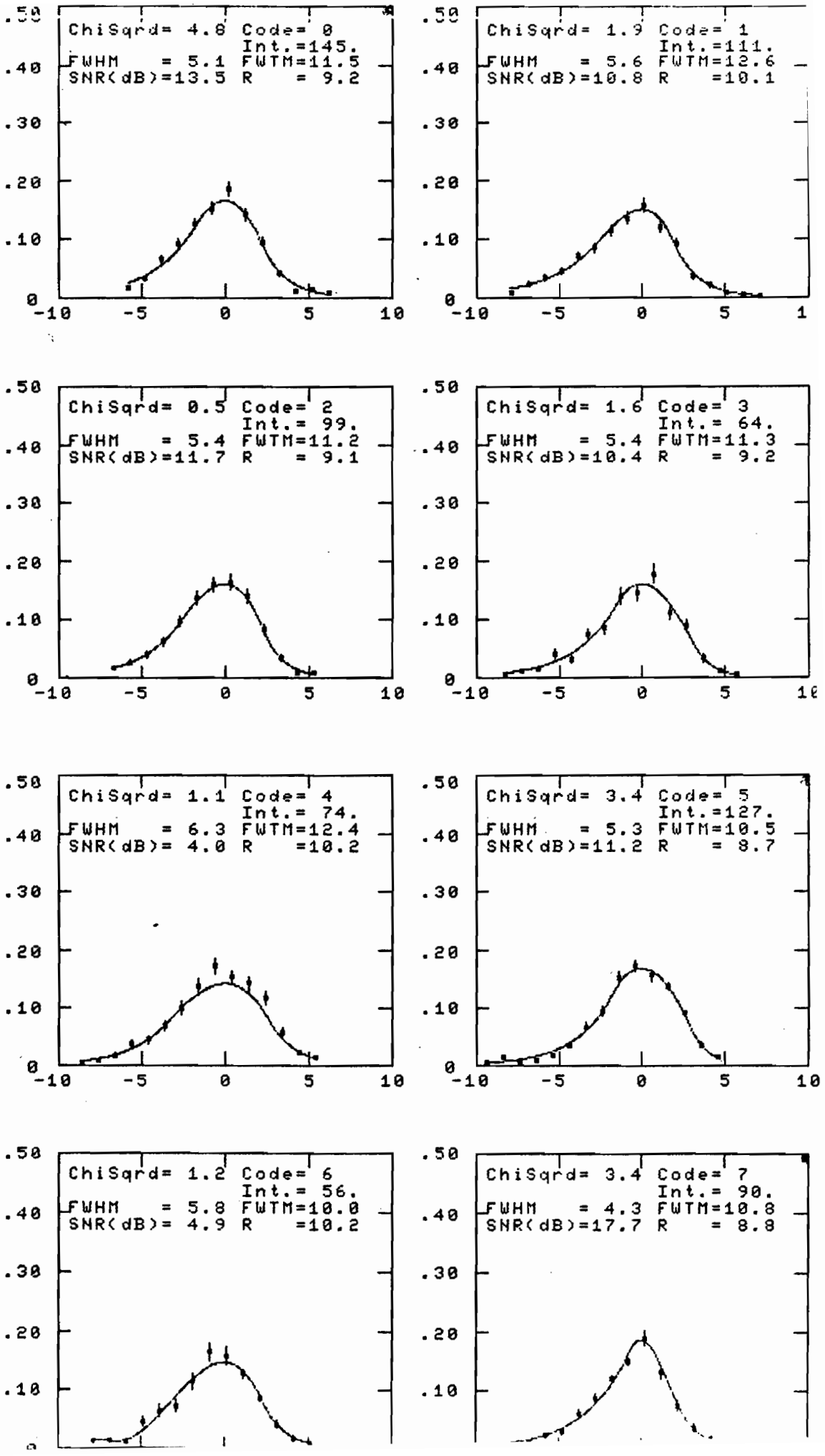

FIGURE 4.5(d) Flat crystals, with tungsten, 20° ray

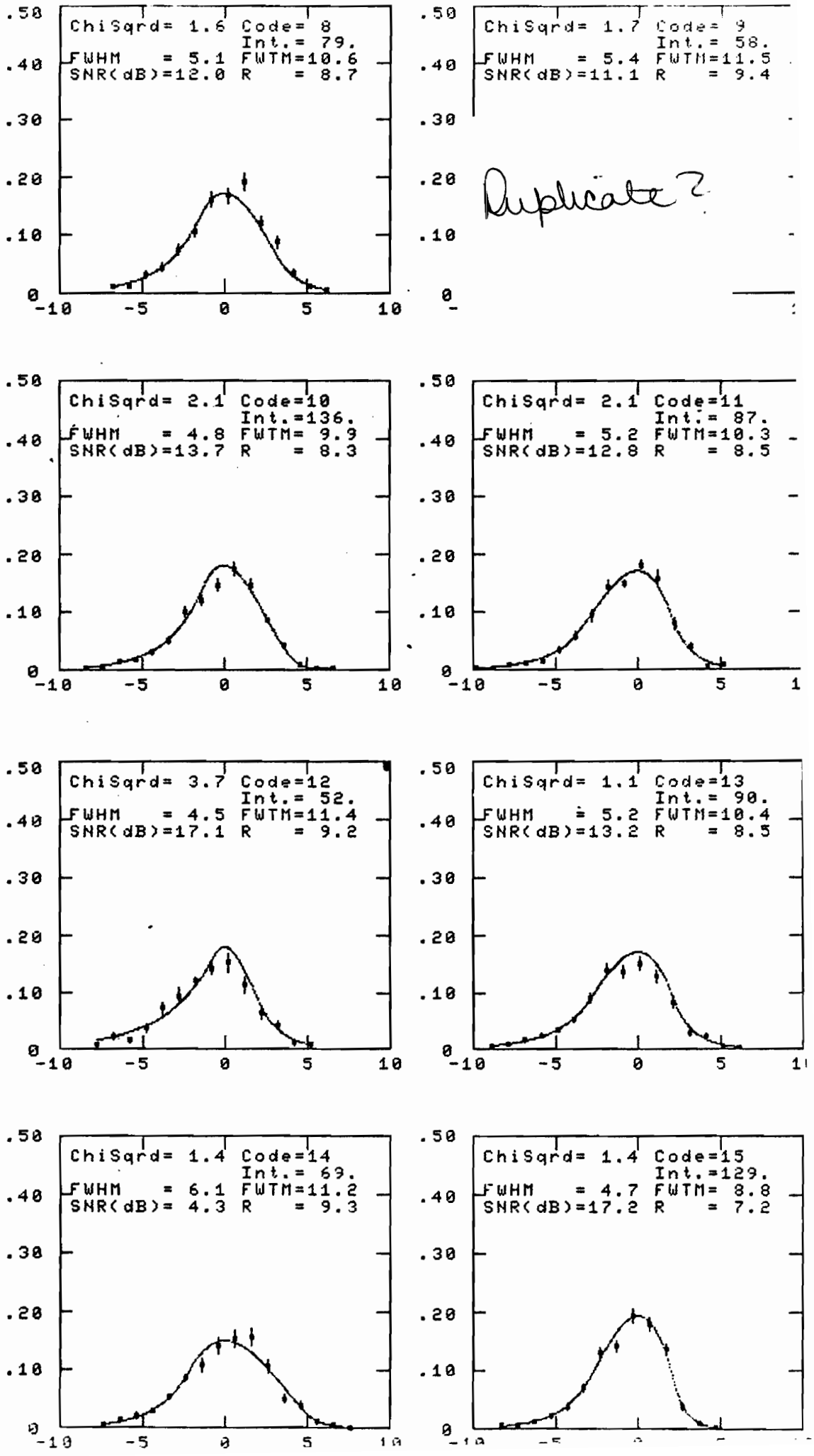

FIGURE 4.5(d) Flat crystals, with tungsten, 20° ray

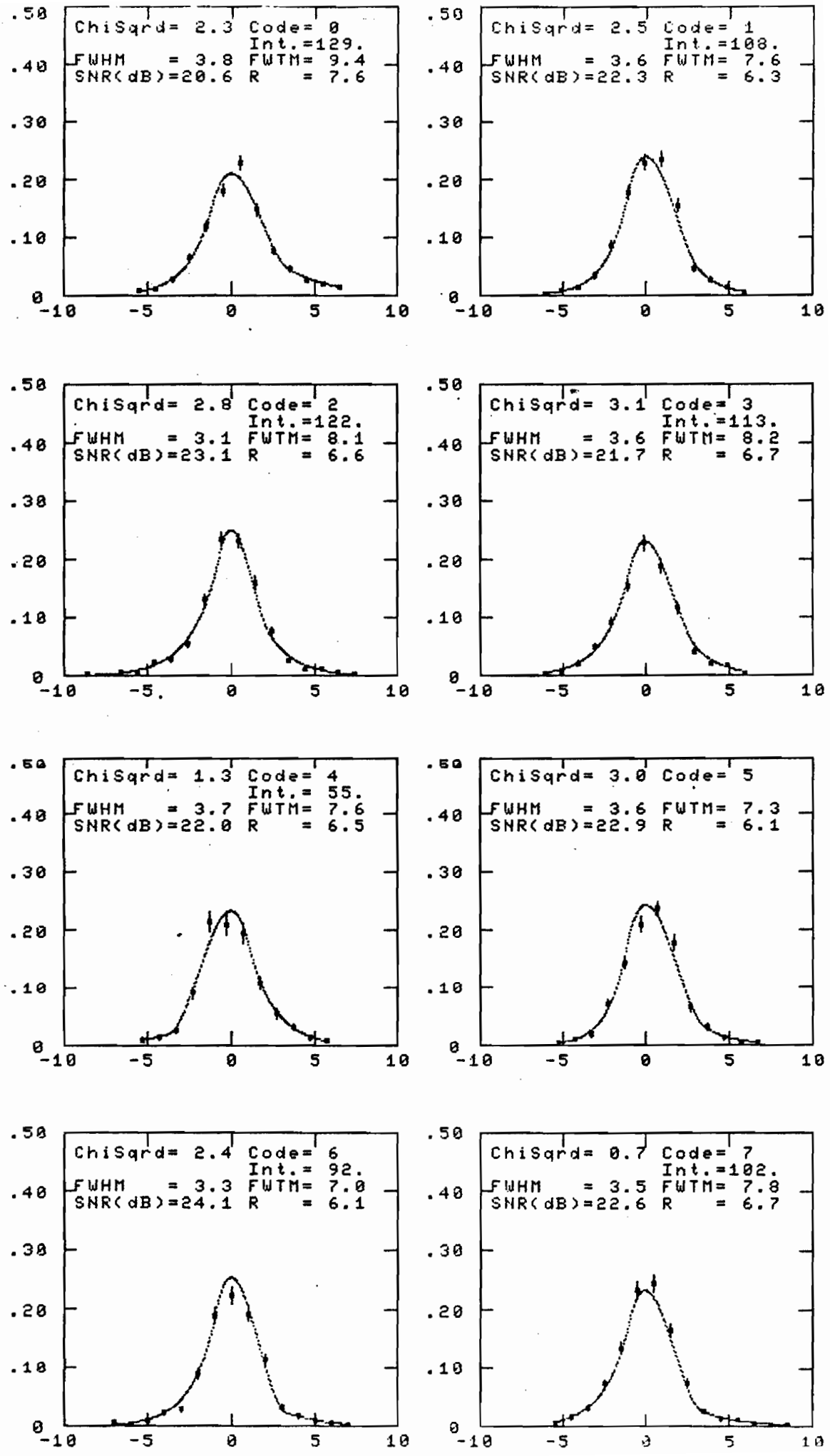

FIGURE 4.5(e) Tapered crystals, without tungsten, 0° ray

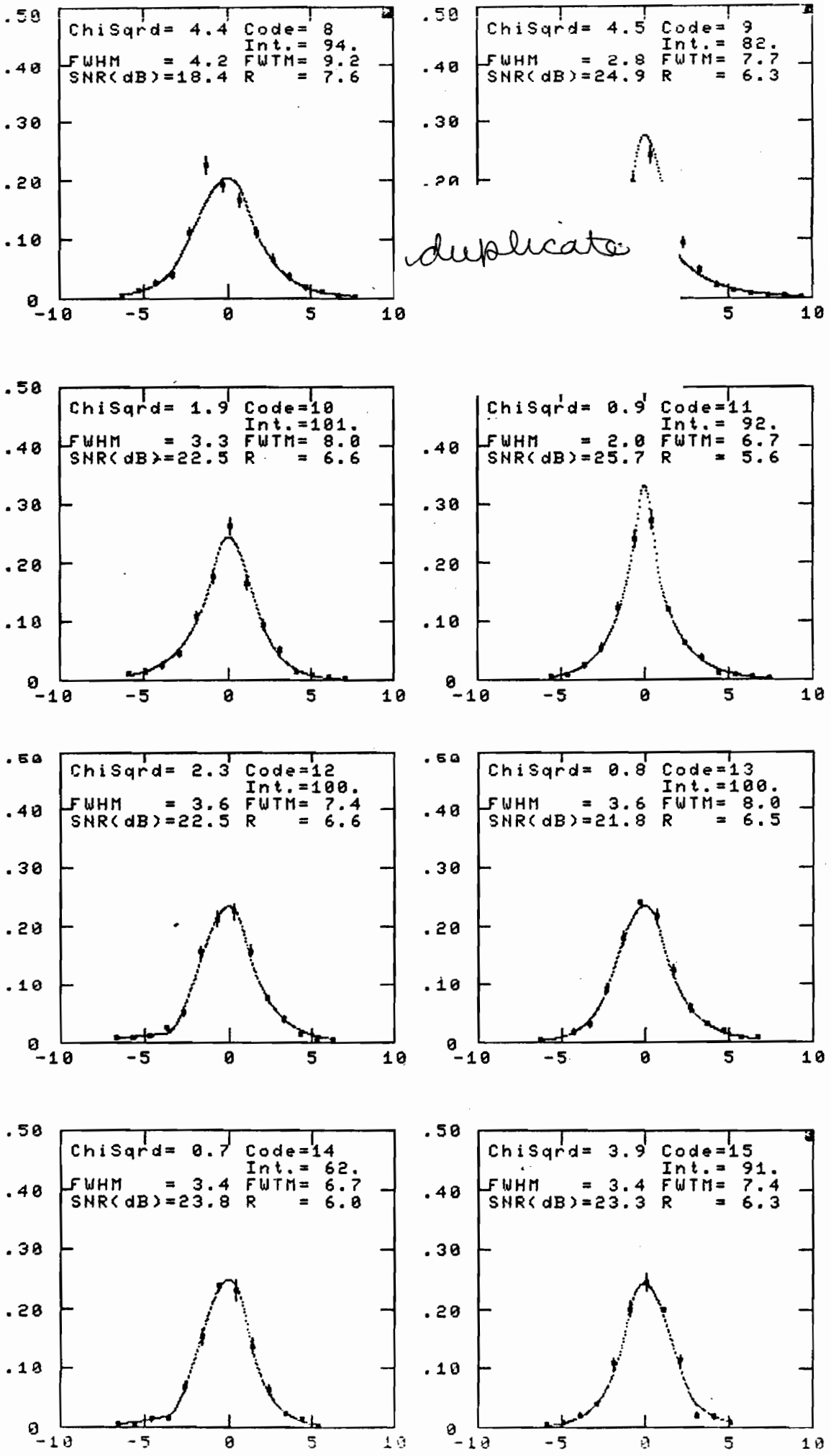

FIGURE 4.5(e) Tapered crystals, without tungsten, 0° ray

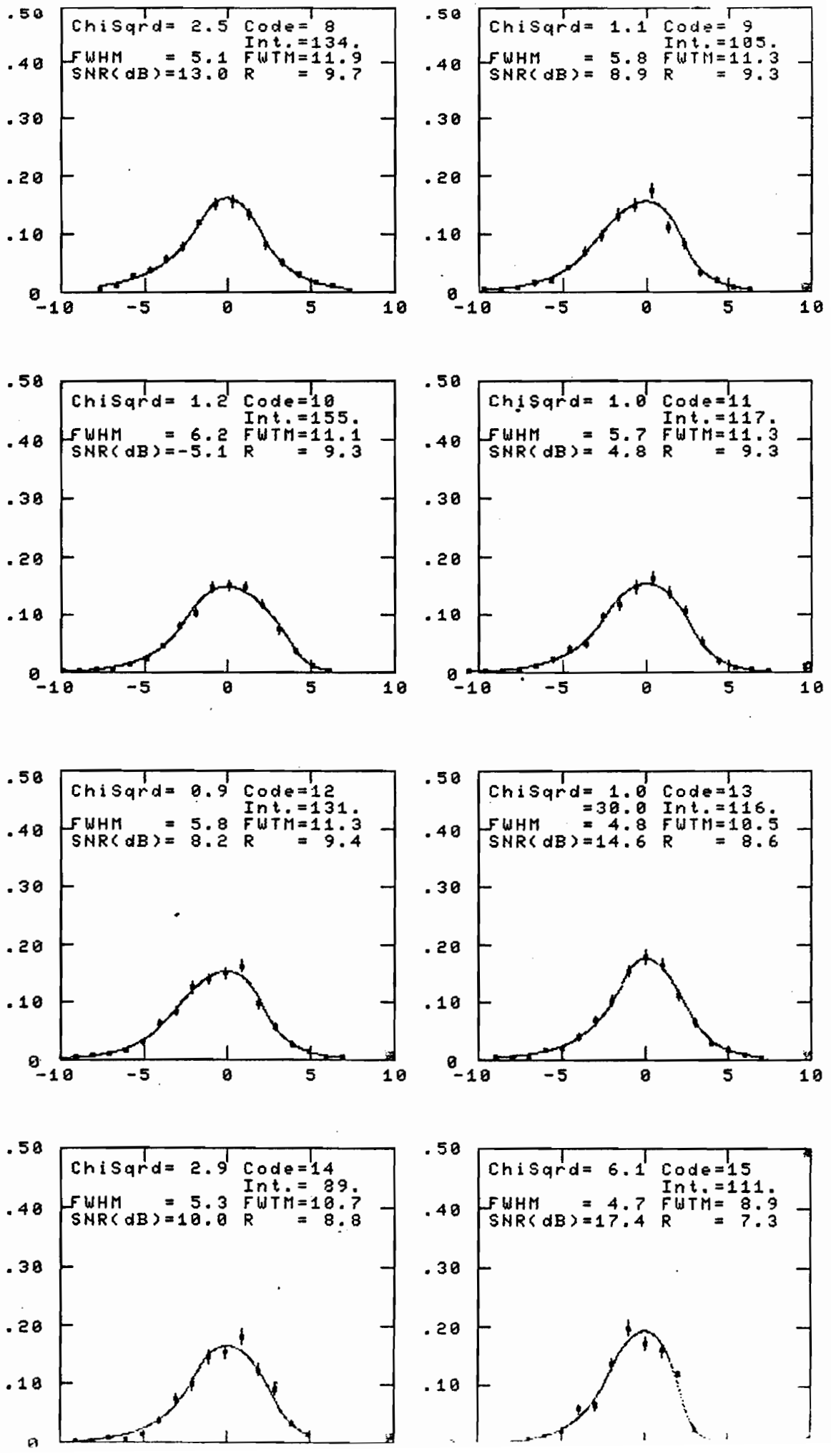

FIGURE 4.5(f) Tapered crystals, without tungsten, 20° ray

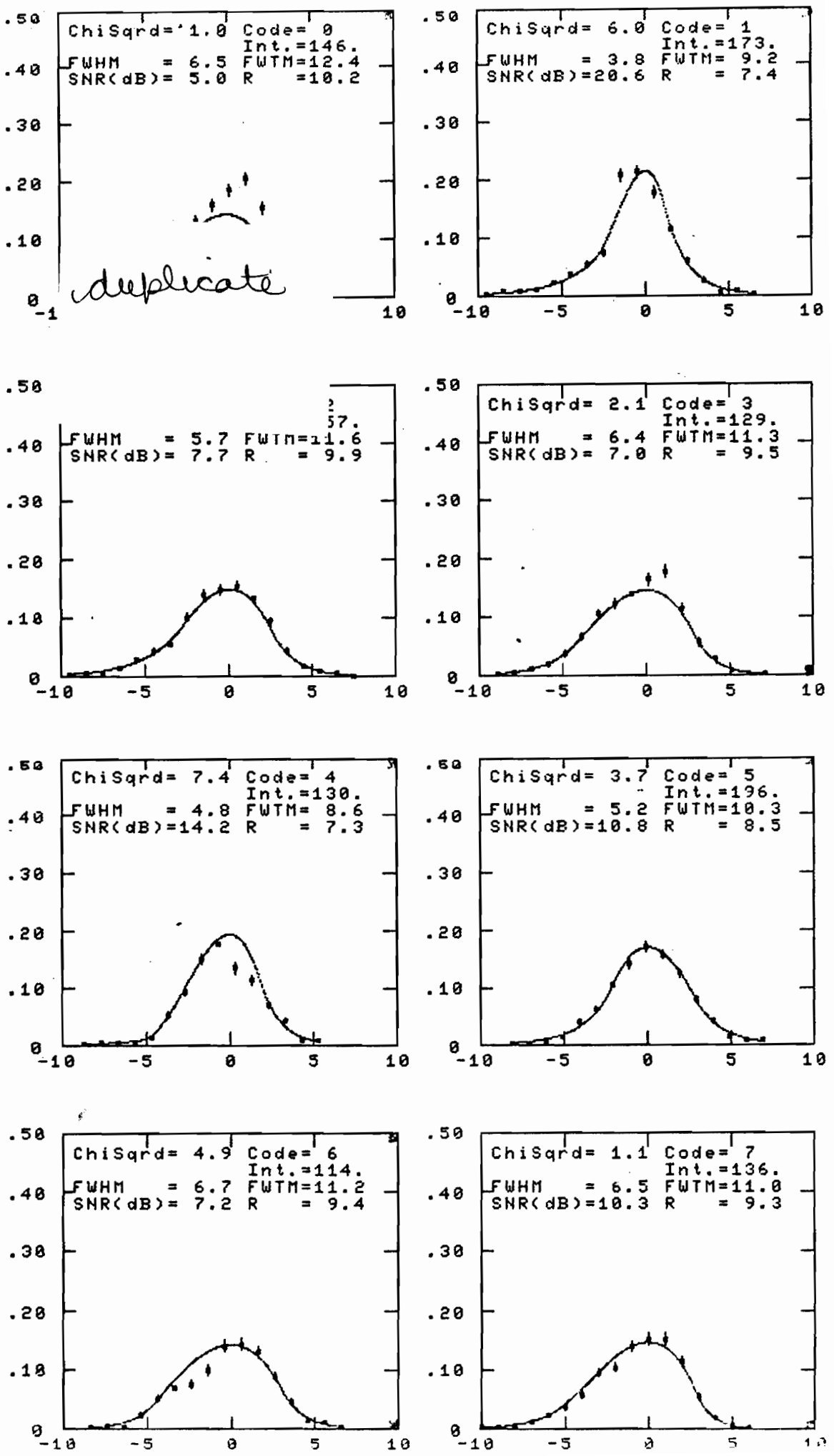

FIGURE 4.5(f) Tapered crystals, without tungsten, 20° ray

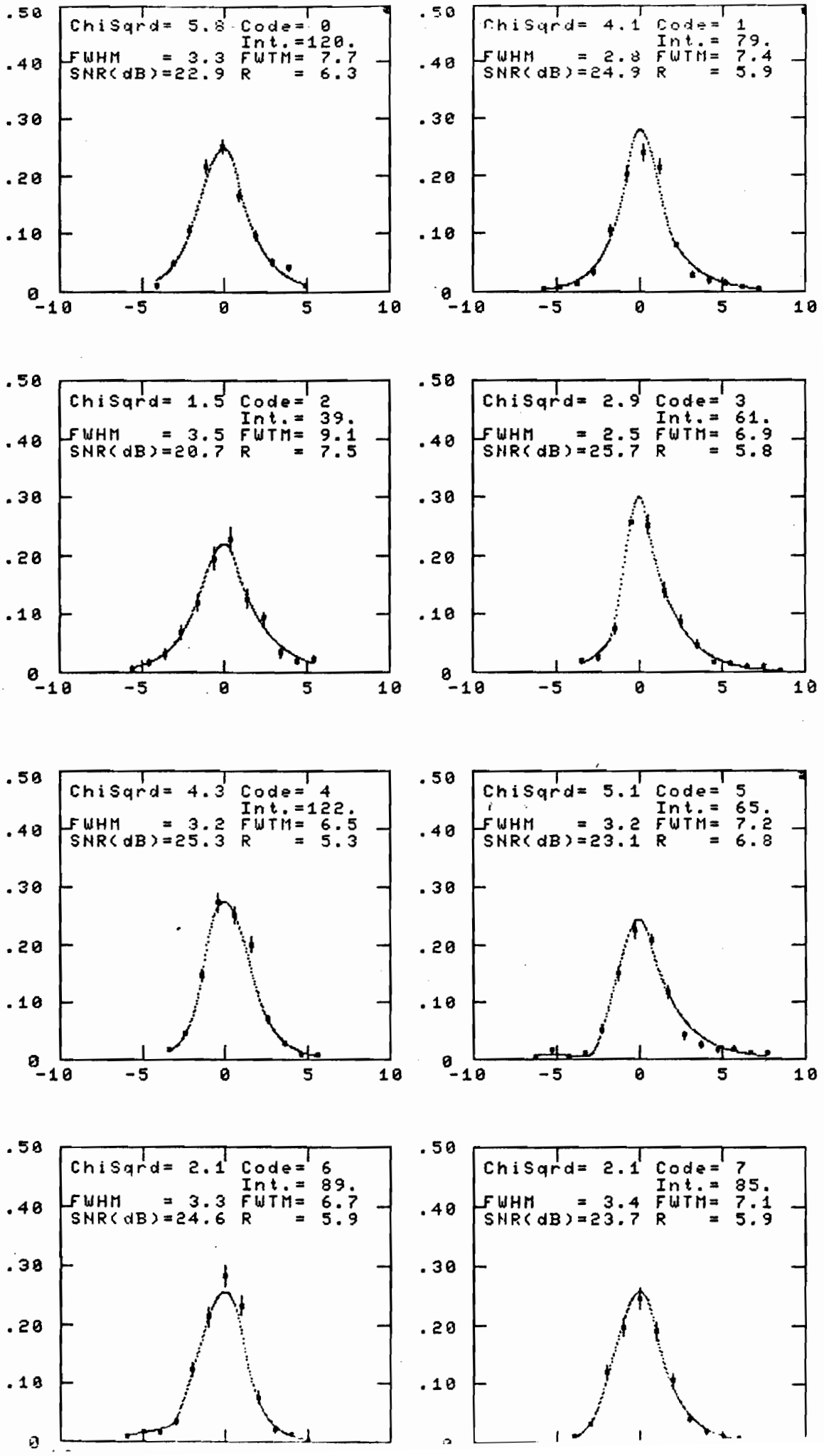

FIGURE 4.5(g) Tapered crystals, with tungsten, 0° ray

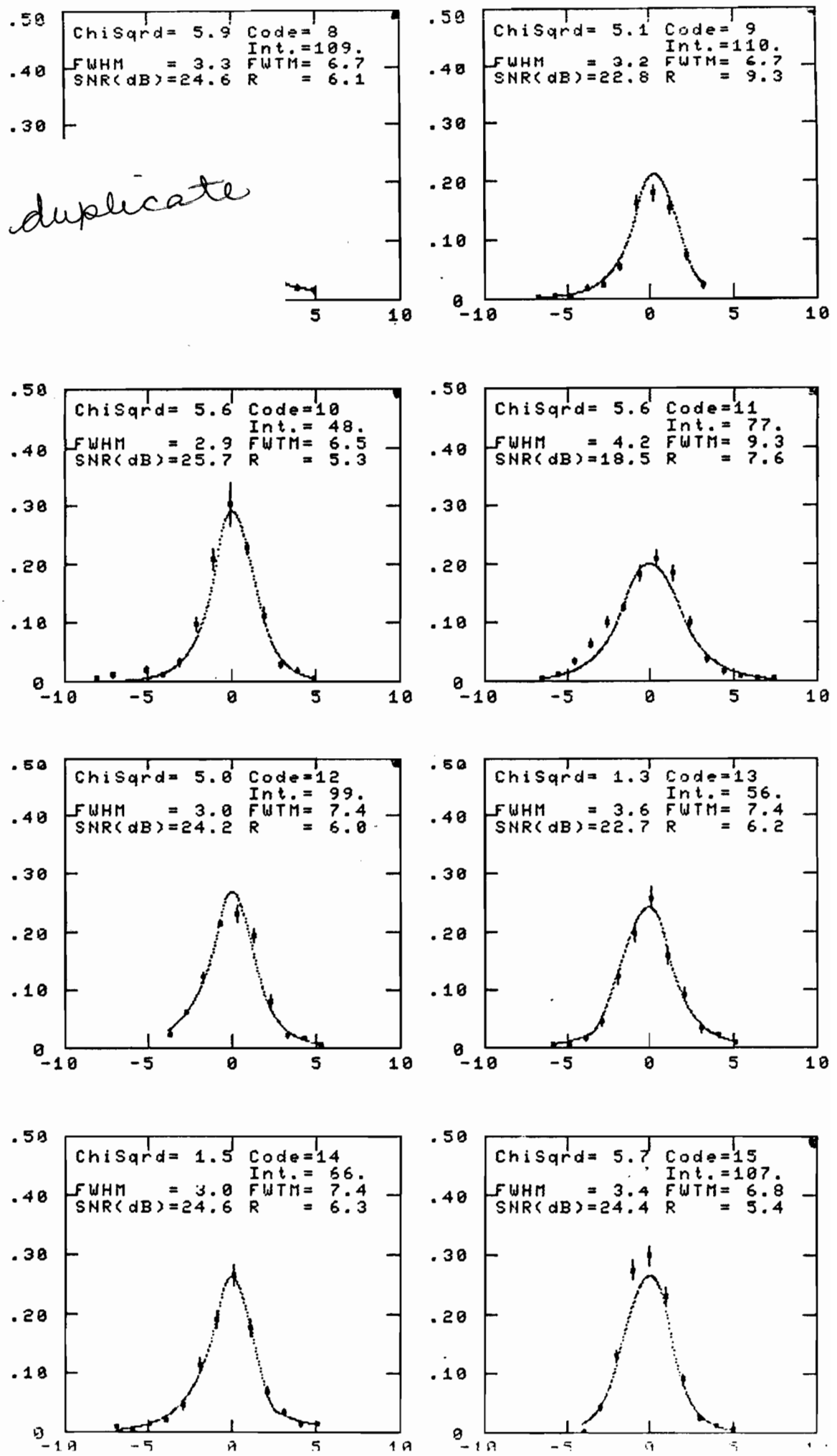

FIGURE 4.5(g) Tapered crystals, with tungsten, 0° ray

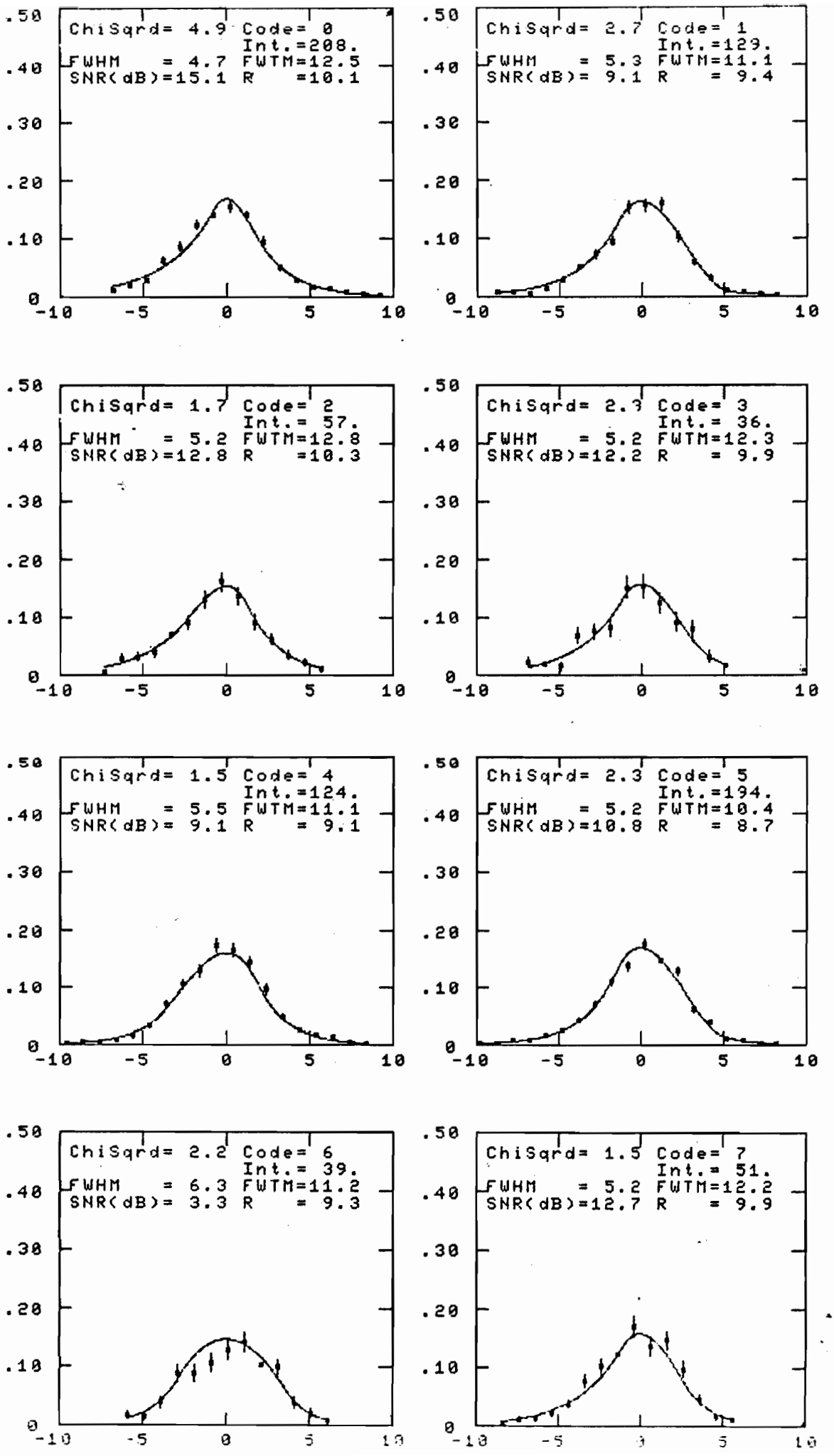

FIGURE 4.5(h) Tapered crystals, with tungsten, 20° ray

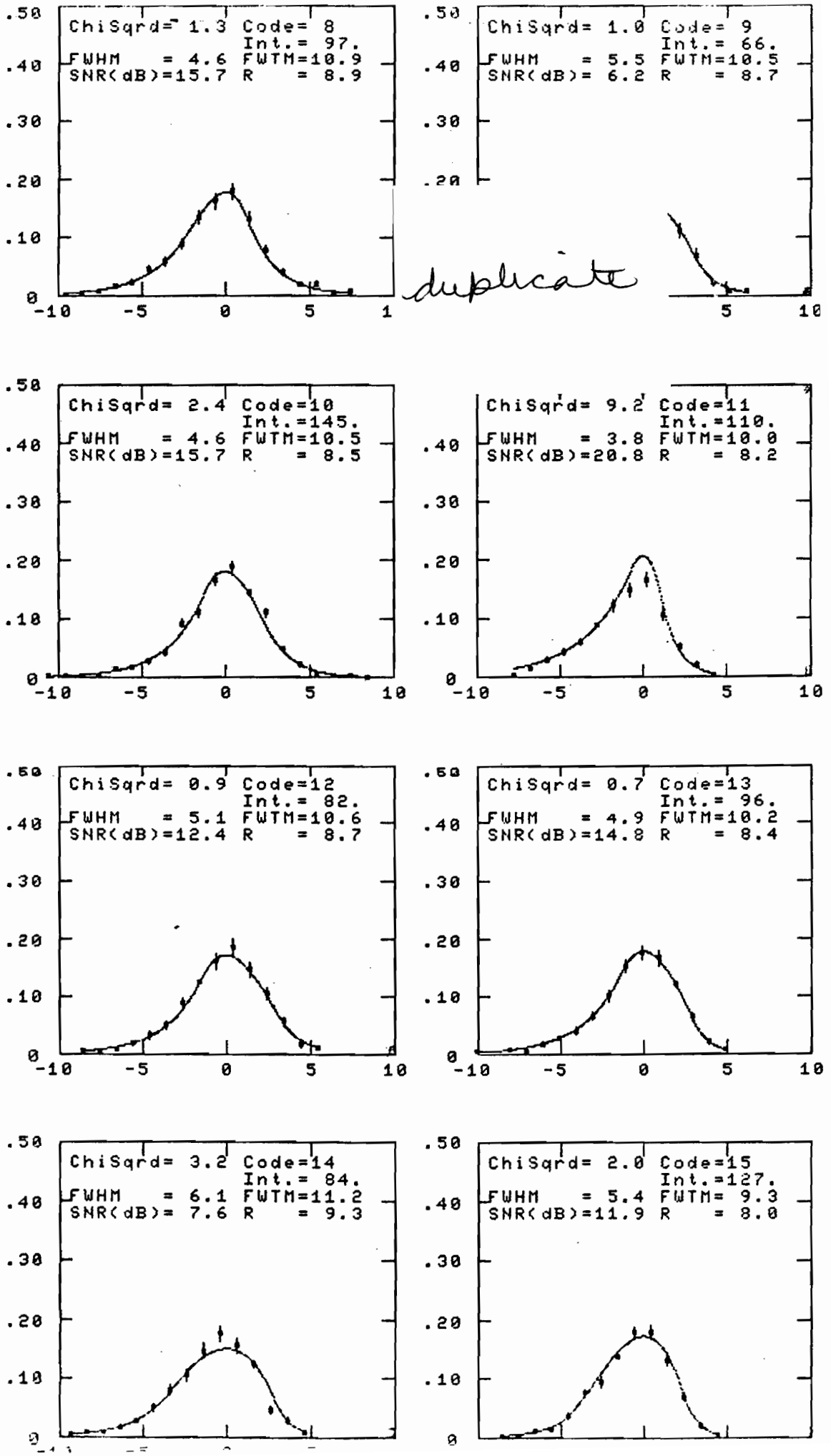

FIGURE 4.5(h) Tapered crystals, with tungsten, 20° ray

TABLE 4.4 SUMMARY OF APERTURE FUNCTION MEASUREMENTS

		Flat Crystal Face		Tapered Crystal Face	
		Without Tungsten	With Tungsten	Without Tungsten	With Tungsten
0° rays	FWHM (mm)	3.3 ±.4	2.8 ±.6	3.4 ±.5	3.2 ±.4
	FWTM (mm)	7.6 ±.7	7.0 ±.6	7.7 ±.7	7.3 ±.9
	R (mm)	6.5 ±1.6	5.9 ±.7	6.5 ±.5	6.1 ±.7
	SNR (mm)	23.3 ±1.6	24.9 ±.7	22.7 ±1.3	23.9 ±1.7
	INT (arb)	83 ±25	61 ±15	98 ±21	74 ±27
20° rays	FWHM (mm)	5.8 ±.5	5.4 ±.5	5.8 ±.6	5.5 ±.5
	FWTM (mm)	11.3 ±.6	10.8 ±1.1	11.1 ±.3	10.9 ±1.0
	R (mm)	9.5 ±.5	9.1 ±1.1	9.2 ±.3	9.0 ±.7
	SNR (mm)	7.2 ±2.8	10.5 ±4.1	9.1 ±3.1	10.1 ±4.0
	INT (arb)	131 ±33	88 ±30	133 ±27	103 ±51

CHAPTER FIVE

Conclusion and Discussion

The various experiments conducted during this study have examined the characteristics of a quad BGO detector and have investigated the consequences of using inter-crystal septa and tapered crystals. It has been shown that satisfactory timing and spatial resolutions can be obtained with the quad detector. The insertion of septa does not significantly increase the overall signal-to-noise ratio even at high spatial frequencies nor does it significantly improve the spatial resolution. Crystals with a tapered piece added to their faces do not have a significantly better spatial resolution for angled gamma rays.

Any improvements in the spatial resolution for angled gamma rays, that may occur when tungsten sheets are inserted between crystals are less than the error margins of these experiments (i.e. less than approximately .5mm). The SNR, as defined by Lecompte et al [1984], calculated at a frequency of .182mm^{-1}, is not significantly improved by the insertion of septa, and appears to decrease, once the drop in efficiency associated with both the reduced packing fraction and the absorption of gamma rays in the tungsten is taken into consideration. The marginal resolution gains do not justify the accompanying drop in SNR at lower frequencies, caused by the decreased efficiency. Therefore , it is recommended that septa not be used with narrow detectors. This is basically the same conclusion reached by Nahmais et al [1980] after experimenting with 8mm wide crystals.

The addition of points to the crystal faces does not significantly change the spatial resolution for gamma rays incident at oblique angles. The measurements conducted here used crystals with a 70° point, which is optimal for a 35° ray. The 35° corresponds to a 46cm diameter tomograph ring using a 26cm diameter reconstruction circle. The gamma rays emerging from the edge of a 16cm diameter head that is centred in the tomograph, have an angle of incidence of 20°. A 20° ray encounters, on average, almost 2mm more BGO when the 70° points are added. The large errors associated with the measurement of SNR prevent one from using this data to investigated the effect of the points on the uncorrected SNR. However, because there is more detector material presented to the incoming gamma ray, it follows that the efficiency will increase, as demonstrated by the monte carlo simulation of Cho et al [1984]. The results of this simulation are corroborated by the results of the experiment summarized in Table 3.1. These indicate that the single gamma inter-crystal cross talk is reduced when points are used. However, the aperture function measurements show that no significant improvement in the resolution can be expected when the points are added. Cho et al [1984] present simulation results that imply that the resolution will be significantly improved with the addition of points. This is not the case for narrow crystals, in fact, as these measurements, and the calculations of Lupton et al [in press] demonstrate. Much of the improvement in crystal penetration cited by Cho et al [1984] can be accounted for by recognizing that the addition of points has the effect of redefining the radius of the tomograph ring. Instead of being measured from the centre

to the tip of the points of the crystals, the radius is extended to the base of the points. The result of this, is that the 'primary detector' (i.e. the one that is supposed to record the event), for angled rays, is redefined as the detector that used to be considered an adjacent detector. This redefinition of the 'primary detector' will improve the image quality. The use of an effective detector ring diameter greater than the face to face distance is commonly used to reconstruct images to take the effect of crystal penetration into account. This is because events will have a higher probability of being recorded in the 'correct detector' for angled rays. However, it cannot be expected to improve the spatial resolution. The improvement in spatial resolution will depend on the amount of material in the point. Therefore, for narrow crystals, which have little BGO in the point, no significant improvement in resolution can be expected. This was predicted by Lupton et al [in press] using an attenuation coefficient calculation, and this is what has been measured here. If the point, instead of being added, was cut away from the face of the crystal, the efficiency would drop and some improvement in resolution might be expected. But the improvement would be of the same order of magnitude as the improvements obtained using 1mm tungsten septa. Such a meagre gain in resolution does not justify the efficiency loss. Perhaps the best approach to be taken, with respect to the use of points, is to determine the optimal ring radius and reconstruction circle diameters based on other considerations (such as desired sensitivity, resolution, cost etc.) and then add an appropriately shaped point to the crystal face in order to boost the efficiency.

The quad BGO detector has been shown to be an effective means of using narrow crystals in a reasonably high packing fraction configuration. A detector pair using 4.5mm crystals has an aperture function FWHM of (3.3±.3)mm and a FWTM of (7.6±.5)mm for 0° incident gamma rays. These values are (5.8±.4)mm and (11.2±.3)mm for 20° incident gamma rays. The crystal identification encoding-decoding errors do not significantly affect the FWHM, but do increase the FWTM by (20±7)% and decreases the SNR. These statements are based on comparisons of the experimental and monte carlo simulated aperture function determinations. The energy and timing resolutions of this detector are greatly affected by poor photoelectron statistics. Any procedure that would increase the number of photoelectrons, such as by using a paint with a higher reflectivity ($BaSO_4$ with polyvinyl alcohol, for example [Okajima et al, 1982]), would improve the energy and timing characteristics. Because of the simplicity of the crystal identification scheme, the cost of the electronics per crystal of a system incorporating such a detector is comparable to that of the MNI's Positome III camera. Moreover, since the cost of the crystals is dominated by the volume of BGO, rather than by the fabrication labour costs, the spatial resolution of a PET system could be almost doubled for a small cost in discriminator complexity. A reasonable cost estimate of a ring of 320 crystals (excluding the electronics), for example, is (1984US)$80,000. [Thompson,1984] This estimate breaks down as follows: $20,000 for 320 30mmx15mmx4.5mm BGO crystals, $30,000 for 80 Hamamatsu R1548 PMT's and bases and $30,000 for packaging, shielding and testing. This compares

quite favourably with the cost of a Positome III ring (64 30mmx30mmx20mm BGO crystals and 64 Hamamatsu R1213 PMTs) which was (1977US)$68,000. This design provides a cost effective detector module which achieves high resolution while maintaining the high efficiency required in PET.

APPENDIX ONE

SOME PHYSIOLOGICAL STUDIES WITH POSITRON TOMOGRAPHY

Positron Emission Tomography, alone, has made possible the in vivo study of many quantifiable physiological process in the human body. Such studies examine, for example,

-the regional metabolism in the brain and heart,

-the permeability of tissue,

-the size of infarcts left in the heart following coronary attack,

-regional blood volume and flow,

-assessment of the effects of drugs on diseased or malfunctioning tissue,

-the measurement of the effect of treatment of cancers by examining changes in the the malignant tissue and by the biochemical reactions of the normal tissue around it,

-cerebrovascular disease,

-epilepsy,

-physiology of psychoses, and others.

A few, specific examples of the types of studies undertaken at the Montreal Neurological Institute and the associated labelled compounds include: glucose utilization using ^{18}F labelled 2-fluoro-2-deoxyglucose (FDG), oxygen consumption using $^{15}O_2$, regional cerebral blood flow using $C^{15}O_2$, and the effects of therapeutic agents such as ^{11}C labelled 1,3 bis(2-chloroethyl)-nitro-sourea (BNCU). The study of glucose utilization and oxygen consumption in patients with a tumour, for

example, show that glucose metabolism is increased while oxygen extraction is reduced at the site of the tumour. Examination of BNCU distributions revealed that the agent concentrates in tumours even if the oxygen extraction is reduced.[Yamamoto et al,1984] Such in vivo, localized and quantitative studies cannot, at present, be conducted using any other technique, and have been made possible by the physical properties of the annihilation process fortuitously combined with the availability of physiologically interesting positron emitting compounds.

APPENDIX TWO

Physical Processes of Positron Emission and Detection

If a nucleus has one or more protons or neutrons in excess of a stable configuration of nucleons, it will undergo beta decay. An excess of neutrons leads to beta minus decay, in which the neutron is transformed into a proton with the transformation being accompanied by the emission of an electron and anti-neutrino. An excess of protons leads to beta plus decay, in which positron and neutrino emission accompany the transformation of the proton into a neutron. In PET, isotopes are created (usually through proton or deuteron bombardment in an accelerator) which have an excess number of protons in their nuclei, and which therefore emit positrons. When a positron is emitted it has fixed probability of having an energy between E and E+dE, with E ranging from zero to some 'end-point energy': E_{max}. The value of E_{max} and the shape of the energy probability distribution depend on the parent nuclide, with the value of E_{max} for positron emitters ranging from tens of keV to several MeV. Travelling through the surrounding medium, the emitted positron loses energy through ionization and excitation interactions with the orbital electrons of the medium (collisional loses) and, to a much lesser extent (less than 1% of the total energy lost), bremsstrahlung processes. In this way most positrons emitted into a non-gaseous medium are thermalized within a few millimetres of their parent nucleus in a period of picoseconds.[Knoll p58, 1979] The actual range of the positron depends strongly on its initial energy and the electron density of the absorbing

medium. Because of the influence that the positron range can have on the spatial resolution of a PET system, a number of studies have examined the range of positrons emitted from biomedically important nuclides in a medium of the biologically ubiquitous water.[Derenzo,1979; Cho et al, 1975; Hoffman and Phelps, 1974] The range can be described in terms of the parameter λ [cm^2/g] such that the number of positrons transmitted through a medium of thickness, x, can be expressed as:

$$N = N_o \cdot \exp (-\lambda \cdot x) \qquad [A2.1]$$

where: N_o is the initial number of positrons.
N is the number of positrons transmitted.

The value of λ can be determined by an empirical formula, such as,

$$\lambda = 17.0 \cdot E_{max}^{1.43} \quad [cm^2/g] \qquad [A2.2]$$

where: E is the end-point energy of the beta plus spectrum. [Siegbahn, 1965]

Equation A2.2 is valid for beta minus emission where more than half of the electrons are transmitted and the number of low energy electrons is large, but it describes beta plus absorption to within a few percent as well.

As the energy of the positron decreases, the probability of interacting with an orbital electron through the process of annihilation increases such that when the positrons are thermalized, two photon annihilation occurs either within hundreds of picoseconds or, if the positron and electron combine to form a quasistable state called positronium, within hundreds of nanoseconds. Annihilation into more than two photons is also possible but with a much smaller probability than two photon annihilation (10^{-4} times lower) [Deutsch,1953] and single photon decay is obviously prohibited by momentum conservation. Due to the

conservation of energy and momentum, the 1.022MeV energy of the mass of a stationary electron-positron pair, when transformed into electromagnetic energy through the two photon annihilation process, must be distributed equally between the two photons (511keV each) and the photons must have oppositely directed momenta (i.e. they must be colinear). However, in general the positron has a residual momentum, as does the orbital electron with which it interacts. The resulting centre-of-mass motion of the electron-positron pair causes a doppler broadening of the 511keV gamma ray energies and a deviation of the relative gamma ray directions from 180°. For a water absorber, the broadening is approximately 2.6keV. This corresponds to an average centre-of-mass momentum, $\bar{p}$, of $5 \times 10^{-3} mc$ which in turn is directly related to the angular deviation from colinearity:

$$\alpha \approx \bar{p}_z / mc. \qquad [A2.3]$$

The distribution of relative gamma ray directions can be approximately described as a gaussian with a mean of 180° and a FWHM of 0.5°.[de Benedetti et al, 1950 and Colombino et al, 1965] The doppler broadening and deviation from colinearity depend on the electronic structure of the absorbing material and on whether or not positronium had been formed. Precision measurements of the broadening or deviation from non-colinearity provide a means of studying the electronic structure of the absorber. However, because the dependence of the distributions on the absorber and the state of the electron-positron pair introduce minor corrections to the gaussian distribution described above, they are not

considered significant dependencies in PET. [Brooks, 1981] For the purposes of PET the doppler broadening is not significant at all since energy resolution is not a critical factor, but the non-colinearity is significant for large volume or high resolution detection systems.

The 511keV gamma rays lose energy either through photoelectric absorption or Compton scattering, but obviously not through pair production (511keV being half the threshold for the pair production process). The Compton scattering cross section depends on the number of electrons available as scattering targets and therefore increases linearly with the atomic number, Z, of the absorbing material. The cross section is described by the Klein-Nishina formula:

$$\frac{d\bar{\sigma}}{d\Omega} = \frac{\alpha^2}{2m^2}\left[\frac{k'}{k}\right]^2\left[\frac{k'}{k}+\frac{k}{k'}-\sin^2\theta\right] \qquad [A2.4]$$

where: k is the incident photon energy.
k' is the scattered photon energy.
θ is the scattering angle.
α is the fine structure constant

and $k' = k\left[1+\frac{k}{mc^2}(1-\cos\theta)\right]^{-1}$

The relation between the photoelectric cross section and Z can be approximated by:

$$\sigma_{PE} \approx \text{constant} \cdot Z^{f(E)}/E^{g(Z)} \qquad [A2.5]$$

where:
f(E) increases from about 4.0 to 4.6 between the energies of 1keV and 3MeV with a value of 4.4 at 511keV.
g(Z) has a complicated Z dependence but which can be approximated by the constant value of 3.[Evans, pp698-700, 1955]

In a PET system one wishes to include only coincidence events that are related to gamma rays from the same annihilation and that have

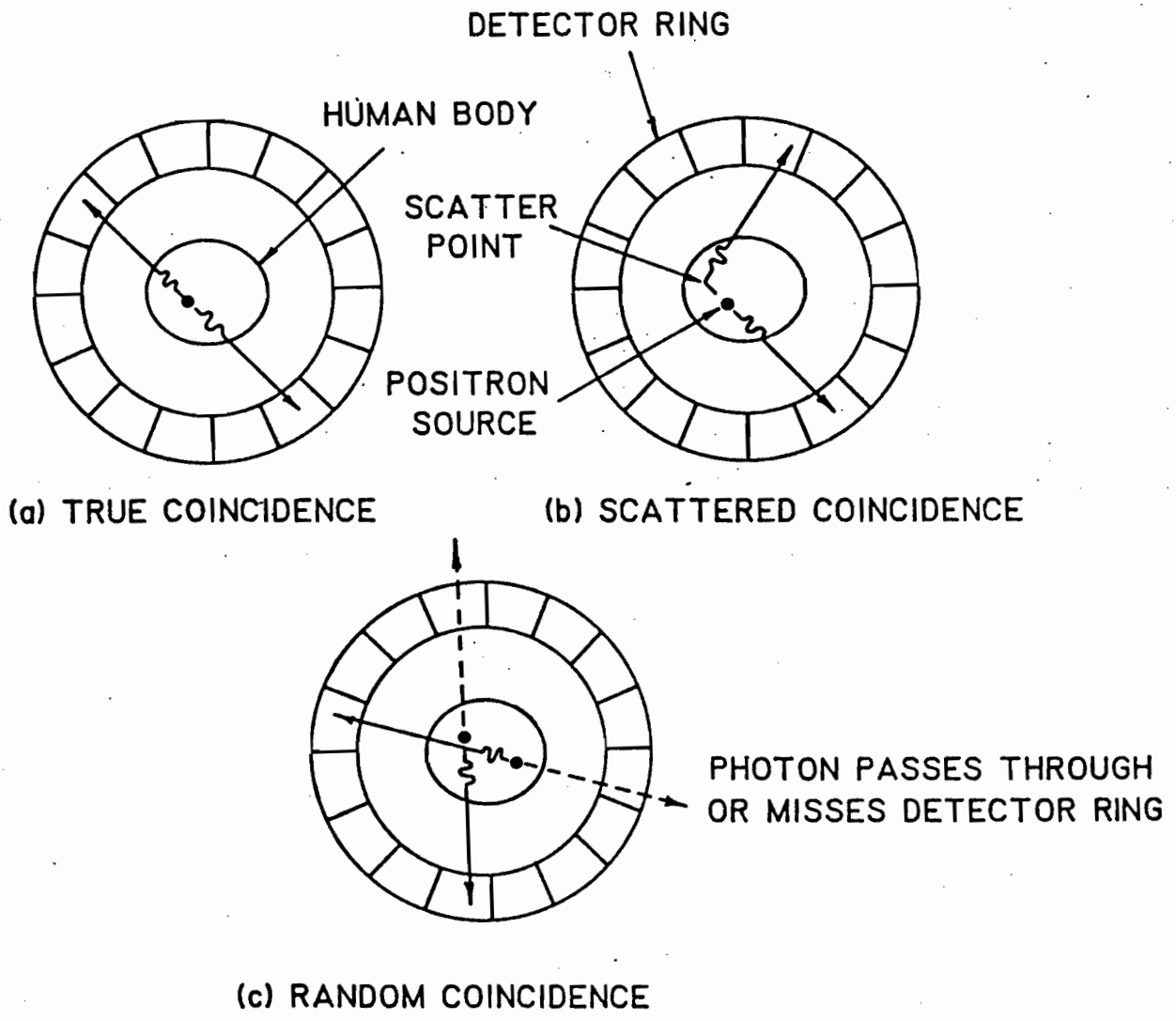

Figure A2.1 Three Types of Coincidence Events That Occur in Positron Emission Tomography [From Lupton and Keller, 1982]

not been scattered in the body prior to detection. These are referred to as 'true coincidences' (see Figure A2.1(a)). However, in reality, the coincidence events include those related to scattered gamma rays (Figure A2.1(b)), and coincidences which occur when two gamma rays emitted in different annihilations are detected within the resolving time of the coincidence circuit (Figure A2.1(c)). The random coincidence rate is given by:

$$R_T = 2\,\tau \cdot S_1 \cdot S_2 \qquad [A2.6]$$

where: 2τ is the coincidence resolving time.
S_1 and S_2 are the singles rates in the two detectors.

Random coincidences are reduced by using as narrow a timing window as possible. The data can be corrected for randoms by either using equation A2.6 (and by measuring the singles rates or by shifting the timing window off coincidence) or by noting the number of coincidence events that occur between detectors that are joined by a chord that does not cross a region of activity (such as at the periphery of the tomograph).

The fraction of scattered coincidences depends on the slice thickness, collimator depth, and detector size.[Derenzo,1980] This fraction can be reduced by increasing the lower level of the energy window. The optimum threshold is 350keV [Lupton et al, 1984]. The data can be corrected for the scatter by deconvolving the effects of scatter from the profiles using a measured scatter profile. In addition, a correction for the attenuation of gamma rays is required. The attenuation has the effect of lowering the values of the projections by a

factor p:

$$p = \exp\left[-\int_{\ell} \mu(s)\, ds\right] \qquad \text{[A2.7]}$$

where: μ is the attenuation coefficient
ℓ is the projection line.

This effect can be accounted for by either measuring p in a transmission scan, or by using an estimated value of μ and measuring skull dimensions (for brain scans). It should be noted that the scatter corrections are influenced by μ and, in fact, can be partly accounted for by using a lower value of μ.

APPENDIX THREE
Spectral Resolution and Signal-to-Noise Ratio

The fourier transform of an aperture function normalized by its total integral, AF(x), can be expressed in terms of the 'modulation transfer function', MTF(ν), and the phase transfer transfer function, PTF(ν):

$$FT\{AF(x)\} = MFT(\nu) \cdot \exp(i \cdot PTF(\nu)) \qquad [A3.1]$$

The MTF is the modulus of the fourier transform of AF(x), and is normalized to 1 at ν=0. The detector system can be thought of as a spatial filter that has a spectral response, MFT(ν), and power characteristic, $[MFT(\nu)]^2$. The 'equivalent width' is one measure of the dispersion of a function about a central point: it is the integral of the function divided by the value of the function at the central point.[Bracewell, pp143-155,1978] Lecompte et al [1984] use the equivalent width of the power pass characteristic of this spatial filter to describe the band width of the filter. They refer to it as the 'spectral resolution',R:

$$R = \frac{1}{\int |MTF(\nu)|^2 \, d\nu} = \frac{\left|\int AF(x)dx\right|^2}{\int |AF(x)|^2 \, dx} \qquad [A3.2]$$

Lecompte et al have also derived an expression for the spectral signal-to-noise ratio, a brief review of which follows:
The signal-plus-noise, assuming Poisson statistics, is:

$$h_T(x) = h(x) + [\, h(x) \,]^{1/2} B(x) \qquad [A3.3]$$

where: $h(x) = a X_0 f(x)$

a is the linear density of the incident gamma rays.

X^0 is the effective width of the detector exposed to the gammas.

$B(x)$ is white noise of unity modulus.

$f(x)$ is the probability distribution as given by AF(x).

Using the fact that the total energy density is proportional to:

$$| \, FT \{ h_T(x) \} \, |^2$$

the 'spectral signal-to-noise ratio' was given as:

$$SNR(\nu) = \left[\frac{FT \{ \text{Energy Density due to Signal} \}}{FT \{ \text{Energy Density due to Noise} \}} \right]^{\frac{1}{2}} \qquad [A3.4]$$

From the convolution theorem,

$$\left[FT \{ h_T(x) \} \right]^2 = FT \{ h_T(x) * h_T(x) \} \qquad [A3.5]$$

and using the fact that white noise convolved with itself yields a unity impulse function, and when convolved with any other function yields a zero value, equation A3.4 can be expressed as:

$$SNR(\nu) = \frac{| \, FT \{ h(x) \} \, |}{\left[\int_{-\infty}^{\infty} h(x) \, dx \right]^{\frac{1}{2}}} \qquad [A3.6]$$

References

Anger,H.O., 'Sensitivity, Resolution, and Linearity of the Scintillation Camera', IEEE Trans. Nucl. Sci. NS-13:No.3, p380-392, 1966

Barton,J.B., Hoffman,E.J., Iwanczyk,J.S., Dabrowski,A.J., and Kusmiss,J.H., 'A High Resolution Detection System for Positron Tomography,' IEEE Trans Nucl Sci, NS-30:No.1, pp671-675, 1983

Bellazini,R., Guerra,A.D., Massai,M.M., and Nelson,W.R., 'Some Aspects of the Construction of HISPET: A High Spatial Resolution Positron Tomograph', IEEE Trans. Nucl. Sci., NS-31:No.1, p645-648, Feb. 1984

Blasse,G., 'New Compounds with Eulytine Structure: Crystal Chemistry and Luminescence', J. Solid State Chem., 3:1, pp27-30, 1970

Bortfeld,D.P. and Meier,H., 'Refractive Indices and Electro-Optic Coefficients of the Eulitities $Bi_4Ge_3O_{12}$ and $Bi_4Si_3O_{12}$', J. Appl. Phys. 43:No.12, pp5110-5111, 1972

Boutot,J.P., and Pietri,G., 'Photomultiplier Control by Clamping Cross-Bar Grid', IEEE Trans. Nucl. Sci., NS-19:No.3, p101-106, 1972

Bracewell,R.N., The Fourier Transform and Its Applications, 2nd ed., McGraw-Hill, Montreal, 1978

Brooks,R.A., Sank,V.J., Friauf,W.S., Leighton,S.T., Cascio,H.E., and Di Chiro,G., 'Design Considerations for Positron Emission Tomography,' IEEE Trans. on Biomed. Eng., BME-28:No.2, pp158-176, Feb. 1981

Budinger,T.F., Derenzo,S.E., and Huesman,R.H., 'Instrumentation for Positron Emission Tomography,' Annals of Neurology, 15:No.4, ppS35-S43, April 1984

Burnham,C.A., Bradshaw,J., Kaufman,D., Chesler,D., and Brownell,G.L., 'A Stationary Positron Emission Ring Tomograph Using BGO Detector and Analog Readout,' IEEE Trans Nucl Sci, NS-31:No.1, pp632-636, 1984

Charpak,G., 'Retardation Effects Due to the Localized Application of Electric Fields on the Photocathode of a Photomultiplier', Nucl. Instr. and Meth. 51, p125-128, 1967

Cho,Z.H., Chan,J.K., Eriksson,L., Singh,M., Graham,S., MacDonald,N.S., and Yano, Y., 'Positron Ranges Obtained from Biomedically Important Positron-emitting Radionuclides,' J. Nucl. Med., 16, pp1174-1176, 1975

Cho,Z.H.,Lee,H.S., and Hong,K.S., 'Wedge-Shaped BGO Scintillation Crystal for Positron Emission Tomograghy', J. Nucl. Med., 25:No.8, pp901-904, August 1984

Colombino,P., Fiscella,B., and Trossi,L., 'Study of Positronium in Water and Ice from 22 to -144°C by Annihilation Quantum Measurements', Nuovo Cimento, 38, pp707-723, 1965

Correia,J.A., Burnham,C.A., Chesler,D.A., Elmaleh,D.R., Alpert,N.M., and Brownell,G.L., 'Positron Cameras in Nuclear Medicine,' Proc. 5th Int. Conference on Positron Annihilation, R.R.Hasiguti and K.Fujiwara, ed., Japan Institute of Metals, Sendai, pp391-401, 1979

De Benedetti,S., Cowen,C.E., and Konneker,W.R., 'On the Angular Distribution of Two Photon Annihilation Radiation', Phys. Rev. 177, pp205-212, 1950

Derenzo,S.E., 'Precision Measurement of Annihilation Point Spread Distributions for Medically Important Positron Emitters,' Proc. 5th Int. Conference on Positron Annihilation, R.R.Hasiguti and K.Fujiwara, ed., Japan Institute of Metals, Sendai, pp819-823, 1979

Derenzo,S.E., 'Method for Optimizing Side Shielding in Positron Emission Tomographs and for Comparing Detector Materials', J. Nucl. Med., 21, pp971-977, 1980

Derenzo,S.E., 'Monte Carlo Calculations of the Detection Effiency of Arrays of NaI(Tl), BGO, Csf, Ge and Plastic Detectors for 511keV Photons' IEEE Trans. Nucl. Sci. NS-28:No. 1, pp131-136, 1981

Derenzo,S.E., 'Comparison of Detector Materials for Time of Flight Positron Tomography', IEEE Workshop on Time of Flight Tomography, St. Louis, pp63-68, May 1982

Derenzo, S.E., Budinger, T.F., and Vuletich,T., 'High Resolution Positron Emission Tomography Using Small Bismuth Germanate Crystals and Individual Photosensors,' IEEE Trans Nucl Sci, NS-30: No.1, pp620-670, 1983

Derenzo,S.E., 'Initial Characterization of a BGO-Photodiode Detector for High Resolution Positron Emission Tomography,' IEEE Trans Nucl Sci, NS-31:No.1, pp620-626, 1984

Deutsch,M. 'Annihilation of Positrons', Progress in Nuclear Physics, 3, pp131-158, 1953

Entine,G., Reiff,G., Squillante,M., Serreze,H.B., Lis,S., and Huth,G., 'Scintillation Detectors Using Large Area Silicon Avalanche Photodiodes,' IEEE Trans Nucl Sci, NS-30:No.1, pp431-435, 1983

Eriksson,L., Bohm,Chr., Kesselberg,M., Litton,J.-E., Bergström,M., and Blomquist,G., 'A High Resolution Positron Camera,' Proceedings of the VII Nobel Conference:"The Metabolism of the Human Brain Studied with Positron Emission Tomography", Karolinska Institute, Stockholm, May 17-20, 1983

Evans,A.E., 'Gamma Ray Response of a 38mm Bismuth Germanate Scintillator', IEEE Trans. Nucl. Sci., NS-27:No. 1, pp172-175, Feb., 1980

Evans,R.,D., The Atomic Nucleus, McGraw-Hill, Toronto, pp698-700, 1955

Fan,C.Y., 'Detection of Scintillation Photons with Photodiodes', Review of Sci. Instr., 35:No. 2, pp158-163, 1964

Faruki,M.R., 'Recent Development in Scintillation Detectors for X-Ray CT and Positron CT Applications', IEEE Trans. Nucl. Sci., NS-29:No. 3, pp1237-1249, 1982(a)

Faruki,M.R., '$Bi_4Ge_3O_{12}$(BGO)-A Scintillator Replacement for NaI(Tl)', Proc. of International Workshop on Bismuth Germanate, Princeton University, pp21-38, 1982(b)

Gu,Y.F., 'The Present Status of the Research and Development of Bismuth Germanate in China', Proc. of International Workshop on Bismuth Germanate, Princeton University, pp96-102, 1982

Hoffman,E.J., and Phelps,M.E., 'An Analysis of Some of the Physical Aspects of Positron Transaxial Tomography,' Comput. Biol. Med., 6, pp345-360, 1976

IEEE Trans. on Nucl. Sc., NS-21:No.3, Special Issue on Computed Tomography Reconstruction Methods, June 1974

Ishibushi,H., Akiyama, S., and Ishii,M., 'Influence of Surface Roughness and Crystal Shape on Scintillation Performance of Bismuth Germanates', Proc. of International Workshop on Bismuth Germanate. Princeton University, pp114-134, 1982

Jeavons,A.P., 'The CERN Proportional Chamber Positron Camera',Proc. 5th Int. Conference on Positron Annihilation, R.R.Hasiguti and K.Fujiwara, ed., Japan Institute of Metals, Sendai, p355, 1979

Keller,K.A., Lange,J., Munzel,H., and Pfennig,G., 'Excitation Functions of Charged-Particle Induced Nuclear Reactions', Group 1: Nuclear and Particle Physics, Vol.5: Q-Values and Excitation Functions of Nuclear Reactions, Schopper,H., ed., Landolt-Bornstein: Numerical Data and Function Relationships in Science and Technology, Hellwege,K.H., ed. in chief. Springer-Verlag, New York, 1973

Keller,N.A., and Lupton,L.R., 'PET Detector Ring Aperture Function Calculations Using Monte Carlo Techniques', IEEE Trans. Nucl. Sci., NS-30:No.1, pp676-680, Feb 1983

Knoll,G.F., Radiation Detection and Measurement, John Wiley and Sons, Toronto, 1979

Lecompte,R., Schmitt,D., and Lamoureux,G. 'Geometry Study of a High Resolution PET Detector System Using Small Detectors', IEEE Trans. Nucl. Sc. NS-31:No. 1, pp556-561, Feb. 1984

Lederer,C.M. and Shirley,V.S. ed., Table of Isotopes, John Wiley and Sons, Toronto, 1978

Lorentz,E., 'Photodiode Readout and Related Problems', Proc. of International Workshop on Bismuth Germanate Princeton University, pp229-255, 1982

Lupton,L.R. and Keller,N.A., 'Monte and Anal1: A General Purpose Monte Carlo Simulation for the Design of Single-Slice Positron Emission Tomography Cameras', Chalk River Nuclear Laboratories Report: AECL-7680, Sept., 1982

Lupton,L.R., and Keller,N.A., 'Performance Study of Single-Slice Positron Emission Tomography Scanners by Monte Carlo Techniques', IEEE Trans. on Medical Imaging, MI-2:No.4, pp154-168, 1983

Lupton,L.R., Keller,N.A., Thompson,C.J., and Anderson,L. 'On the Use of Shaped Crystals in Positron Emission Tomography,' In Press.

Macovski,A., and Herman,G.T., 'Principles of Reconstruction Algorithms,' Chap. 110, Vol. 5, Radiology of the Skull and Brain, T.H.Newton and D.G.Potts, ed., The C.V.Mosby Co., Toronto, pp3877-3903, 1981

McKee,B.T.A., 'Current PET Detector Research at Queen's University, Kingston,' Presentation at the Canadian Workshop on Detectors for Positron Emission Tomography, Montreal Neurological Institute, Montreal, April 16,17 1984

Muehllehner,G., Colsher,J.G., and Lewitt,R.M., 'A Hexagonal Bar Positron Camera: Problems and Solutions,' IEEE Trans. Nucl. Sci. NS-30, p652-660, 1983

Murayama,H., Nohara,N., Tanaka,E., and Hayashi,T., 'A Quad BGO Detector and Its Timing and Position Discrimination for Positron Computed Tomography,' Nucl. Instr. and Meth. 192, pp501-511, 1982

Murayama,H., Tanaka,E., Nohara,N., Tomitani,T., and Yamamoto,M., 'Twin BGO Detectors for High Resolution Positron Tomography,' Nucl. Instr. and Meth. 221, pp633-640, 1984

Nahmias, C., Kengon, D., and Garnet, E.S., 'Optimization of Crystal Size in Emission Computerized Tomography'. IEEE Trans. Nucl. Sci. NS- 27, No. 1, pp529-532, Feb. 1980

Nahmias,C., 'Ideal Crystal Sizes for Use in Positron Emission Tomography', Proc. of International Workshop on Bismuth Germanate. Princeton University, pp476-486, 1982

Nestor,O.H., and Huang,C.Y., 'Bismuth Germanate; A High Z Gamma-Ray and Charge Particle Detector', IEEE Trans. Nucl. Sci.,NS-22:No.1, pp68-71, 1975

Okajima,K., Takami,K., Veda,K., and Kawaguchi,F. 'Characteristics of a Gamma Ray Detector Using a Bismuth Germanate Scintillator', Rev. Sci. Instr. 52:No. 8, pp1285-1286, 1982

Petrillo,G.A., McIntyre,R.J., Lecomte,R., Lamoureux,G., and Schmitt,D., 'Scintillation Detection with Large-Area Reach-Through Avalanche Photodiodes,' IEEE Trans Nucl Sci, NS-30:No.1, pp417-423, 1984

Piltingsrud,H.V., 'The Low Temperature Scintillation Properties of Bismuth Germanate and Its Application to High-Energy Gamma Radiation Imaging Devices', J. NUcl. Med. 20, p1279,1979

Rockmore,A.J., and Macovski,A., 'A Maximum Likelihood Approach to Emission Image Reconstruction from Projections,' IEEE Trans. Nucl. Sci., NS-23, pp1428-1432, 1976

Rogers,J.G., 'Current PET Detector Research at the University of British Columbia, Vancouver,' Presentation at the Canadian Workshop on Detectors for Positron Emission Tomography, Montreal Neurological Institute, Montreal, April 16,17 1984

Siegbahn,K., Alpha, Beta, and Gamma Spectoscropy, North Holland, Amsterdam, pp21-23, 1965

Strother,S., 'Is Higher Spatial Resolution in PET Really Necessary?',Presented at the Canadian Workshop on PET Detectors. MNI, Montreal, 1984

Tanaka,E., Nohara,N., Tomitani,T., and Endo,M., 'Analytical Study of the Performance of a Multilayer Positron Computed Tomography Scanner', J. Comput. Assist. Tomogr.,6, pp350-364, 1982

Ter-Pogossian,M.M., Mullani,N.A., Ficke,D.C., Markham,J., and Snyder,D.L., 'Photon Time-of-Flight-Assisted Positron Emission Tomography,' J. Comp. Ass. Tomography, 5, No.2, pp227-239, April, 1981(a)

Ter-Pogossian,M.M., 'Physical Aspects of Emission Computed Tomography,' Chap. 131, Vol. 5, Radiology of the Skull and Brain, T.H.Newton and D.G.Potts, ed., The C.V.Mosby Co., Toronto, pp4372-4388, 1981(b)

Thompson,C.J., Yamamoto,Y.L., and Meyer,E., 'Positome II: A High Efficiency Positron Imaging Device for Dynamic Brain Studies,' IEEE Trans Nucl Sci, NS-26:No.1, pp585-589, 1979

Thompson,C.J., 'An Optical Coupling Scheme for High Resolution BGO Detectors', Report to MNI PET Group, Montebello, March, 1983 (unpublished)

Thompson,C.J., 'Future Potential of PET Imaging', Proceedings of the Conference on the Metabolism and Imaging of the Brain, Fonation Pour l'Etude du Systeme Nerveux Central et Peripherique, March 29-31, 1984

Vacher, J., Laboratoire ER LETI CEA CENG, Grenoble, private communication.

Weber,M.J., 'Discovery of the Scintillation Properties of BGO: Underlying Principles', Proc. of International Workshop on Bismuth Germanate, Princeton University, pp3-20, 1982

Weber,M.J., and Monchamp,R.R., 'Luminescence of $Bi_4Ge_3O_{12}$ Spectral and Decay Properties', J. Appl. Phys.,44:No.12, pp5436-5439, 1973

Wong,W.-H., Mullani,N.A., Wardworth,G., Hartz,R.K., and Bristow,D., 'Characteristics of Small Barium Fluoride (BaF_2) Scintillators for High Intrinsic Resolution Time-of-Flight Positron Emission Tomography,' IEEE Trans Nucl Sci, NS-31:No.1, pp381-386, 1984

Yao Xiao Guang and Rogers,J.G., 'A Monte Carlo Calculation of the Intrinsic Spatial Resolution of a NaI Bar Detector', In Press

Yamamoto,M., Ficke,D.C., and Ter-Pogossian,M.M., 'Experimental Assessment of the Gain Achieved by the Utilization of Time-of-Flight Information in a Positron Emission Tomograph (Super PETT1),' IEEE Trans. Medical Imaging, MI-1:No.3, pp187-192, Nov. 1982

Yamamoto,Y.L., Thompson,C.J., Diksic,M., Meyer,E., and Feindel,W.H., 'Positron Emission Tomography', J. Nucl. Chem. and Phys. In Press

Yamashita,Y., Ito,M., and Hayashi,T. 'New Dual Rectangular Photomultiplier Tube for Positron CT,' Proc. of International Workshop on Physics and Engineering in Medical Imaging, March 1982

Yamashita,Y., Uchida,H., Yamashita,T., and Hayashi,T., 'Recent Developments in Detectors for High Spatial Resolution Positron CT,' IEEE Trans Nucl Sci, NS-31:No.1, pp424-428, 1984